UNIVERSITÀ DEGLI STUDI DI ROMA
"TOR VERGATA"

FACOLTÀ DI SCIENZE MATEMATICHE, FISICHE E NATURALI

DOTTORATO DI RICERCA IN ASTRONOMIA
XX CICLO

HIGH ENERGY BEHAVIOUR OF NEUTRON STAR LOW MASS X-RAY BINARY SYSTEMS

Antonella Tarana

Tutors: Chiar.mo Dott. Pietro Ubertini
Chiar.ma Dott.ssa Angela Bazzano
Coordinatore: Chiar.mo Prof. Roberto Buonanno

Contents

List of Figures

List of Tables

Introduction

Low Mass X-ray Binaries (LMXBs) are close binary systems composed by a compact object and a donor late-type ($>$ A type) low mass star ($<$2 $M_{\odot}$). The compact object accretes mass via Roche lobe overflow with consequent formation of a geometrically thin and optically thick disk. These systems emit in the X-ray band with luminosity up to 10^{38} erg s^{-1}. They are old populationand located in the Galactic Bulge of the Milky Way, and mostly in Globular Clusters.

We aimed to study the high energy emission from a subclasses of this system: Atoll, Bursting sources. The Atoll source, so called depending on the track in the Hardness-Intensity Diagrams, are characterised by different spectral state and moves from the ”Hard” to the ”Soft” spectral states on time scale of hours or days. Most of the Atoll sources are also showing bursting behaviour, i.e. type-1 X-ray bursts, which are thermonuclear flashes onto the surface of compact object that is a Neutron Star (NS). So, the presence of bursts proves that the binary system has a NS as compact object.

The main emission processes of NS LMXBs are explained as due to a black body thermal emission arising from the accretion disk (or neutron star or boundary layer) that dominates in the soft energy band (0.1-10 keV) and a Comptonization component that dominates at high energies ($>$20 keV) due to repeated inverse Compton scattering of the seed photons by hot electrons plasma.

Neverthless, the complexity of the high energies features of the spectra makes them difficult to understand. Moreover, in the past few years the study of these systems revealed that they are high energy emitters with spectral state transition similarly to Black Hole (BH) systems. Lack of high energy cut-off indicating the possible correla-

tion to radio emission and jets production as well as a reflection component has been recently reported in few cases.

In spite of these evidences, still open questions remains (such us disk-jet coupling), and a deep survey of their wide band behaviour was missed before *INTEGRAL* launch.

I report here on the results of the study of the high energy emission from a selected sample of NS LMXBs, Atoll and bursters, in the Galactic Bulge: 4U 1608–522, GX 354–0, 4U 1722–30, 4U 1820–30, 4U 1812–12, XB 1832–330 and also 4U 1254–690. This sample is composed by sources with different characteristics, most of them are located in Globular Clusters, some are classified as transient and some as persistent sources.

The PhD work consisted on the investigation of this sample, performing the scientific analysis of the *INTEGRAL* data. This observatory, thanks to the large field of view and high spectral resolution of the on board instruments, is ideal to study the high energy emission (in particular above 60 keV) and to search for spectral variations and transitions. The work is firstly based in the monitoring of their X and γ -ray behaviour through creation of the light curves in different energy bands to search for temporal variability. Then hardness-intensity diagrams were constructed, and finally a detailed spectral extraction was performed to determine the physical parameters dominating the spectral features. In same cases we use also scientific data from other satellites, such as *BeppoSAX* and *RossiXTE*.

Scientific results can be summarized as follows:

Confirmation that the NS LMXBs systems are objects with a high energy emission extending up to 200-300 keV as the BH systems.

The sources 4U 1812–12, XB 1832–330, 4U 1254–690 showed a persistent behaviour with Comptonized high energy emission up to 200 keV.

The sources 4U 1820–30, 4U 1608–522, 4U 1722–30 and GX 354–0 showed spectral changes. In particular for 4U 1820-30 for the first time was detected an high energy emission characterized by the presence of a hard tail extended above 50 keV during the Hard spectral state. This hard tail could be due to syncrotron emission correlated with radio emission of a jet, or more probably, by a thermal/non-thermal Comptonization emission. A similar hard tail emission was also detected from the Hard state of GX

354–0.

Finally, we re-constructed, for all the source-spectral states detected, the ”Bursters Box”, i.e a diagram that compares the source luminosity in the energy band 4-10 keV with the 20-200 keV one. This is devoted to discern the similarities and differences with BHs and also to compare amongst themselves the sources sample.

The thesis structure is as follows:

- In Chapters 1 and 2 I summarize the X and hard X characteristics and physical properties of NS binary systems, outlining importance and aim of the thesis in the framework of the high energy study of NS LMXBs.
- In Chapter 3 and 4 I deal with the *INTEGRAL* mission overview and data analysis method.
- In Chapter 5 I report on the results of the analised sample of NS LMXBs and on the specific source discussion.
- Finally, an overview of the discussed results and conclusions are given in Chapter 6.

Chapter 1

The Accretion physics of the X-ray binaries

1.1 The X-ray binaries

The major part of the stars of the universe belong to binary systems. The binary systems consist of two stars gravitationally bound and rotating around the common centre of mass.

The evolutions of binary system are different from the evolution of the single stars [1]. During the evolutions transfer matter phenomena and accretion could happens. The accretion happens when one of the two stars reaches its Roche Lobe, the greater critical equipotential surface conatining the two stars separately, and that intersects into the unsteady Lagragian point, L_1. The matter outflows, through the L_1 point, to the other star that begins to accrete. The binary systems are defined closed, in opposite to the open systems, if during the evolution at least one the stars reach its critical Roche Lobe [2]. On the other hand, mass transfer could happens also without Roche Lobe overflow. This is the case of the systems that has a massive donor stars (>2 $M_\odot$) that expel significant amount of matter through stellar wind.

Of particular interest are the systems in which the accreting star is a compact object such as a black hole (BH), neutron star (NS) or a white dwarf (WD) (see for a reference [3]), because these systems become a X-ray emission sources, called X-ray Binaries.

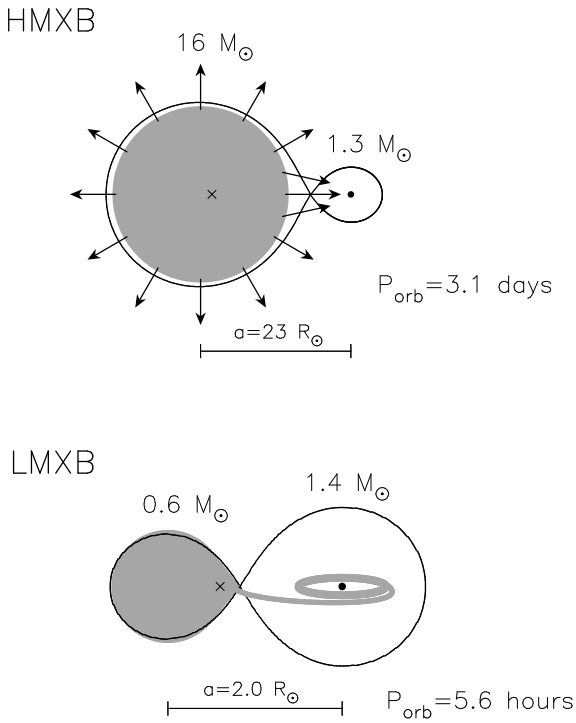

Figure 1.1: Examples of a typical HMXB (top) and LMXB (bottom). The compact object (in this case a neutron star) in the HMXB is fed by a strong high-velocity stellar wind. The compact object in an LMXB is surrounded by an accretion disk which is fed by Roche lobe overflow [1].

The X-ray Binaries emit the major part of their flux in the X-ray band (and not in the optical band) with typical luminosity of 10^{37} erg s^{-1} and temperature of 10^8 K. They are very well studied in the X-ray band through the instruments on board satellites because of the atmosphere absorption of the X-rays.

The X-ray Binaries are classified as **High Mass X-ray Binaries** (HMXBs) or **Low Mass X-ray Binaries** (LMXBs) according to the mass of the donor star.

The High Mass X-ray Binaries are young systems ($< 10^7$ y) in which the companion star is a early-type, massive star (O, B type) with a strong stellar wind that provide to the accretion of the compact object (***wind accretion***).The Low Mass system have a late–type (>A type) donor star with a mass $<2M_\odot$. In this case the accretion is due to the ***Roche lobe overflow*** of the material through the inner lagragian point [4].

Figure 1.1 shows a simple accretion scheme of HMXB and LMXB respectively.

1.2 The basic accretion physics

With accretion we refer to the phenomenon of the deposit of matter into a star due to the gravitational force. If M is the mass of the compact object, R is the distance of the region of energy release from the center of the compact object, and m is the accreting mass that falls down to the compact object, than the gravitational potential energy released due to the accretion, assumed steady state and spherical, is:

$$\Delta E_{acc} = \frac{GMm}{R}$$

where G is the gravitational constant. The produced luminosity is

$$L_{acc} = \frac{GM\dot{m}}{R} \tag{1.1}$$

where $\dot{m}$ is the ***mass accretion rate*** defined as the quantity of accreted material in the unit of time.

The typical mass accretion rate and Luminosity revealed from a X-ray binary is $\dot{m} \simeq 10^{-8\div-9}$ $M_{\odot} y^{-1}$ and L$\simeq 10^{37\div38}$ erg s^{-1} [5].

1.2.1 The accretion efficiency

The energy and luminosity can written as:

$$\Delta E_{acc} = \eta mc^2$$

and

$$\Delta L_{acc} = \eta \dot{m} c^2$$

where we have introduced the *efficiency*, a parameter defined as

$$\eta = \frac{G}{c^2}\frac{M}{R}$$

The efficiency is an adimensional parameter with value rengies between 0 and 1. This parameter is independent from the accretion rate and depend only on the mass and the

radius of the accreting star. The more the accreting object is compact the more the accretion process is efficient. As a consequence, we have
- for a WD ($R = 10^9$ cm), $\eta \simeq 0.02\%$,
- for a NS ($R = 10^6$ cm), $\eta \simeq 15\%$,
- for a BH ($3R_{Schw}$-$1.3R_{Schw}$[1]), $\eta \simeq 5.7 - 43\%$.

We note that the energies release of the binaries are dominated by the accretion and not by the nuclear fusion reactions, which has the efficiency $\eta_{nuc} \simeq 0.7\%$ (for the conversion of hydrogen to helium) [5]. An accreting NS (object of interest in this thesis) with radius $R = 10^6$ cm, and $1M_{\odot}$ releases an accretion energy E_{acc} of about 10^{20} erg for accreted gram, while the E_{nuc} is of about 10^{18} erg for gram.

1.2.2 The Eddington luminosity

As can be derived from Eq. 1.1, the accretion luminosity increases with the increasing of the mass accretion rate, $\dot{m}$. Exists a limit at the value of the accretion luminosity. This limit is expressed by the *Eddington luminosity* that is the luminosity when the gravitational force of the mass of the accreting particles, is balanced by the radiation pressure of the compact star (that interact by Thomson effect with the charge particles that fall into the accreting star). The Eddington luminosity is the maximum luminosity that it could be reach during the accretion processes.

Considering the case of an accreting gas composed by completely ionized hydrogen. The radiation pressure of the object that has a luminosity, L, and flux, F, at the distance from its centre, r, is

$$P_{rad} = \frac{F}{c} = \frac{L}{4\pi r^2 c}$$

than the radiation force acting on the electron is

$$F_{rad} = \sigma_e \frac{L}{4\pi r^2 c}$$

[1] R_{Schw} is the Schwarzschild radius ($R_{Schw} = 2GM_{BH}/c^2$ for a BH). The BHs don't have a soild surface, so the last stabil orbit of the matter could be considered as BH radius, which is equal to $3R_{Schw}$ for a non-rotating BH and $1.3R_{Schw}$ for a rotating BH.

where σ_e is the Thomson cross-section of the electron (the proton cross setion is neglectable respect to the electron cross section [2]). The gravitational force of the central mass, M, that is neglectable for the electron (because of the minor mass respect to the proton), is:

$$F_{grav} = \frac{GMm_p}{r^2}.$$

By equaling the two opposite forces, F_{rad} and F_{grav} we have the Eddington luminosity:

$$L_{Edd} = \frac{4\pi Gcm_pM}{\sigma_e}$$

$$= 1.38 \cdot 10^{38} \left(\frac{M}{M_\odot} \right) \quad \text{erg s}^{-1}.$$

The Eddington luminosity corresponds to the maximum luminosity that a source of mass M, with spherical symmetry, can emit during the accretion process of completely ionized gas [7].

1.2.3 The radiation temperature of accreting matter

The radiation temperature depends on the conditions of thermalizing the infalling matter kinetic energy. The lowest temperature of radiation is obtained in an optically thick case, when all released energy is emitted as spherically symmetric black body radiation from a sphere of radius R. This temperature is equal to:

$$T_{min} = \left(\frac{L_{accr}}{4\pi R^2 \sigma} \right)^{1/4}$$

where σ is the Stefan-Boltzmann constant ($\sigma = 5.67 \times 10^{-5}$ erg s^{-1} cm^2 K^{-4}). The highest temperature is obtained in an optically thin case, when kinetic energy of an accreted proton-electron pair is thermalized and directly radiated away. In this case we

[2] the Thomson cross section of the electron is $\sigma_e = \frac{8\pi e^4}{3m_e^2c^4}$, since $m_p >> m_e$ ($m_e = 10^{-27}$ g and $m_p = 10^{-24}$ g) then we could disregard the proton cross section.

have:

$$T_{max} \sim \frac{GMm_p}{3kR}$$

where m_p is the mass of proton.

Assuming a surface of a typical neutron star and that L_{acc} is at Eddington limit, we estimate a $T_{min} \sim 10^7$ K, which corresponds to energy $E = h\nu = kT \sim 1$ keV (where k is the Boltzmann constant, $k = 1.38 \times 10^{-23}$ J K^{-1}) and $T_{max} \sim 5 \times 10^{11}$ K, which correspond to $E \sim$50 MeV. This range corresponds to X-rays and soft Gamma-rays [5].

1.2.4 The accretion disk

In the Low Mass X-ray Binaries the accretion phenomenon occurs through the Roche Lobe overflows. Matter passes through the critical point L_1 following a trajectory that depends on its angular momentum. In the case of matter has no angular momentum, it fall down directly into the compact star without a particular trajectory, on the comtrary, in the case of the matter having an angular momentum, it must orbits around the compact object, thereby forming an *accretion disk*. The angular momentum per unit of mass of the inflow gas is:

$$\vec{l} = \vec{r} \times \vec{v} \quad \text{con} \vec{v} = \vec{v}_{par} + \vec{v}_{perp}$$

dove v_{par} is the parallel component of the velocity of the gas and v_{perp} is the perpendicular component. The parallel component of the velocity is lower than the sound value, $\vec{v}_{par} \simeq 10$ km s^{-1}, therefore the angular momentum in this direction is small. The perpendicular component is $\vec{v}_{perp} \geq \frac{2\pi}{P}a$, it depends on the major orbital semiass, a, and on the orbital period, P. The closed binary systems have periods (and so major semiasses) such that determine an high perpendicular velocity and an high angular momentum, that causes the orbit of the mass around the comact object. This happens for the LMXBs that shows periods of the order of hours or days and perpendicular velocity greater than 100 km s^{-1}.

The particles around the compact object interact themselves, so that energy dissi-

pation modifies the orbits of the gas since a circulars orbits that have least energy. The distance of the inner stable orbit, defined as circularization radius, r_{circ}, is the orbit for which the gas angular momentum, l, is equal to the angular momentum of Keplerian orbit of the gas, l_K, that is

$$l_K = \left(\frac{GM}{r_{circ}}\right)^{1/2} r_{circ} \quad ,$$

hence,

$$r_{circ} = \frac{l^2}{GM} \quad .$$

So, if $r_{circ} < R_{star}$ then the matter fall down directly into the compact star; if $r_{circ} > R_{star}$ then the matter flow down in circular orbits around the compact star, with the forming the *accretion disk*.

The disk Luminosity is very high, in fact, according the Virial theorem, half of the gravitational potential energy must be released as warmth and half must be irradiated. So, the disk luminosity results as half of the accretion luminosity:

$$L_{disc} = \frac{1}{2}\frac{GM\dot{m}}{R} = \frac{1}{2}L_{acc} \quad . \tag{1.2}$$

This results is also obtained by the *standard disc* theory for which the disk is approximated to a *thin disc* where the matter accretes through a sequence of Keplerian orbits with gradually decreasing angular momentum. The angular momentum is carried outwards and energy is dissipated by the viscosity (*shear viscosity*) providing a torque between the shearing orbits.

In the next Chapter will deal with the emitted energy spectrum of the thin disc.

Boundary layer

The required Kepler angular velocity, $v_K(r) = (GM/r^3)^{1/2}$, cannot be maintained at the inner edge of the disk if it is to join smoothly to a non-magnetic acreting star spinning at below the break up velocity $v_K(r)$. The region in which gas moving at Keplerian velocities in the disk is decelerated to match the star angular velocity v_x is called the **boundary layer** (BL). In such region if $v_x \ll v_K(r)$ there exists a point where $dv/dr = 0$ implying that the shear vanishes at this point. Thus shear viscosity

is no longer able to transport angular momentum into or out the star, and the accreting object simply gains the angular momentum of the accreting matter.

If the star spins more slowly than the break-up value, the BL must release a large amount of energy as the accreting matter comes to rest at the stellar surface. Part of this energy is used to spin up the star, but still there remains an amount of luminosity emitted in the BL

$$L_{BL} = \frac{GM\dot{m}}{2R}\left(1 - \frac{v_x}{v_K}\right)^2 \quad .$$

For $v_x \ll v_K$ this correspons to one-half of the total accretion luminosity. Not all the L_{BL} goes as radiation, but it is clear that for accretion onto a slowly rotating star, the boundary layer can emit a luminosity comparable to that of the disc. For a rapidly rotating star $\dot{v}$ is always negative and viscosity transports angular momentum outwards at all radii and accordingly L_{BL} reduces drastically [5] [6].

1.2.5 Wind accretion

This type of accretion happens in double systems with a high dimension companion star of O, B spectral type, that has a strong stellar wind that accretes the compact object. So, this type of accretion takes place in the High Mass X-ray Binaries. The lower limit of the wind velocity is given by the escape velocity on the surface of the star that emits it, and for a mass of 10 $M_\odot$ and radius of $5R_\odot$ the velocity reach the value of 1000 km s^{-1}.

The accretion rate is about $10^{-4\div-5}$ $M_\odot$ y^{-1} i. e. higher than the accretion by the Roche lobe overflow, but in this case not all the accretion matter is really accreted by the compact object. This is because of the irradiated wind from the companion star is radial and isotropic, so part of the matter has a opposite direction to the accreting star; and also because of the matter of the wind could have a kinetic energy too high to escape from the attractive force of the compact object. For this reason even if the accretion rate of the wind accretion processes is higher than the accretion via Roche lobe overflow, the accretion Luminosity results similar for both processes (L$\sim 10^{37}$ erg s^{-1}).

The accretion radius is the radius at which the kinetic energy of the particles of the

accreting matter, is minor or equal to the gravitational potential energy of the compact star:

$$r_{acc} = \frac{2GM}{v_{rel}^2}$$

where the v_{rel} is the wind velocity relative to the compact star, defined as $v_{rel} = v_w + v_{orb}$, being v_w the wind velocity and v_{orb} the orbital velocity of the compact star.

Because of the few physical information about the wind velocity and the accreting matter angular momentum the formation of an accretion disk is not sure. In any case if the accretion disk takes places it will have small dimension [5].

1.3 The Low Mass X-ray Binaries

As already reported the main difference between Low Mass and High mass is the way of the transferring matter. In the Low Mass X-ray Binaries happens Roche lobe overflows with the formation of the accretion disc.

The old nature of the companion star in the LMXBs systems ($5 \div 15 \times 10^9$ yrs) involves that the distribution in the Galaxy is not casual. In fact they are concentered towards the Galactic Center like the old disk population (II population) and many of them are found in Globular Cluster, the cluster composed by same-old-age stars. The High mass systems are otherwise concentered in the Galactic plan and in the spiral arms. The recent spatial distribution of HMXBs and LMXBs in our Galaxy as is shown in Figure 1.2 by the third *INTEGRAL* Galactic Survey.

Because of the low mass and late type of the companion star, they have lower luminosity in the optical band respect to the high mass systems. In fact the ratio L_X/L_o is about 100-1000 for the LMXBs and L_X/L_o is ≤ 1 for the HMXBs. Moreover the probability to detect the eclipse is lower than the high mass systems. In fact the probability to detect an eclipse varies as the cube root of the mass of the companion star. Because of the detection in the optical wavebands is argue, than in most cases the evaluation of the masses, through the *mass function* estimation, is not possible.

The low mass orbital period are not higher and ranges from 0.2 to 400 hours, so often the LMXBs are very compact systems.

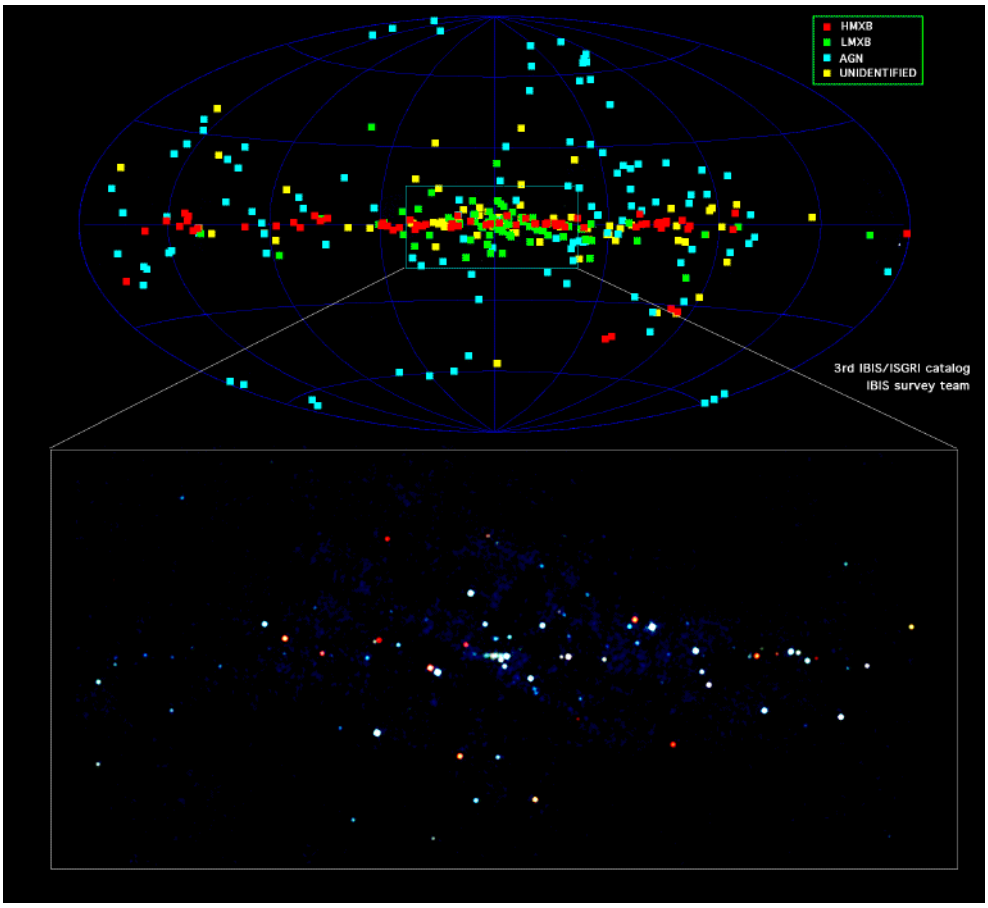

Figure 1.2: Third *INTEGRAL* Galactic Survey distribution of Low-Mass X-ray Binaries, High Mass X-ray Binaries, and extragalactic and unidentified sources. Note the different position of the Low Mass and High Mass Binary (Credit to IBIS Survey Team).

.

The LMXBs have also other characteristics: they are classified as Atoll or Z source based on the shape on the X-ray Colour-Colour diagram; and many of them are also burster sources. These characteristics are not exclusive: the Atoll/Z sources could be also burster sources. Because this thesis deal with Burster, Atoll LMXBs, then we report further on their characteristics in the next sections.

1.3.1 Type 1 X-ray bursters

The Bursters are low magnetic (B $\sim$ 10^8-10^{10} G) LMXBs that show, on top of their X-ray persistent emission, X-ray spikes, called *bursts*, with a duration of few seconds (10-100 s) and an energy release of 10^{39} ergs. The recurrance time ranges from few hours to few days. They show a fast rise and exponential decay and are, in general, detectable in the range of energy of 0.1-40 keV, with the current instrumentation. The energy spectra of the burst are a thermal black body and the main characteristic of the type 1 burst is the *cooling* black body during the burst decay. This is evident also from the light curves in different energy bands: the decay times are much shorter at high energies than at low energies [8].

The type I sources differences from the type II sources that shows different bursts. They are no characterised by the cooling black body and are due to accretion instability [9].

Thermonuclear burning on the Neutron star surface

The type 1 X-ray burst are explained by the thermonuclear-flash model that interpers the bursts as the unstable thermonuclear burning on the compact star surface. Due to the accretion flow from the disc, a layer of the hydrogen will be produced on the surface of the neutron star. It will reaches the condition of the thermal nuclear burning, then producing a underlying layer of helium and so on (see Figure 1.3). This model has many observational proves. In fact the cooling of the black body spectra, the rise time and exponential decay and the bursts recurrance time confirm this model. By the black body radius, derived from the spectra, of the order of the typical neutron star radius; and by the validity of the thermonuclear-flash model allow to conclude that type 1 X-ray sources are Neutron star [9].

This is a very important because the presence of a burst in the LMXBs permits to identify the nature of the compact object of the binary systems. The other possibility to identify the nature of the compact object is through the optical method that as already reported it is rare to get [9].

All the LMXBs observed and analysed in this thesis are Bursters, so all have a

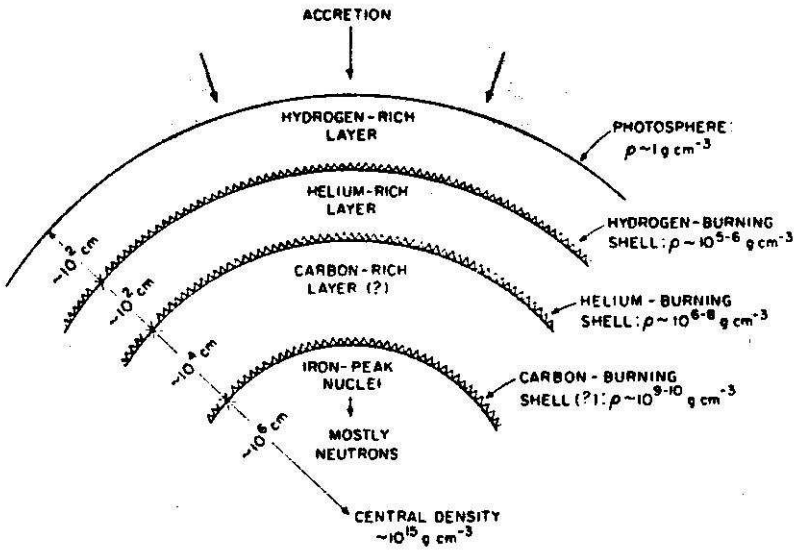

Figure 1.3: Surface layers of accreting, bursting neutron star [9].

Neutron star as compact object.

Double peaked bursts

In bright bursts the local X-ray luminosity in the atmosphere may reach the Eddington limit and the photospheric layers can be shifted off the neutron star surface by radiaton pressure. In these bursts the blackbody temperature decreases while the inferred blackbody radius simultaneously increases and the total X-ray flux stays approximately constant. These bursts are called Photospheric Radius Expansion (PRE) bursts. In this case the burst profile appears as double peaked (the most intense shows a precursor) because the flux is shifted out of the X-ray band by the expansion [10]. As the photosferic radius increases, at near constant L, the effective temperaure will decrease (accordingly to $T_e = (L/4\pi\sigma)^{1/4} \times (R_{ph})^{-1/2}$) and the X-ray emission shift temporarily to low energy. As the photospheric radius starts decrasing, X-ray emission increases, first at low energies and later on, as the temperature continues to increase, at high energies [8].

Since the Eddngton limit imposes an upper limit to burst fluxes, the peak luminosi-

ties of the bursts may provide a ”standard candle”, and so the double peaked bursts could be used as ditance indicators [11].

1.3.2 The Atoll sources

The low magnetic-field neutron star systems are divided in ”Z” and ”Atoll” source depending on the shape of the track showed in the X-ray Colour-Colour Diagram (CCD) or Hardness Intensity Diagram (HID) and the related spectral and timing properties [12].

In Figure 1.4 is showed a typical CCD of Atoll and Z sources, with the different branches that correspond to different spectral and timing properties. Their variability go down to less than a millisecond, and their power spectra show aperiodic phenomena, such us Quasi Periodic Oscillations (QPOs) and low and high ferquency noise, with different frequency depending on the location on the CCD/HIDs (studied by *timing* technique) [13].

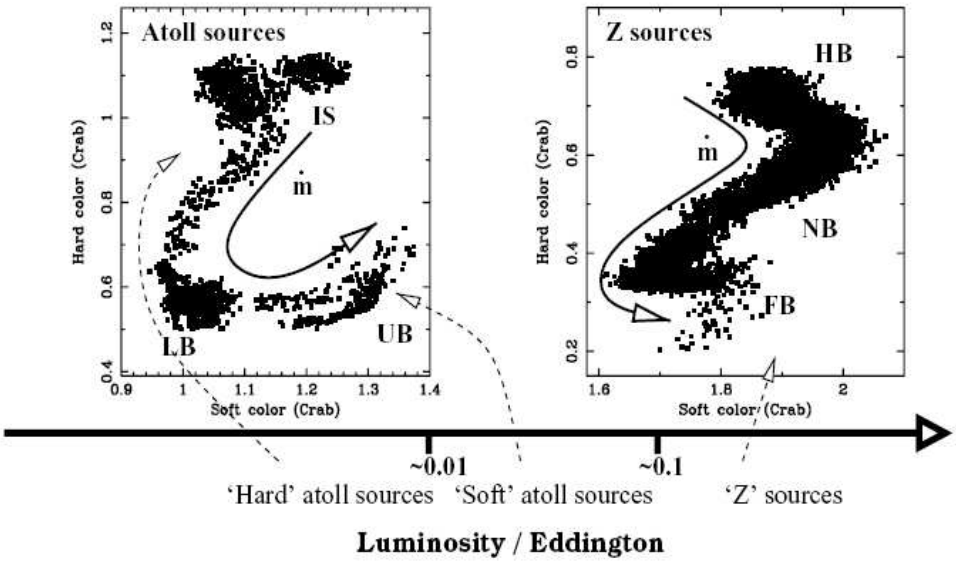

Figure 1.4: Color-Color Diagram of the Atoll and Z sources, with their different branches. Island (IS), Lower and Upper Banana branches (LB, UP) for the Atolls; and Horizontal (HB), Normal (NB), and Flaring (FB) branches for the Z. With the solid arrows are showed as the accretion rate increases [13].

Z sources are the most luminous and accrete at a significant Eddington rate of 0.5-1 L_{Edd}.

Atoll sources, most of them also Bursters, cover a much wider range of luminosity, from about 0.001 L_{Edd} up to the range of the Z sources, but usually are in the 0.01-0.2 L_{Edd} range [13]. They could show a persistent and also transient behaviour, showing intermittent activity intervals called outbursts, usually lasting week to month, separated by long quiescent emission intervals.

The Atoll-shaped track, trace out in the CCD/HIDs, consists of different zones characterized by different variability: the main ones are called Banana Branches (devided in Upper Banana and Lower Banana) and Island Branch. Transient Atoll sources move along the branches as a hysteresis, and sometime in a relatively rapid way ($\sim$ 1 day). The different branches correspond to different spectral states; the Banana state is characterized by a high X luminosity and correspond to the Soft spectral state while the Island branch happens at low X luminosity when the sources are in the Hard spectral state. The main parameter changing during the track and the spectral avolution is the mass accretion rate, $\dot{m}$ [13].

In the next chapter we there will be a description of these states and their spectral components.

Chapter 2

High energy emission from Neutron Star Low Mass X-ray Binaries

2.1 Emission processes

The emission processes which contribute to the X-ray Binary behaviour are showed in Figure 2.1. Depending on the different type of Binary and compact central object, same of these features could be not present.

2.1.1 Disk emission component

The accretion disk component of the X-ray Binary spectra is usually modeled by the so-called *"Standard disk model"* or *"α disk model"*, developed by Shakura & Sunyaev (1973) [15]. This was one of the first developed models and later used as base for the next ones to follow, such us the multicolor disk black body (MCD) Mitsuda 1984 [16], since to the more recent ADAF and CADAF theories [17] [18].

In the Standard model the accreting gas forms a geometrically thin ($H << R$ where H is the thickness and R is the radius of the disc) and optically thick disk ($\tau >> 1$, where τ is optical depth) producing a quasi-blackbody spectrum due to thermal emission. The effective temperature of the accreting gas is in the range $10^5 - 10^7$ K, depending on the compact object mass and the accretion rate. The matter accreting

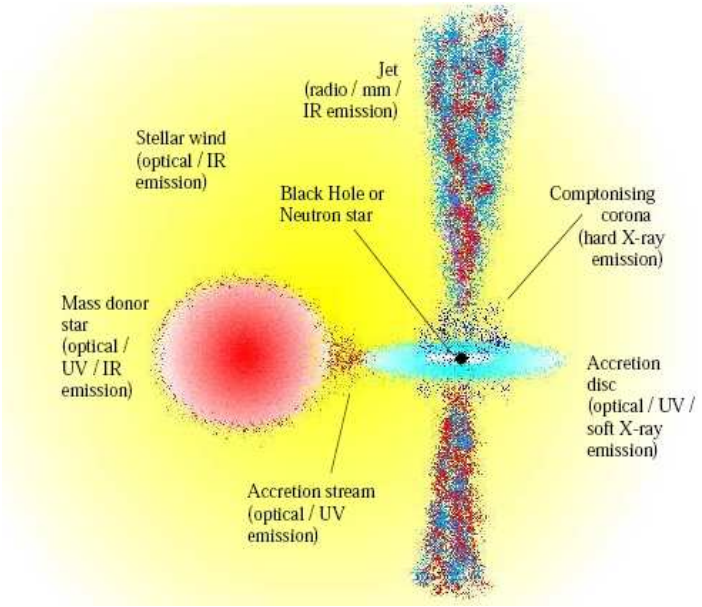

Figure 2.1: Emission processes of XRBs (from [14]).

onto a compact object is likely to have a net angular momentum. Inside the disk will must be a phenomenon which transfers the angular momentum outwards the accretion disc. The accreting gas has a differential rotation, with a Keplerian angular velocity given by $v_K = \left(\frac{GM}{R^3}\right)^{1/2}$. Than the transfer is explained as the internal viscous torques by the *shear viscosity* between the rings of matter, and it is orthogonal to the gas motion. The physical origin of the viscosity is still unclear. By calculating the variation of the net viscous torques we obtain the radiating energy flux of the steady disc, called *dissipation rate*:

$$D(R) = \frac{3GM\dot{m}}{8\pi R^3}\left[1 - \left(\frac{R_{in}}{R}\right)^{\frac{1}{2}}\right]$$

where R_{in} is the radius of the last stable orbit of the disc. The luminosity of the disk is obtained by intergrating the radiating energy flux from the inner radius to the external radius assumed at infinity distance:

$$L_{disc} = \frac{1}{2}\frac{GM\dot{m}}{R_{in}} \quad .$$

As already obtained in Eq. 1.2.

Each element of the disk face radiates roughly as a blackbody with a temperature T(R) as for equation:

$$T(R) = \left\{ \frac{3GM\dot{m}}{8\pi R^3 \sigma} \left[1 - \left(\frac{R_{in}}{R} \right)^{\frac{1}{2}} \right] \right\}^{\frac{1}{4}} \tag{2.1}$$

where R_{in} is the inner cut-off radius of the accretion disc. Hence the accretion disk has a temperature that depend on the radius as $T(R) \propto R^{-3/4}$.

The emitted spectrum results as a multicolor disk black body whit intensity:

$$I_\nu = B_\nu[T(R)] = \frac{2h\nu^3}{c^2} \frac{1}{e^{\frac{h\nu}{kT(R)}} - 1} (erg\ s^{-1}\ Hz^{-1}\ sr^{-1}). \tag{2.2}$$

where $B_\nu(T)$ is the Planck function. For an observer at a distance D whose line of sight makes an angle i to the normal to the disc, the observed flux is:

$$F_\nu = \frac{2\pi \cos i}{D^2} \int_{R_{in}}^{R_{out}} I_\nu r\, dr \tag{2.3}$$

where R_{out} is the outer radius of the disc, since a ring between radii R and R+dR subtend a solid angle $2\pi R\, dR \cos i\, /D^2$. With the blackbody assumption, we get

$$F_\nu = \frac{4\pi h \cos i\, \nu^3}{c^2 D^2} \int_{R_{in}}^{R_{out}} \frac{R\, dR}{e^{\frac{h\nu}{kT(R)}} - 1} \tag{2.4}$$

- For frequencies $\nu \ll kT(R_{out})/h$ the Planck function B_ν approximates to the Rayleigh-Jeans form $2kT\nu^2/c^2$; hence Eq. 2.4 gives $F_\nu \propto \nu^2$.

- For frequencies $\nu \gg kT(R_{out})/h$ the Planck function B_ν assumes the Wien form $2h\nu^3 c^{-2} e^{-h\nu/kT}$: the integral in Eq. 2.4 is dominated by the hottest parts of the disk $(T \sim T_{in})$ and the spectrum has exponential form.

- For intermediate frequencies ν such that $kT(R_{out})/h \ll \nu \ll kT_{in}/h$, Eq. 2.4 becomes approximately $F_\nu \propto \nu^{1/3}$.

Disk emission has tipical peak in the UV – soft X-ray (0.5-1.5 keV) [5]. The standard

disk model can explain the production of soft X-ray photons, but not the hard X-ray ones.

2.1.2 Thermal Comptonization component

Different models have been developed, based on different assumptions, but all aiming to model those observed spectra that are not explained with the standard disk model only. The broad-band X/γ-ray spectra of X-ray Binaries can be explained in terms of successive Compton upscatterings of soft photons - *Comptonization* - in a hot electron cloud. Both neutron stars or galactic black holes and Seyfert galaxies (a specific case of AGN) show a hardening of the spectra at $\sim$ 10 keV, which is attributed to Compton reflection (combined effect of photoelectric absorption and Compton down-scattering) of hard radiation from a cold material [19]. This implies the presence of cold material in close proximity, such as a ***corona***. Hard radiation, reprocessed in the cold matter, can form a significant fraction of the soft seed photons for Comptonization. The energy balance of the cold and hot phases determines their temperatures and the shape of the emerging spectrum [58].

The *Compton scattering* is the collision between a high energy photon and a stationary electron. After the collision the photon has a lower energy because of the transferring of energy to the electron. In the non-relativistic regime ($\hbar\omega \ll m_e c^2$) the energy variation of the photon is rapresented by:

$$E' = \frac{E}{1 + \frac{\hbar\omega}{m_e c^2}(1 - \cos\alpha)}$$

where the E' is the photon energy after the collision, m_e is the electron mass, and α is the *scattering angle*, i.e. the deviation angle of the photon because of the collision. Averaging over the different scattering angles, the average energy lost of the photon is:

$$\frac{\Delta\varepsilon}{\varepsilon} = -\frac{\hbar\omega}{m_e c^2} \quad .$$

The *inverse Compton scattering* is the collision between a low energy photon and ultrarelativistic electron. In this case the photon increase the energy. If the electrons

have a thermal distribution of of velocities T_e ($3/2kT_e = 1/2m_e v^2$), then the fraction of energy gain by the photon is given by:

$$\frac{\Delta\varepsilon}{\varepsilon} = \frac{4kT_e}{m_e c^2} \quad .$$

As a result, the equation which describes the energy changes of the photons in a Compton collisions is:

$$\frac{\Delta\varepsilon}{\varepsilon} = \frac{-\bar{h}\omega + 4kT_e}{m_e c^2}$$

- if $4kT_e >$ then the photons gain energy,
- if $4kT_e <$ then the photons loose energy.

In the case of electrons with higher temperature (then higher energy) respect to the photons, then the repeated inverse Compton scattering (Comptonization) could modify the initial spectrum of the photons (*seed photons*). This condition is verified when

$$4y \geq 1$$

where y is the *Comptonization parameter* given by

$$y = \frac{kT_e}{m_e c^2} max(\tau_e, \tau_e^2)$$

where $\tau_e = N_e \sigma_T l$ is the Thomson scattering optical depth of the region with electron density N_e and dimension l.

The ideal condition for the Comptonization processes are created in the region near the compact object. The Comptonization process dominates the energy spectrum of the binaries when are in the so called "Hard spectral state". The observation of a *cut-off* in the spectrum indicate that this is a thermal process. While the lack of a cut-off indicate a non thermal nature or a hybrid, thermal-non thermal nature of the Comptonization (i.e. of the electrons distributions of velocities) [20].

2.1.3 Non-thermal component

The non thermal emission in the X-ray Binaries is observationally evident by the presence of a power law tail or by the lack of high energy cut off. The non thermal emission could be due either to the syncrotron emission or to hybrid, thermal and non-thermal, population of the electrons plasma of the corona. In the last case, the most likely mechanism to power the non thermal electron is the magnetic reconnection in the corona above the disk [21]. The syncrotron emission could be associated to the production of the *jet*.

Jets are formed in a region extending near the compact object and the inner edge of the accretion disk and extending out, probably, along symmetry axis. They are a narrow stream of energy and particles flowing out of the system with relativistic velocities. At the moment a comprehensive theory that can account for the process of jet formation, acceleration and collimation doesn't exist, though observation strongly suggest powerful jets are produce for sub-classes of object and not for others. Jets are mainly observed from their radio emission. High brightness temperatures, non-thermal spectra and polarization measurements indicate an origin due to synchrotron emission from relativistic electrons [14].

Synchrotron radiation

Charged particles, relativistically moving in the presence of magnetic fields B, loose energy emitting non-thermal synchrotron radiation with frequency spectrum peaked around

$$\nu \approx \frac{4}{3}\gamma^2\nu_L$$

where ν_L is the Larmor frequency ($= eB/2\pi mc$). The power emitted by the particle, being α the angle between the velocity $\vec{v}$ and the magnetic field $\vec{B}$, is

$$P_s = 2\sigma_T c U_B \gamma^2 \beta^2 \sin\alpha^2$$

where σ_T is the Thomson cross section and $U_B = B^2/8\pi$ the magnetic energy density. For electrons isotropically distributed, the average over the pitch angles leads to the

expression for the electron average cooling rate:

$$\dot{E}_{syn} = \frac{4}{3}\sigma_T c U_B \gamma^2 \beta^2 \tag{2.5}$$

Beaming effects concentrate the emitted radiation field along the forward direction, leading to a distribution lying within a cone of half-angle $1/\gamma$, where $\gamma = (1 - v^2/c^2)^{-1/2}$ for a velocity v.

For a population of electrons, assuming a power-law energy distribution $N(\gamma) = N_0\gamma^{-n}$ between γ_1 and γ_2, the total emissivity is obtained integrating Eq. 2.5 over $N(\gamma)$, yielding

$$j_{syn}(\nu) = B^{1+\alpha}\, N_0\, \nu^{-\alpha} \tag{2.6}$$

where $\alpha = (n-1)/2$. A power-law energy distribution of the emitting particles yields a corresponding power-law profile in the emitted spectrum. The emitted spectrum extends up to the maximum frequency ν_{max}, given by $\nu_{max} \sim \gamma_2^2 \nu_L$.

Since the electrons also absorb photons with energy roughly similar to that which they can emit, a given population of electrons can self-absorb part of the synchrotron emission they produce. The frequency at which the optical depth is ≥ 1 is referred to as the self-absorption frequency ν_t. In this case, depending on whether thermal equilibrium is established or not, the resulting spectrum is $\propto \nu^2$ or $\nu^{\frac{5}{2}}$. Above ν_t, however, the region is optically thin and the spectrum is therefore given by Eq. 2.6

2.1.4 Reflection component

Depending on the geometry of the system and on the position of the disk respect to the observer it is possible to detect the reflection component in the X-ray Binaries. This is due to *Compton reflection* of the the hard X-rays by material in the accretion disk (ionised or neutral). The fraction of the Comptonizing emission from the corona, placed between the NS and the disc, is reprocessed by the surface of the accretion disk producing a broad X-ray bump peaking near 20-40 keV together with fluorescence lines and edges of the most abundant elements (such us the Iron with the k_α line at 6.4 keV). The reflection amplitude, $\Omega/2\pi$, is indicated as the solid angle subtended by

the reflector as seen from the corona. The reflection component is now observed in the spectra of both neutron star and black hole systems. The reflection bump observed in the spectra of some NSs has, usually, a reflection amplitude lower than 0.3. The weakness of this component suggests that the reflector subtends a small solid angle as seem from the corona. This is possible in the hypothesis of a truncated disk is or/and an absention of its inner part or of a highly ionized the accretion disc. In this geometry, a decrease of the inner radius of the disk causes an increase of the solid angle subtended by the reflector [22] [23].

2.2 Spectral states of NS LMXBs

The X-ray Binaries show different spectral states depending on the contribution of the emission components described above.

The NS LMXBs spectra are difficult to understand and the precise origin of the spectral components are still debated.

Observational studies in the ”classical” X-ray band (1-20 keV) resulted in two main models which have been applied and discussed. In the *western model* the spectrum is decomposed in the sum of unsaturated Comptonised spectrum, produced in an inner disk corona, plus a black body originating close to the neutron star surface or the boundary layer between the disk and the neutron star [24]. In the *eastern model* the spectrum consists of the sum of an optically thick multi-temperature disk (locally emitting like a pure black body), plus a black body originating from the neutron star or boundary layers [16].

Observations also in the hard X-ray bands ($>$20 keV) outlined that broad band spectral study has been necessary to model and understand all the components and features. The Hard X-ray spectra extending up to energies of several hundred of keV, that was initially considered a characteristics of the black hole (BH) systems, was then revealed also in the NS systems with the advent of new instrumentations [25].

The actual classification of the LMXBs relies upon the position displayed by individual sources in the X-ray Colour-Colour Diagram (CCD). As already described in section 1.3.2 the atoll sources moves in the X-ray CCDs showing different spectral

states. They moves from the Banana, *Soft* spectral state, to the Island, *Hard* spectral state, passing through intermediate states. These states are distinguished by the different combination of the spectral components together with different timing and also radio properties [13]. During the Soft spectral state almost the total emission is due to the black body emission from the disc, while in the Hard spectral state the disk emission decreases with the rising of the hard emission due to the Comptonization. The transition is often modelled in terms of a gradual decrease of the electron temperature of the Comptonising region, typically in the ranges of 3-10 keV for the Soft states and 10-100 keV for the Hard [23]. In Figure 2.2 are reported as example the Soft and Hard spectral state of the atoll NS LMXBs 4U 1705-44.

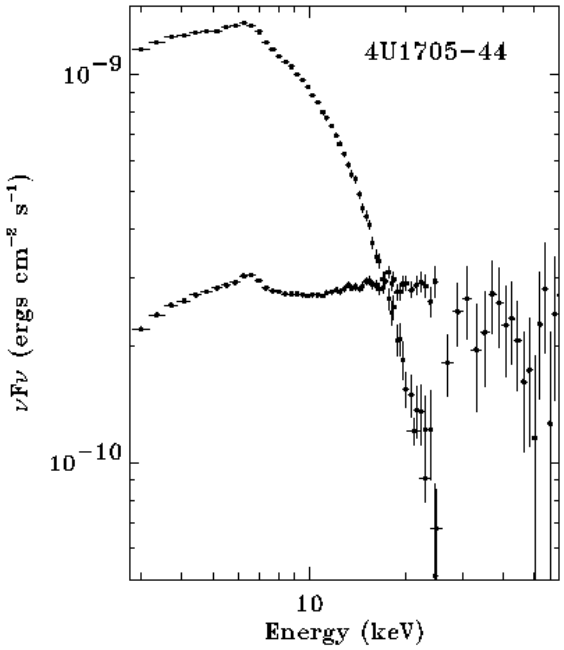

Figure 2.2: Hard and Soft spectral state from 4U 1705-44 as observed by *RXTE* [23].

The changes in the mass accretion rate appears to be the main parameter driving the spectral hardness of atoll sources. In fact $\dot{m}$ should increase from the Island state to the Upper-Banana state. It as been suggested that the second parameter regulating the spectral state transition might be the truncation radius of the optically thick disk [23]. A different geometry of the system in the Soft and Hard spectral states is also

suggested by the reflection component. In fact in the Hard state, the measurements of the total amount of relativistic smearing and the small solid angle of the reflector suggest that the reflector is not extended down to the last stable orbit; on the contrary, in the Soft state the reflection components properties suggest that the reflector extends closer to the central object.

2.3 Why study the high energy emission from NS LMXBs?

The importance of the study of the emission of the NS LMXBs system extended in the hard X-ray band can be summarized as follow:

- **Spectral changes parameters and similarity/differences with Black Hole Binaries (BHBs).**
  The study of the X and hard X-ray temporal behaviour and spectral state changes allows to meausure the variations of the spectral model parameters between the Soft and Hard state. These parameters describes the physics of the accretion disk (black body temperature and radius) and the corona (electrons temperature, plasma optical depth, seed photons temperature). Eventually, the contribute of reflection features can be determined in order to study the physical characteristic of the disk and constrain the geometry of the system.
  Then the results can be compared to the spectral results of the better modelised BHBs.

- **Non thermal emission study.**
  Investigating the high energy band permits to detect in the high energy spectra the possible presence of high energy cut-off; to discern the non thermal nature of the emission, such as syncrotron emission, and the possible correlation with the presence of jets.

The *INTEGRAL* satellite, providing improved sensitivity and imaging capability in hard X-rays (at 100 keV) compared to *BeppoSAX* and *Rossi-XTE*, gives unique opportunity to study and investigate the properties of the spectra of NS LMXBs and in particular the thermal and non-thermal emission of these sources.

2.3.1 Luminosity differences between BH and NS binaries

A criterion to distinguish the black hole or neutron star nature of the compact object of the X-ray Binaries has been searched since ever. The optical observation and the *mass function* estimation represent the *sure* method to identify the nature of the compact star. Unluckily, only rarely it is possible to apply the optical method to the Galactic Binaries, especially for the Low Mass type (as reported in section 1.3).

Before the *SIGMA* time ($\sim$ 90') it was suggested that the presence of the extension of the spectra in the high energy range was indicative of a BH nature for compact object. Later on, it was shown by Barret & Vedrenne (1994) that also the X-ray Bursters emits up to 100-200 keV in their hard state, demonstrating that the use of a high energy emission criterion alone was not valid as possible means of discriminating between BH and NS systems [26]

Barret et al. 1996, 2000, propose a luminosity criterion to distinguish BH and NS systems. They measured the 1-20 keV and 20-200 keV luminosity of a sample of NS and BH systems (optically proved), showing that the X-ray Bursters are clustered in the *X-ray Bursters Box* at low luminosities ranges respect to the BH systems [27] [28] (see Figure 2.3).

It was also suggested that the observation of the broad band spectral shape of the X-ray binaries could be a way to distinguish the nature of the compact object. In particular the electron temperature of the corona appeared to be systematically lower for the NS systems than for BHs ($kT_e \leq 30$ keV vs ≥ 50 keV) [29] [30] [31].

The recent observations of NS LMXBs in the hard X-ray band with *BeppoSAX* and *RXTE* satellites and now with *INTEGRAL* , reject these criteria. In fact the observations show that the X-ray spectral parameters and shape are similar for NS and BH candidate binaries. Moreover the detection of hard X-ray tail and high energy emission from the NS system also, shows that the luminosity criterion is difficult to be applied.

My work summarised in this thesis confirms that the NS system are high energy emitters with spectra extending above 100 keV, and spectral state (especially the Hard state) similar to the BH systems.

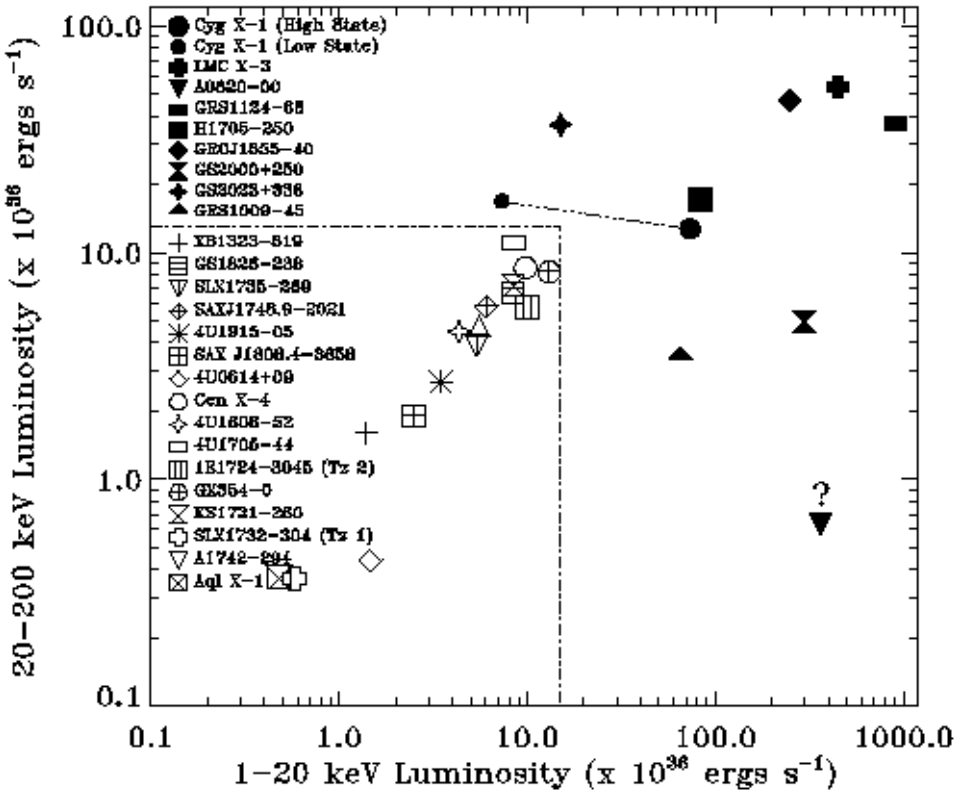

Figure 2.3: The X-ray Bursters Box [28].

2.3.2 Hard tail detection

With the detection, by *BeppoSAX* and later on by *INTEGRAL* , of the first hard X-ray tail of a NSB during Soft state, namely the Z source GX 17+2 [32], the Bursters Box lost its meaning, in fact this source state was out of the Box. Later on, few more NSBs showed the presence of hard X-ray tails [33], [34], [35].

The origin of the tails is currently debated but the fact that these systems are also relatively bright radio sources suggests the hypothesis that the hard X-ray emission have a non-thermal origin. In bright neutron stars the hard tail luminosity represents a small fraction of the source luminosity. This is not the case for black hole systems. This could be related to the additional Compton cooling from the neutron star surface/boundary layer emission. Alternatively, it has also been suggested that these tails may be related to the appearance of a jet. The high energy tail would then result either

from non-thermal Comptonization of disk seed photons or from direct optically thin syncrotron emission of the jet [23].

2.3.3 Radio connection

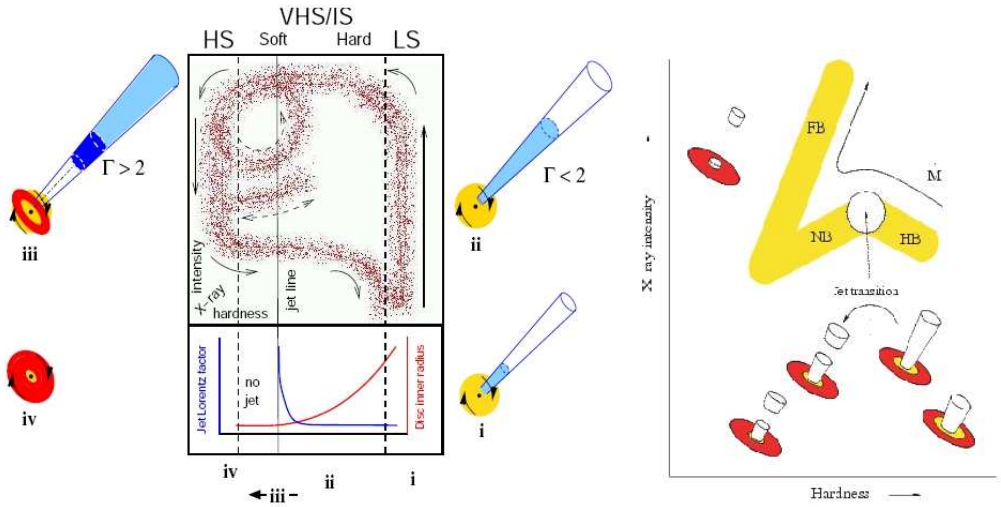

Figure 2.4: Disk-jet coupling for the BHBs and Z sources, taken from [36] and [37].

Recent studies (since 2003 by Fender, Gallo and Belloni [14], [36], [38]) on BHBs in the X-ray and radio bands allow to establish a X-ray and radio connetion, called *disc-jet coupling*. The source behaviour display a cycle hysteresis in the CCD as represented in Figure 2.4. All BH systems which are either in the Hard spectral state, or undergoing a major transient outburst, are associated with a jet formation. On the contrary during the Soft spectral state the radio emission is rapidly quenched.

The similarity of the BH and NS systems behaviour allow us to hypothesize that the analogies could be extended also to the disc-jet coupling, though with some differences.

Up to now the relation of X and radio emission seems to be present also for many Z sources [37]. The prototype Z source Sco X-1 , is known as a variable radio source since the early 1970s [39]. Moreover in 1999 a relativistic jet has been detected. Recently other Z sources have been reported to have radio counterparts with comparable luminosities as Sco X-1 [40]. It was also found for some of them a coupling between

X and radio emission, with a radio behaviour correlated to the position in the X-ray Colour-Colour diagram. This suggests that all the Z sources would have the cycle hysteresis including also the presence of jets (see Figure 2.4).

For the atoll type the X-radio connection has not been reported so far. Radio observations show that atoll sources are less ”radio loud” with respect to the BH systems [37], [41]. In particular Migliari et al. [42] have shown that the atoll source 4U 1728–34 is 30 times less radio luminous then BHs in the same spectral state. The lack of such coupling detection could be due to the low radio luminosity of the atoll sources and/or due to lack of sensitive enough instrumentations.

Given the above, my opinion is that the similarity between BH and NS systems, support the scenario that an hysteresis loop can exist also for NS atolls though with different properties and intensity. The observation of NS spectra with similar behaviour and components of the BH spectra during the radio emission, could give indication that similar processes are present also in the NS systems. So, the recent detection of hard X-ray tails in NS binaries assume special importance. It could be the proof that also these system could emit in the radio band, in particular by jet emission. In Figure 2.5 the atoll sources with the radio observation are reported. Three of them, 4U 1820-30, 4U 1728-34 and 4U 1608-522 are studied in this thesis.

Table 1. Name of the source of our sample, X-ray state (LB = lower banana; IS = island; MB = middle banana; H-OUTB = hard outburst; S-OUTB = soft outburst; ASM/PCA mean = the mean over more than one X-ray state), X-ray flux in the range 2–10 keV, radio flux density at 8.5 GHz, distance to the source in kpc and references.

Source	X-ray state	F_{2-10} ($\times 10^{-9}$ erg cm^{-2} s^{-1})	$F_{8.5}$ (mJy)	D (kpc)	Ref.
		Atoll-type NSs			
4U 1728−34	LB	1.03 ± 0.05	0.5 ± 0.08	4.6	M03, G03
	IS	2.25 ± 0.15	0.6 ± 0.2		
	LB	1.54 ± 0.10	0.33 ± 0.15		
	IS	1.81 ± 0.11	0.62 ± 0.1		
	IS	2.42 ± 0.16	0.11 ± 0.02		
	IS	0.60 ± 0.07	0.09 ± 0.02		
	IS	0.61 ± 0.06	0.11 ± 0.02		
	IS	0.62 ± 0.06	0.15 ± 0.02		
	IS	0.69 ± 0.12	0.16 ± 0.02		
	IS	0.70 ± 0.05	0.09 ± 0.02		
4U 1820−30	MB	8.7	0.10 ± 0.02	7.6	M04, H00
Ser X-1	MB	4.4	0.08 ± 0.02	12.7	M04, JN04
Aql X-1	H-OUTB	0.79	0.210 ± 0.050	5.2	RMD04, JN04
	H-OUTB	1.00	0.214 ± 0.035		
4U 1608−52	IS?	0.93	<0.19	3.3	MF05, JN04
4U 0614−09	IS	0.78	<0.09	<3	MF05, B92
MXB 1730−335	S-OUTB	2.92	0.370 ± 0.030	8.8	R98, M00, K03
	S-OUTB	3.06	0.290 ± 0.030		
	S-OUTB	5.34	0.330 ± 0.050		
		Low-magnetic-field accreting ms X-ray pulsar			
SAX J1808.4−3658	S-OUTB	0.14	0.8 ± 0.18	2.5	GSG99, Z01, R02, R05
	S-OUTB	1.82	0.44 ± 0.06	2.5	
	S-OUTB	0.56	0.44 ± 0.07	2.5	
IGR J00291+5934	S-OUTB	0.62	1.5 ± 0.3	<3?	G05, P04
		Z-type NSs			
Sco X-1	ASM mean	253.80	10 ± 3	2.8	FH00, P89, C76, BFG97
GX 17+2	ASM mean	12.90	1.0 ± 0.3	14	FH00, P89, P88, JN04
GX 349+2	ASM mean	14.39	0.6 ± 0.3	5	FH00, CP91, CS97
Cyg X-2	ASM mean	10.75	0.6 ± 0.2	13.3	FH00, P89, H90, CCH79, JN04
GX 5-1	ASM mean	20.36	1.3 ± 0.3	9.2	FH00, P89
GX 340+0	ASM mean	8.54	0.6 ± 0.3	11	FH00, P93
GX 13+1	PCA mean	18	1.8 ± 0.3	7	FH00, H04, JN04
		High-magnetic-field accreting X-ray pulsars			
X Per	?	0.46	< 0.08	1	MF05, D01
4U 2206+54	?	0.26	< 0.039	3	B05, NR01

References: M03 = Migliari et al. (2003); G03 = Galloway et al. (2003); M04 = Migliari et al. (2004); H00 = Heasley et al. (2000); JN04 = Jonker & Nelemans (2004); RMD04 = Rupen et al. (2004); MF05 = Migliari et al. (2005); B92 = Brandt et al. (1992); R98 = Rutledge et al. (1998); M00 = Moore et al. (2000); K03 = Kuulkers et al. (2003) and references therein; GSG99 = Gaensler et al. (1999); Z01 = in't Zand et al. (2001); R02 = Rupen et al. (2002); R05 = Rupen et al. (2005); G05 = Galloway et al. (2005); P04 = Pooley (2004); FH00 = Fender & Hendry (2000); P89 = Penninx 1989; C76 = Crampton et al. (1976); BFG97 = Bradshaw, Fomalont & Geldzahler (1997); P88 = Penninx et al. (1988); CP91 = Cooke & Ponman (1991); CS97 = Christian & Swank (1997); H90 = Hjellming et al. 1990a; CCH79 = Cowley, Crampton & Hutchings (1979); P93 = Penninx et al. (1993); H04 = Homan et al. (2004); D01 = Delgado-Martí et al. (2001); B05 = Blay et al. (2005); NR01 = Negueruela & Reig (2001).

Figure 2.5: Radio detection of NS Binaries from [37].

Chapter 3

The X and gamma ray observatory *INTEGRAL*

Data used in this thesis are principally from observation with IBIS and JEM-X on board *INTEGRAL* . Whenever possible and usefull we used data from other X-ray mission such us *BeppoSAX* and *RossiXTE*. Description of these missions and the characteristics of their instruments are reported in Appendix **A**.

3.1 The *INTEGRAL* mission

INTEGRAL is the second ESA γ-ray mission after COS-B launched in 1975. It is a medium size mission conceived as part of ESA's Horizon 2000 programme. *INTEGRAL* was launched by a 4 stage PROTON from Baikonur in Kazakhstan on 17^{th} October 2002 and was inserted into a geosynchronous highly eccentric orbit with high perigee in order to have long periods of uninterrupted observation with nearly constant background. *INTEGRAL* is a major milestone in hard X-ray and low energy gamma-ray astronomy after the successful missions SIGMA on GRANAT (France/USSR) and the Compton Gamma-Ray Observatory (NASA). In fact the instruments of its payload cover a wide energy range in the hard X-rays and soft gamma-rays bands (15 keV - 10 MeV) with good sensitivity, energy and angular resolution.

INTEGRAL scientific goals are met by fine spectroscopy with imaging capability

and accurate positioning of celestial sources. Fine spectroscopy over the entire energy range permits spectral features to be uniquely identified and line profiles to be determined for physical studies of the source region.

The fine imaging capability within a large field of view permits an accurate location and hence identification of the gamma-ray emitting objects with counterparts at other wavelengths. Large field of view provides considerable serendipitous science which is very important for an observatory-class mission.

The *INTEGRAL* mission, togheter with the ESA *XMM-Newton* one, has been recently extended to be operative up to December 2012, because of the excellent scientific results. [43].

3.1.1 Observations and goals

Observing Programme

Most of the observing time, from 65% of the total time in the first year to 75% for subsequent years, is devoted to the scientific community. Typical observations last from 100 ks up to about two weeks, depending on the target or sky region. Proposals for observations are selected on their scientific merit only by a Time Allocation Committee. These selected observations form the basis of the General Programme.

The remaining fraction of the total observing time is the Core Programme [44], reserved for scientific institutes which have developed and delivered instruments (the *INTEGRAL* Science Working Team, ISWT) and for the scientific Data Centre (guaranteed PI time). During the nominal period of the mission, the Core Programme consisted of three parts with a dedicated exposure time per year:

- Frequent scans of the galactic plane (Galactic Plane Survey, GPS): these scans provide a periodic monitor of the gamma-ray sky to search for transient sources and monitoring the persistent ones. The scans are performed weekly with a “slew and stare ” manoeuvre of the spacecraft along the seasonally visible part of the galactic plane within a galactic latitude of $\pm 10^{\circ}$.

- Deep Exposure of the galactic central radian (Galactic Central Deep Exposure,

GCDE): has the aim of mapping line emission and diffuse emission of the central galactic region and to perform deep imaging and spectroscopic studies of the galactic bulge and of the single point sources around the galactic centre zone.

- Target of opportunity (ToO), pointed observations of selected sources.

One of the key outcome of the *INTEGRAL* Core Program is mapping the soft gamma-ray sky with particular interest in the galactic plane regions of the galaxy from 20 keV up to 1 MeV.

Within the new Key Program strategy, started after the mission extension to cover the period 2008-2012, only specific interesting zones of the galactic plane, not covered enough, will be the target of observations.

Observing modes

In order to minimize systematic effects taking place in the the two main instruments, SPI and IBIS (see Section 3.2) due to spatial and temporal background variations, a controlled and systematic spacecraft dithering manoeuvre was required.

This manoeuvre consists of several off-axis pointings of the spacecraft pointing axis from the target in steps of 2 degrees. The integration time for each pointing could vary in the range 0.5–1 hour and time is adjusted in a way so that always multiples of a complete dither pattern are executed for each observation. Two main, different pointing patterns are currently used:

- Hexagonal dither pattern: this consists of a hexagonal pattern around the nominal target location (1 source on-axis pointing, 6 off-source pointings, each 2 degrees apart).

- Rectangular, or 5×5, dither pattern: this consists of a square pattern around the nominal target location (1 source on-axis pointing, 24 off-source pointings, each 2 degrees apart). This is the nominal pattern for the best use of both SPI and IBIS.

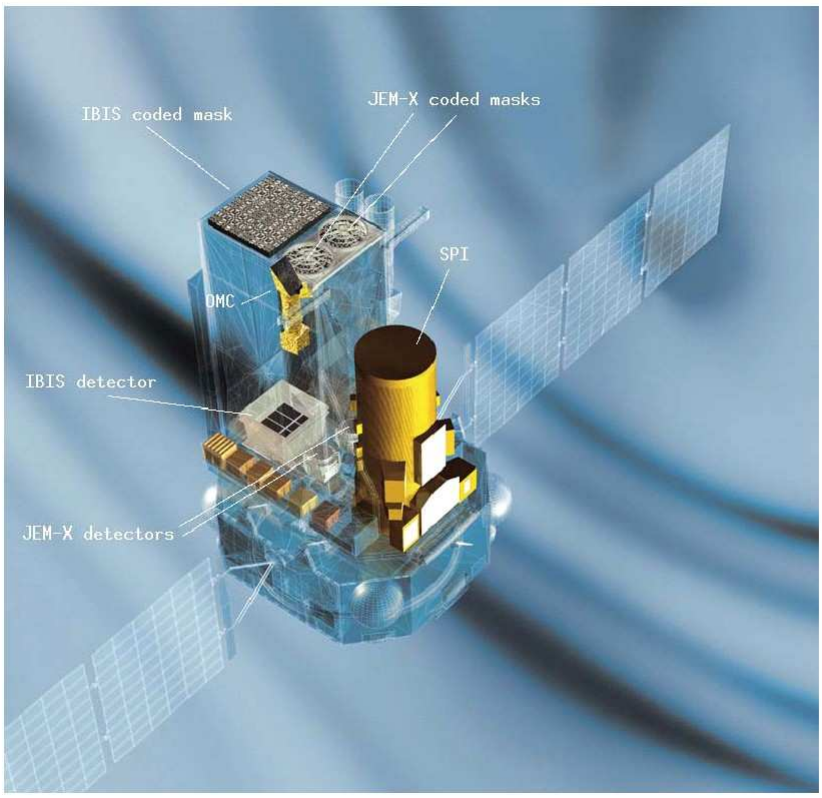

Figure 3.1: An *INTEGRAL* payload modules view.

3.2 The instruments on-board *INTEGRAL*

The two main gamma-ray instruments, integrated in the *INTEGRAL* payload (Fig. 3.1), have both spectral and angular resolution, but they are differently optimised in order to complement each other and to achieve overall excellent performance. The Spectrometer, the Imager as well as the X-ray monitor have a common principle of operation: they are all coded aperture mask telescopes.

3.2.1 Coded mask telescopes

An X- and γ-ray telescope works, generally, outside the earth atmosphere and is designed to collect as much information as possible on the incident radiation emitted from a source. It should have the capability to provide information on the position of

the sources, on its flux variation and on its energy distribution.

The techniques used for the source imaging depends on the energy range considered.

The X-rays can be reflected from surfaces, but at very small incidence angles. The critical grazing angle (the maximum incidence angle at which reflection can occur), is inversely proportional to the photon energy, so that reflecting high-energy X-rays requires very small incidence angles. This makes designing practical mirrors very difficult. Up to soft X-rays (< 20 keV), methods, using multiple reflections, are available to increase the typical reflection angles and permit to focus the X-rays on the detector, as for example, a combination of a paraboloid mirror and an hyperboloid mirror. This solution was used in satellites like *HEAO-2* and now *Chandra*.

It is not easy to focus a γ-ray photon because it passes through most of materials and thus cannot be simply reflected by a mirror like optical photons. For gamma-ray observations one of the commonly techniques use the coded aperture masks system.

This imaging techniques employs straight-line ray optics that offer the opportunity to image at higher photon energies and over larger FOV's [45]. The characteristic of this techniques is that the direction of the incoming rays is, before detection, encoded, so the image of the sky has to be reconstructed by decoding the observation afterward [46].

This method of producing sky images is a two-step, indirect procedure in contrast to the direct, one-step, imaging procedure of focusing techniques. These alternative techniques are referred to as multiplexing techniques, for which, for equal collecting areas, the sensitivity of a focusing instrument is always better. Multiplexing techniques can be divided into two classes: those based on temporal and those on spatial multiplexing [45].

In a spatial sensitive coded-mask telescope such as IBIS, the imager on board *INTEGRAL* satellite, the imaging system and concept is shown in Fig. 3.2. Every source within the field of view projects a shadow of the aperture onto the detection plane.

For any particular telescope geometry, the field of view consists of two different zones: The Fully Coded Field of view (FCFOV) in which the detected flux is completely modulated by the mask, and the Partially Coded Field of View (PCFOV) in

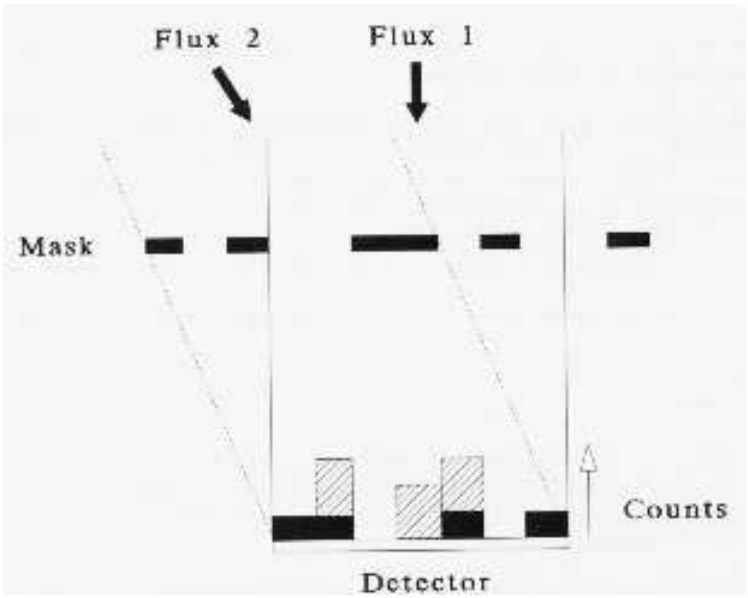

Figure 3.2: Schematic diagram illustrating the working principle of a coded aperture camera: the recorded count rate in each pixel of the detection plane is the summation of contributions from each source flux modulated by the mask.

which the detected photons are coded only by a fraction of the mask.

The angular resolution, dθ, of a coded mask telescope depends on the ratio between the mask element size, C, and the mask-detector distance, H. Each peak in the deconvolved image has angular extent (FWHM) of approximately the size of C/H. For point sources and no source confusion, the parameter actually driving the imaging performance is the Point Source Location Accuracy (PSLA). The theoretical PSLA is limited by the spatial resolution of the detector array.

$$PSLA = \arctan(d/H)/n \tag{3.1}$$

with d the detector inter-pixel separation and n the Signal to Noise ratio (S/N). [43].

3.2.2 The gamma-ray imager IBIS

IBIS, Imager on Board the *INTEGRAL* Satellite [47], provides diagnostic capabilities of fine imaging (12 arcmin Full Width Half Maximum). The source location accuracy

is of 30 arcsec for strong sources, the FOV is $19^\circ \times 19^\circ$ (Full Width to Half Response) with a FCFOV of $9^\circ \times 9^\circ$. The detection unit is composed of two gamma-ray cameras separated by 10 cm:

- ISGRI (*INTEGRAL* Soft Gamma-Ray Imager), covering the range from 15 keV to 1 MeV, has a detection plane made of 16384 physically independent cadmium telluride semiconductor crystals organized in eight modules [48].
- PICsIT (Pixilated CsI Telescope) covering the range from 170 keV to 10 MeV, made of 4096 cesium iodide crystal scintillators [49].

Photons are detected by IBIS in three modes: detection on ISGRI, detection on PICsIT, and detection on the two layers (Compton mode). Table 3.1 shows the principal IBIS scientific capabilites.

Two anti-coincidence shields protect the detector from external radiation:

- a passive shield composed by an “hopper ” unit (truncated pyramid on the top of the ISGRI detector) and a “tube ” made of four walls closing the aperture down to the hopper level. The passive shielding is designed to reduce the celestial diffuse background component; it becomes transparent above 200 keV;
- an active anti-coincidence shield, the VETO anti-coincidence system that is composed of 16 independent modules, each made with two large BGO crystals. This ensures a substantial reduction of the background due to the induced photons and hadronic component, enhancing the detector sensitivity. Measured over the whole energy range, the VETO system provides a background suppression effect of $\sim 50\%$ for ISGRI and $\sim 40\%$ for PICsIT.

The basic design of the IBIS mask (Figure 3.3 top) is a Modified Uniformly Redundant Array (MURA)[1] of 53×53 elements. This pattern, reiterated four times and cut on the borders, provides the IBIS mask of 95×95 individual square cells. Half of them are in tungsten (16 mm thickness) offering a 70% opacity at 1.5 MeV; the other

[1]For design and properties of MURA pattern, see Gottesman & Fenimore (1989)

Table 3.1: An overview of the IBIS scientific capabilities.

Energy Range	15 keV–10 MeV
Continuum sensitivity, at 3σ and 10^6 s integration (ph cm^{-2} s^{-1} keV^{-1})	2.3×10^{-6} @ 100 keV 1.6×10^{-6} @ 1 MeV
Line sensitivity, at 3σ and 10^6 s integration (ph cm^{-2} s^{-1})	1.8×10^{-5} @ 100 keV 3.8×10^{-4} @ 1 MeV
Energy Resolution (FWHM %)	8% at 100 keV ISGRI 10% at 1 MeV PCSIT
Angular resolution (FWHM)	$\sim 12'$
Point Source Location Accuracy (90 % error radius)	30" @ 100 keV (50 σ source) 3' @ 100 keV (5 σ source) 5'-10' @ 1 MeV (5 σ source)
Timing accuracy	61 μs - 1 hr
Field of View	$9^\circ\times9^\circ$ (fully coded) $29^\circ\times29^\circ$ (zero response)

half are opened and covered by a carbon fibre with an off-axis transparency of 60% at 20 keV.

The FCFOV size, for which sensitivity is the nominal one, is $9^\circ \times 9^\circ$; it becomes then 50% at 19°, and response decreases to zero at 29°. The angular resolution is $d\theta = \arctan(C/H) = 12'$ with $C = 11.2$ and $H = 3133$ mm.

Each pixel of the ISGRI camera is a spectrometer chain with its own characteristics. The spectral performance of the camera depends therefore critically on the alignment of the pixel gains and offset. The alignment is performed in two steps: the electronics allow for a rough alignment and then a fine software correction must be applied.

In principle, the amplitude of the pulse yields the energy of the incident photon. However, above 60 keV the energy is a function of both pulse height and rise time, because of the charge trapping inside the CdTe material. The longer the rise time, the more important are the charge losses. In order to determine the energy for each photon, raw data are corrected on-ground using Look Up Tables (LUTs) carried out by calibrations. In addition, the resulting line profile is no longer a Gaussian, but more similar to a Lorentzian. ISGRI energy resolution (Tab. 3.1) depends on the operating

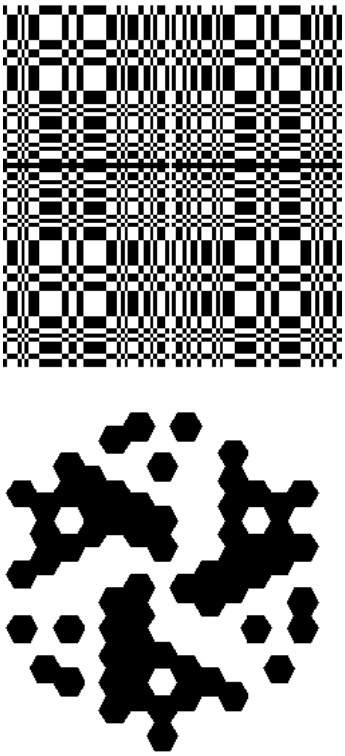

Figure 3.3: IBIS and SPI coded mask patterns

temperature, and also on the bias voltage.

3.2.3 The spectrometer SPI

The spectrometer SPI (SPectrometer on *INTEGRAL*) [50] provides spectral analysis of gamma-ray point sources as well as extended sources over an energy range between 20 keV and 8 MeV.

The field of view is 16 degrees with an angular resolution of 2 degrees. The SPI detector is composed of an array of 19 hexagonal high purity germanium detectors. Table 3.2 summarises the principal SPI scientific capabilites. Emission lines from radioactive nuclei, such as ^{26}Al, are the main observational subjects of the spectrometer SPI.

The SPI Mask, (Figure 3.3 bottom) placed 1.7 m above the 19 germanium detectors, is a Hexagonal Uniformly Redundant Array (HURA) made up of 127 hexagonal

Table 3.2: An overview of the SPI scientific capabilities.

Energy Range	20 keV – 8 MeV
Continuum sensitivity, at 3σ and 10^6 s integration (ph cm^{-2} s^{-1} MeV^{-1})	1.5×10^{-4} @ 1MeV
Line sensitivity, at 3σ and 10^6 s integration (ph cm^{-2} s^{-1})	5.1×10^{-6} @ 1MeV 2.8×10^{-5} @ 511 keV
Energy Resolution (FWHM %)	2.33 keV @ 1.33 MeV
Angular resolution (FWHM)	$\sim 2.0^\circ$
Timing accuracy (3σ)	0.129 ms
Field of View	16° (corner to corner) (fully coded)

cells of which 63 are opaque to the radiation (95 % opaque @ 1 MeV) and 64 are transparent to gamma-radiation (60 % transparent @ 20 keV & 80 % transparent @ 60 keV). The pattern has a 120° symmetry and the cells are of size 60 mm side-to-side (i.e. short axis) by 67.55 (i.e. long axis) forming a hexagonal-shaped coded area of overall dimensions 692.72 mm (i.e. short axis) by 770 mm (i.e. long axis). The opaque elements are made of 3 cm thick tungsten.

3.2.4 The X-ray monitor JEM-X

Table 3.3: An overview of the JEM-X scientific capabilities.

Energy Range	3 keV–35 keV
Continuum sensitivity, at 3σ and 10^6 s integration (ph cm^{-2} s^{-1} keV^{-1})	1.3×10^{-5} @ 6 keV
Line sensitivity, at 3σ and 10^6 s integration	1.7×10^{-5} (ph cm^{-2} s^{-1}) @ 6keV
Spectral Resolution	1.2 keV @ 10 keV
Angular resolution (FWHM)	$\sim$ 3 arcmin
Point Source Location Accuracy	$<$ 30” (10 σ source)
Timing accuracy (3σ)	122 μs
Field of View	4.8° (fully coded)

The JEM-X monitor [51] works simultaneously with the other instruments in the energy range between 3 and 35 keV with an angular resolution of one arcmin and a FCFOV of 4.8 °. The coded mask is placed 3.4 m above the detector. The detector consists of two identical chambers filled with Xenon at a pressure of 1.5 bar (see Table 3.3).

3.2.5 The optical monitor OMC

The Optical Monitoring Camera (OMC) is a CCD detector of 1024 $\times$ 1024 pixels located in the focal plane of a 50 mm lens with a Visible (V) filter [52]. The size of each pixel is 13 $\times$ 13 μm covering a field of 17.6 x 17.6 arcsec. The total field of view of the OMC camera is of 5 $\times$ 5 degrees. The camera is placed on top of the satellite and is sensitive to stars of magnitude up to about 18. [43].

Chapter 4

The *INTEGRAL* data analysis method

My thesis work consisted on the scientific analysis of a sample of NS LMXBs observed with *INTEGRAL* . In these chapter I summarize informations about the *INTEGRAL* data analysis method that has been used and the scientific approach that has been applied.

4.0.6 The NS LMXBs sample

The analysed sources rapresent a sample of NS LMXBs, Atoll type and bursters, with different characteristics. Some of them are transient, some of them are persistent, and some are located in Globular Clusters. They are: 4U 1820–30, 4U 1608–522, 4U 1722–38, 4U 1812–12, 4U 1722–30, XB 1832–330, 4U 1254–690. Most of these sources are located in the Galactic Centre region and the *INTEGRAL* Core Program of the first four years of operation devoted 6 milion seconds to the GCDE. This implies that starting from January 2003 the sources on this region have been monitored longly though not continuously.

4.0.7 *INTEGRAL* data analysis

INTEGRAL data are organized into pointings called Science Windows (ScWs), lasting about 2000 seconds. During the scientific analysis of a source, all the Science Windows belonging to the same observation are collected to form the ”Observation

Group", available from *INTEGRAL* Science Data Centre (ISDC) browes on-line page[1]. In our analysis, the public and private-ISWT pointings available and that include the source have been selected.

In 2006 the Galactic Centre region was available only through observation via Announcement of Opportunities (AO). To get propertary data and proceed with my studies, I proposed and got a sample of Atoll LMXBs (*INTEGRAL* AO4 and AO5). Some of the sources proposed for observation are transient and up to now didn't show outburst and persisted in quiescent state, the other ones were detected and analysed (4U 1820–30, XB 1832–330, 4U 1722–30).

Data were processed using the v. 4.2 or v. 5.1 version of the Off-Line Scientific Analysis (OSA) [53] software released by the ISDC [54]. The scientific analysis script (`ibis_science_analysis`) consists on three main step: the first one gives as result the images in the selected ranges of energy; the second one is the spectral extraction of the sources detected in the field of view; last task consists on the light curve extraction.

IBIS and JEM-X are coded mask telescope instruments, so in order to have a good spectral extraction, it is important to recognize all the source detected in the instrument Field of View and compose a catalog including these sources (`user_cat.fits`) [55].

For the spectral extraction, all the available data for which the source was within the IBIS/ISGRI and JEM-X fully coded FOV ($4.5^\circ \times 4.5^\circ$; $2.4^\circ \times 2.4^\circ$) has been analysed, so that the flux evaluation is not affected by calibration uncertainties in the off-axis response.

All the results (in FITS format) have been elaborated via FTOOLs and with the use of IDL language programming. In particular, the spectral analysis has been performed with the XSPEC package v. 11.3.2. A 2% systematic errors to both JEM-X and ISGRI data sets has been added[2]. Fluxes have been normalized to IBIS/ISGRI value. The standard 2048 channels response matrix, logarithmically rebinned to 64 channels has been used for the spectral analysis with IBIS; and the standard matrix has been used

[1] http://isdc.unige.ch/index.cgi?Data+browse

[2] http://isdc.unige.ch/?Support+documents

for JEM-X.

We used the so-called νF_ν representation for the energy spectra. The motivation for this choice is provided by a mathematic consideration. Namely, any differential dependence, e.g., flux per unit energy, $\mathrm{d}F/\mathrm{d}E$, equivalently expressed as $F(E)$ or F_E, can be plotted as $F(E)$ vs E. However, when we plot F vs. $\log E$, it should be $F(\log E) = \mathrm{d}F/\mathrm{d}\log E$, i.e., $F(E)(\mathrm{d}\log E/\mathrm{d}E)^{-1} \propto EF(E)$. This gives F per a logarithmic interval of E. Graphically, $EF(E)\mathrm{d}\log E$ represents the area under the curve, F, in a plot vs $\log E$. Then, a peak in this representation shows us at which photon energy range most of the power of the source is radiated. An added benefit of this representation is that plots vs. photon energy or wavelength become identical, as $\lambda F(\lambda) = EF(E)$ [56]. We also plot the energy spectra with the same length per decade on each axis, in order to enable direct comparison of the shape spectra on different figures.

Figure 4.1 shows the IBIS mosaic image (i.e. the image composes by each single pointing image) of the Galactic centre with a label for the sources analysed in this thesis.

4.0.8 Scientific approach applied

To check the different spectral component of each spectral state, we are interested in the timing and spectral behaviour of NS LMXBs. To search for possible flux variations it is important to analyse in detail the behaviour of each source. They have been individually and independently analysed, but the same scientific approach has been applied to all of them. This consists on the combination of three method of analysis: *Temporal*, using light curves, *Photometric*, by deriving the hardness-intensity diagrams and *Spectral*, with spectral fitting.

Data from other satellites, such as *RXTE* and *BeppoSAX* has been used when it has been usefull and if available. The *RXTE*/ASM[3] public data has been used in order to have a monitoring of the source flux behaviour in the soft 1-12 keV band.

[3] http://xte.mit.edu/ASM_lc.html.

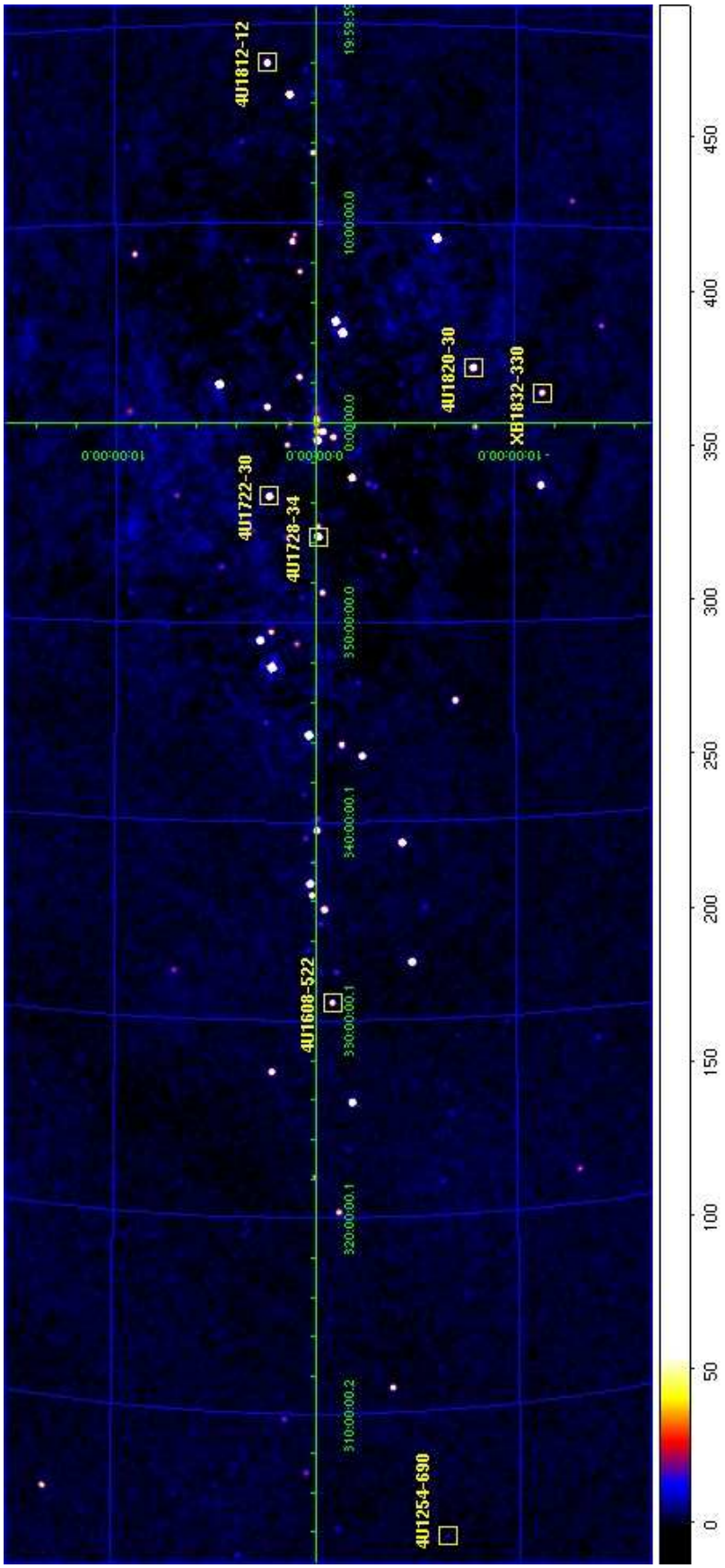

Figure 4.1: IBIS mosaic image of the galactic center in the 20-100 keV energy band, with the analysed sources showed in the yellow boxes.

Temporal analysis

The temporal study consist on building up the light curves (flux vs time) in different energy ranges. The temporal bin chosen is a single pointing except for the bursts events which require shorter time down to 1 second. The energy ranges chosen to check flux variations are either 20-40, 40-100 keV, or 20-30, 30-60, 60-120 keV for IBIS; and 4-10, 10-20 keV for JEM-X.

Usually, as it is used in X-ray Astrophysic, the source fluxes are indicated in unit of Crab flux [4]. This is because the Crab is the only persistent not variable source acting as "standard candle" reference for instrument calibration. In particular this is necessary for the soft JEM-X band, for which the flux from sources are computed in Crab rate with a conversion factor for each different calibration periods.

Photometric analysis

To search for fluxes variation which are correlated with spectral variation, it is usefull to set-up the *hardness ratio* of different energy bands. It consists on the flux differences between the photon counts in two broad band: "hard" band to the "soft" band.

Fluxes variations are also recognized with the constructions of the *Hardness-Intensity diagram* or *Color-Intensity diagram*, where with "X-ray color" we mean the hardness ratio between two energy bands, and with "intensity" the total count rate in the X-ray broad band. By computing two X-ray colors (a "hard" color in an higher energy band and a "soft" color in a lower band) and plotting one vs the other, we represent the *Color-Color diagram* with similar results. When a source changes its spectral state it moves through the diagrams.

With *INTEGRAL* we have a *Very Hard* Color-Intensity diagrams because of the harder energy band available ($>$20 keV), different from the usually soft X-ray band used from other satellites ($<$10 keV).

[4] From IBIS/ISGRI the Crab flux in the 20-40 keV band correspond to 7.5×10^{-9} ergs cm^{-2} s^{-1}

Spectral analysis

Last step of our method is the spectral analysis. The results of the temporal and photometric analysis allow to understand if the sources changes its emission or stays in the same spectral state. We combine in the same spectrum all the pointings with the same spectral state that for some source is equal to the total observation period.

In next chapter spectral results are presented and discussed for each source. For the spectral analysis different models to fit the data have been used.

These model are the Comptonization models, such us `CompTT` [57] and in some cases `CompPS` [58]; the black body, or disk black body component `diskbb` [16]; in some case has been added also the reflection componenet, `reflect` [59].

Here a summary of the physical description of the parameters of the models is reported, while for details on models see the indicated references.

The Comptonization models have three main parameters: kT_e, the temperature of the electrons plasma giving rise to the corona i.e. a hot region near the disk; the optical depth of this region, τ; and kT_0, the Wien temperature of the soft photons, also known as input seeds photons, which are upscattered to higher energies by the hot electrons of the corona.

The simple black body model is characterized by the temperature of the black body, kT_{bb}. The diskbb black body model, `diskbb`, has as parameters kT_{in}, the temperature at the inner disk radius, R_{in}, corresponding to the inner last stable orbit of the material of the disk (the temperature of the disk depends on the radius as $T \propto R^{-\frac{3}{4}}$, see section 2.1.1). The diskbb normalization correspond to $K = \{(R_{in}/km)/(D/10kpc)\}^2 cos\theta$ where D is the distance to the source and θ is the angle of the disk.

`Reflect` is a convolution model for reflection from neutral material according to the method of Magdziarz & Zdziarski, 1995, [59] and the physical parameter is the reflection scaling factor.

Chapter 5

X- and soft Gamma-ray behaviour of atoll sources analysed with *INTEGRAL*

5.1 4U 1820–30

4U 1820–30 is a low mass X-ray binary seen at $0.66''$ from the centre of the globular cluster NGC 6624. It was the first identified source of type-I X-ray bursts [69]. Distance has been estimated as $d \simeq 5.8 - 8.0$ kpc (e.g., [74]; [11]). Kuulkers et al. (2003) [11] derived a $d = 7.6 \pm 0.4$ kpc compatible with the peak X-ray burst luminosity being a standard candle in their sample of sources, and equal to the Eddington limit for He. The binary system consists of a He white dwarf with mass of $0.06 - 0.08 M_{\odot}$ [73] and a neutron star, with the mass estimated by Shaposhnikov & Titarchuk as $\sim 1.3 M_{\odot}$, orbiting at short period of 11.4 minutes [78]. In X-rays, 4U 1820-30 is classified as an atoll [12]. However, its flux variation between the soft (banana) to the hard (island) state are quasi-periodic at $\sim$170 d ([72], [77], [80]), that has been proposed to be due to tidal effects of a more remote third star [64], [88]. X-ray bursts occur only at low flux levels and the detected kHz Quasi Periodic Oscillations are correlated with the flux, demonstrating that the variability is due to an intrinsic change of the source luminosity (and the accretion rate) rather than to variable either obscuration or viewing

angle of an anisotropic emitter [65] [89]. X-ray spectra of the source from *RXTE* and *BeppoSAX* were modelled by thermal Comptonization with or without an additional blackbody ([63], [76], [41]).

5.1.1 *INTEGRAL* observations

We studied the source in the 4–200 keV energy range with the JEM-X [51] and IBIS [47] instruments on board the *INTEGRAL* satellite [82], collected during the GCDE program [83]. This yields 308 and 51 ScWs for IBIS and JEM-X respectively, during revolutions 50–363. Thanks to the *INTEGRAL* analysis we detected for the first time X-ray emission above 50 keV from 4U 1820-30 in a Hard spectral state. We report in the next sections the obtained results [127].

5.1.2 Light curves and hardness–intensity diagrams

Figure 5.1 shows the light curves of the monitoring period (2003 March 12–2005 October 5) from soft to hard X-rays (4–10, 10–20 keV bands from JEM-X and 20–30, 30–60, 60–120 keV with IBIS/ISGRI), as well as the corresponding *RXTE*/ASM light curve. The ∼170-d quasi-periodic variability can be seen in the ASM data. The *INTEGRAL* light curves are marked with vertical lines to identify five epochs (A, B, C, D, E) during which we have performed detailed spectral analysis (see Table 5.1). Epoch A corresponds to the joint IBIS and JEM-X count rate maximum (∼530 mCrab at 4–10 keV). Epoch C corresponds to the minimum of the 4–10 keV count rate (∼100 mCrab), but to high count rates from 20 to 60 keV, implying a spectral hardening across the 4–60 keV band. We also studied epochs before (B), and after that event (D, E).

Figure 5.2 shows hardness–intensity diagrams with data from JEM-X (a) and IBIS/JEM-X (b) (for simultaneous pointing and when possible because of different FOV). In Figures 5.2 we can see the banana state, forming a nearly horizontal bands across the A, B, D, E epochs. Thus, the source evolution is mostly in the flux, with the 4–20 keV spectral shape nearly constant. The upper part of the red points (epoch C) in Figure 5.2(a) corresponds to the island state. In this case the 4–20 keV flux is almost constant

while the hardness shows large changes.

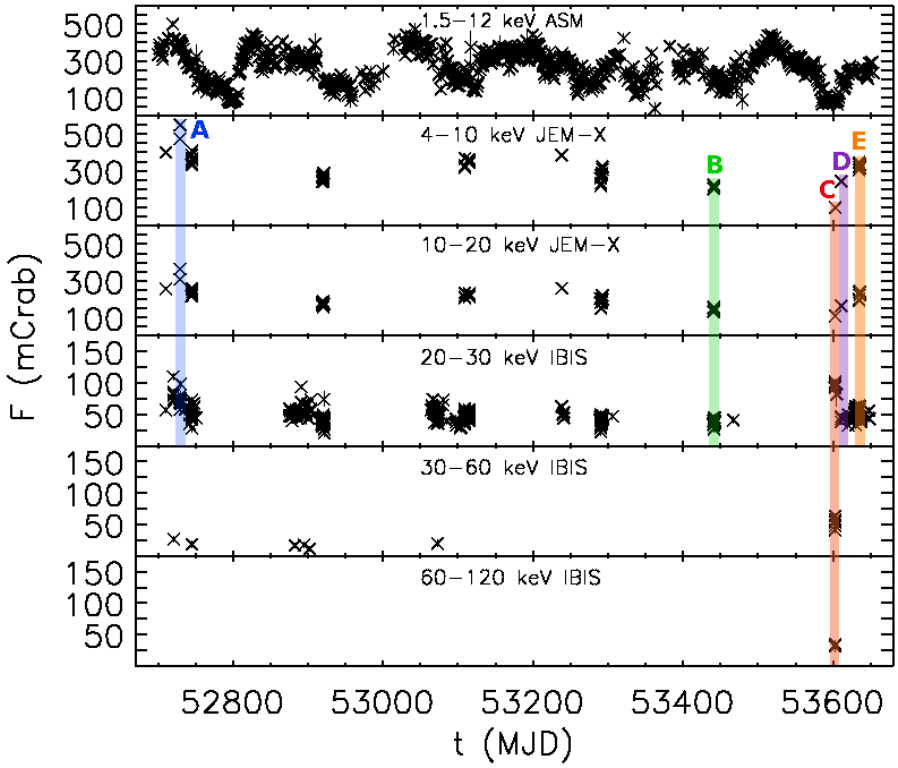

Figure 5.1: The 2003–2005 light curves of 4U 1820–30, with the detector count rate in each band given with respect to the corresponding Crab count rate. The panels are marked with the energy range and detector, and present the *INTEGRAL* ScW data points except for the top panel, which gives the *RXTE*/ASM 1-day averages. The colored lines mark the data sets (A, B, C, D, E) used for joint IBIS and JEM-X spectral fits.

This indicates spectral pivoting somewhere in this energy band. Figure 5.2(b) allows us to study spectral variability of the source in the energy band 10–30 keV, grater than that usual one. In this diagram, we see similar behaviour in the horizontal banana state, while there is only one ScW for the island state, with a large hard color. These findings are confirmed by spectral analysis as discussed below.

5.1.3 Spectral analysis

Data of the five epochs (see Table 5.1) have been fitted with a number of models and also combinating different ones, namely, thermal and hybrid Comptonization, black-

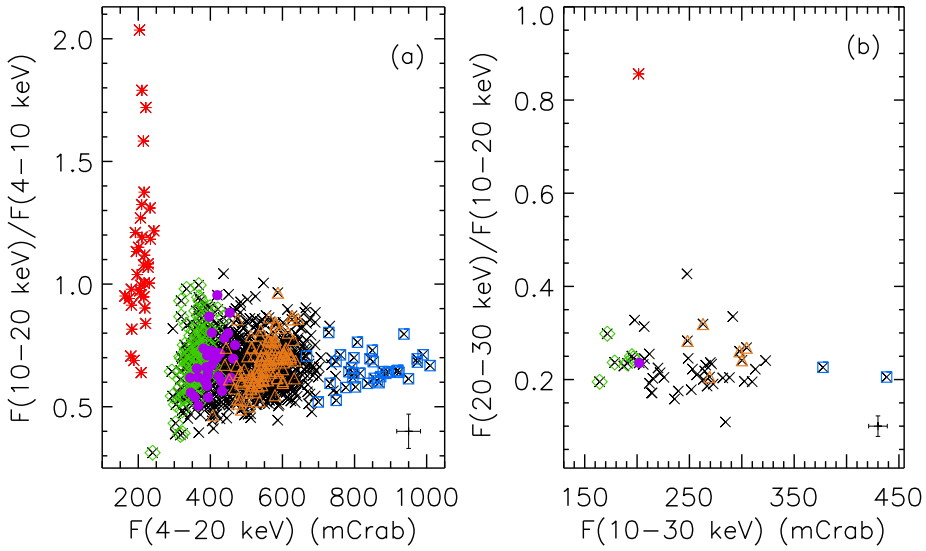

Figure 5.2: (a) Hard color–intensity diagram of 4U 1820–30; each point corresponds to 100 s. (b) Very hard color–intensity diagram; each point corresponds to a ScW. The colors identify the A–E data sets, see Table 5.1 and Figure 5.1. The typical error bars are shown at the bottom right corners.

body, disk blackbody and a power law, all absorbed by the interstellar medium at $N_{\rm H} = 3 \times 10^{21}$ cm^{-2} [63].

Soft states

A thermal Comptonization model, `CompTT` [57], sufficiently model the spectra of the banana states (A, B, D, E). We obtain an electron temperature, $kT_{\rm e} \simeq 2.7$–3.1 keV, and optical depth $\tau \simeq 6$–7, as reported in Table 5.2. This is consistent with the *Hard* Colour-Intensity diagram, where we detected spectral changes mostly in flux values (most likely proportional to the accretion rate) and only slightly in their shape. The temperatures of the seed photons (Table 5.2) have been frozen at their best-fit values, because the operative range is well above those values. The data, model, and residuals for the spectrum A are shown in Figure 5.3*a*, *b*, and all unabsorbed models, in Figure 5.4. This spectrum is the soft spectra characterized by highest flux and unabsorbed bolometric luminosity of $7.7 \times 10^{37} (d/5.8\,{\rm kpc})^2$ erg s^{-1}).

An addition of a blackbody component does not significantly improve the fits (al-

Table 5.1: The log of the data used for spectral fitting. The indicated colors are used in the light curves, Figure 5.1, and hardness–intensity plots, Figure 5.2.

data set	Time (MJD) start−stop	rev. #	Exposure (ks) IBIS ; JEM-X[a]	Obs. type
A (blue)	52729.2−52729.5	56	6.7 ; 3.7	GCDE
B (green)	53440.6−53442.3	294	1.9 ; 1.3	GCDE
C (red)	53602.4−53603.3	348	1.8 ; 3.5	ToO[b]
D (purple)	53610.9−53620.2	351	1.2 ; 3.5	ToO[b], GCDE
E (orange)	53634.8−53635.5	359	1.3 ; 1.2	GCDE

[a] JEM-X2 for the A obs. and JEM-X1 for the B-E obs.
[b] AO3 target-of-opportunity observation, PI P. Goldoni.

though its presence is hinted by the negative residuals at the lowest energies, Figure 5.3*b*), and thus the confidence ranges of the temperature, $kT_{\rm bb}$, are not constrained. Nevertheless, we find $kT_{\rm bb} \simeq 1.5$–2.4 keV at the best fits, in agreement with previous study of Bloser et al. (2000) [63].

Hard state

The spectrum of the island state (C, red) shows an evident excess above 50 keV that cannot be fitted by thermal Comptonization only, as shown in Figure 5.3*e* (value for χ^2_r is 1.6 with 59 d.o.f.). An addition of a soft ($\Gamma \simeq 2.4$) power law improves the fit significantly ($\chi^2_r = 1.0$, see Figures 5.3*c*, *d*), with a chance probability from the F-test of 6.3×10^{-7} [62]. The parameters of the thermal plasma are also different from those for the banana state, with a higher $kT_{\rm e}$ ($\simeq 6$ keV), and a lower τ ($\simeq 4$) (see Table 5.2). Figure 5.4 shows the unabsorbed spectrum with the two components.

By adding a disk blackbody component, `diskbb` [16] to the thermal Compton model, we have also obtained a good fit, with $\chi^2_r = 1.0$. However, the required inner temperature, $kT_{\rm in} \simeq 5.4$ keV, is clearly unphysical (see 2.1.1). Whereas adding a single blackbody gave a worse fit, as well as an unphysically high temperature, $\simeq 4$ keV.

The island-state data have been fitted also with the highly-accurate Comptonization model `CompPS` [58]. We assumed here spherical geometry of the Comptonizing

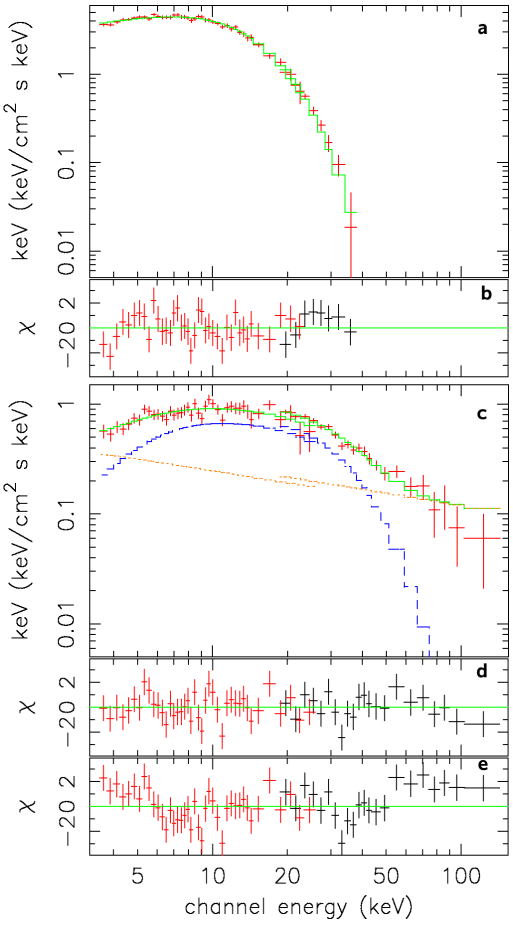

Figure 5.3: Data, models and residuals of the Soft spectrum A (*a*, *b*) and the Hard spectrum C (*c*, *d*) fitted by thermal Comptonization without and with, respectively, a power law component. The panel *e* shows the residuals for the spectrum C fitted without the power law component. The high energy excess at ≥ 50 keV is clearly visible.

plasma. Also, we have taken into account Compton reflection [59] detected in other atolls (e.g., [85], [28], [67]), as well as a disk blackbody.

- We have obtained a very good fit, χ^2_r(d.o.f.)$= 0.92(54)$ for a purely-thermal Comptonizing plasma with $kT_{\rm e} \simeq 55$ keV and $\tau \simeq 0.6$, and the solid angle subtended by reflector of $\Omega/2\pi \simeq 0.69$ (assuming the source inclination of $i = 60^\circ$). The bolometric luminosity for this model is $1.8 \times 10^{37} (d/5.8\,{\rm kpc})^2$ erg s^{-1}. However, similar to the problem with the model using CompTT (see above), the inner disk temperature is rather high, $kT_{\rm in} \simeq 2.4$ keV, as well as the temper-

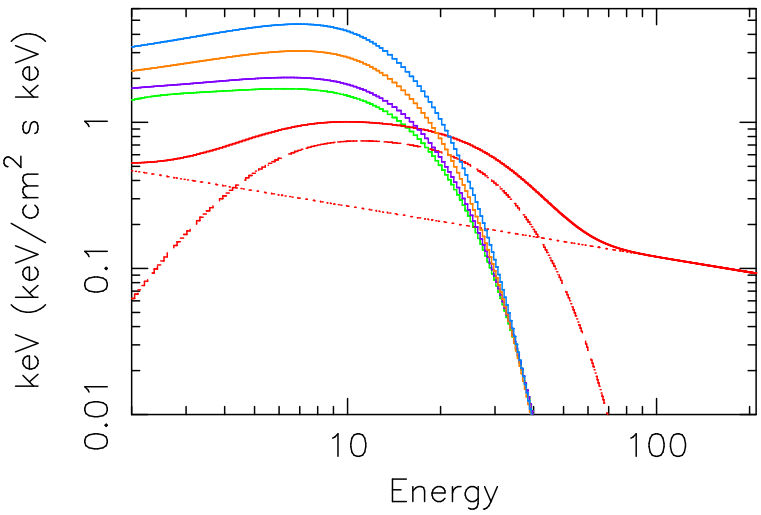

Figure 5.4: The unabsorbed best-fit models of the A–E data sets, see Table 5.1. The model for the green, purple, orange and blue spectra is thermal Comptonization, while a power law (dotted curve) is added in the red spectrum (C). Note that the power law dominates at low energies, and thus it is probably only a phenomelogical, but nonphysical, description of the spectrum.

ature of the seed blackbody photons upscattered in the Comptonizing plasma is unphysically high, $kT_0 \simeq 3.9$ keV. Data model and residual are showed in top left of Figure 5.5.

- In order to constrain the model to acceptable values of the blackbody temperatures, we used a model with kT_0 allowed to be ≤ 2 keV. Also, we have constrained $\Omega/2\pi \leq 1$. The resulting purely-thermal model provides a worse fit, χ^2_r(d.o.f.)$= 1.09(54)$, with $kT_e \simeq 24$ keV, $\tau \simeq 1.9$, $kT_{in} \simeq 1.4$ keV, similar to the parameters found in the atoll source 4U 1608–52 [67]. Data model and residual are showed in top right of Figure 5.5.

- To improve the fit of this model, in particular to account for the high-energy residuals (appearing as a high-energy tail), we have added nonthermal electrons to the thermal plasma, as it has been done to account for some spectra of both black-hole ([68]; [79]) and neutron-star binaries [66]. We have obtained χ^2_r(d.o.f.)$= 1.07(52)$ for a model with the nonthermal tail with the power-law index of $p \simeq 1$ above the electron Lorentz factor of 1.6 (and the Maxwellian dis-

tribution below it), and other parameters similar to that of the previous model. We stress, however, that this model is significantly more complex than the one with CompTT and a power law presented above. Data model and residual are showed in the bottom of Figure 5.5.

Table 5.2: Spectral fitting results for the JEM-X and IBIS broad-band spectra of 4U 1820–30. The model is CompTT for A, B, D, E, and a CompTT + a power law for C.

parameters	A (blue)	B (green)	C (red)	D (purple)	E (orange)
kT_0 (keV)[a]	0.2	0.4	1.5	0.3	0.2
kT_e (keV)	$2.71^{+0.08}_{-0.07}$	$3.12^{+0.10}_{-0.10}$	$6.10^{+0.77}_{-0.62}$	$2.90^{+0.20}_{-0.18}$	$2.83^{+0.07}_{-0.06}$
τ	$7.04^{+0.32}_{-0.29}$	$5.85^{+0.24}_{-0.23}$	$3.89^{+0.79}_{-0.65}$	$6.38^{+0.72}_{-0.62}$	$6.71^{+0.24}_{-0.22}$
$\mathrm{norm}_{\mathrm{CompTT}}$	$2.34^{+0.21}_{-0.19}$	$0.58^{+0.06}_{-0.06}$	$3.79^{+0.68}_{-0.59} \times 10^{-2}$	$1.06^{+0.21}_{-0.18}$	$1.57^{+0.12}_{-0.11}$
Γ	–	–	$2.35^{+0.10}_{-0.11}$	–	–
norm_{pl}	–	–	$0.60^{+0.22}_{-0.24}$	–	–
χ^2_r(d.o.f)	1.13(44)	0.96(46)	1.0(57)	1.07(37)	1.14(43)
$F_{4-20\mathrm{keV}}$[b]	9.1×10^{-9}	3.8×10^{-9}	2.1×10^{-9}	4.2×10^{-9}	5.8×10^{-9}
$F_{20-60\mathrm{keV}}$	3.3×10^{-10}	1.8×10^{-10}	7.4×10^{-10}	2.2×10^{-10}	2.5×10^{-10}
$F_{60-120\mathrm{keV}}$	–	–	1.5×10^{-10}	–	–

[a] Fixed parameters

[b] The Fluxes are in units of erg s^{-1} cm^{-2}

5.1.4 Discussion on the results

We got the first detection of hard emission above 50 keV in the island state of the atoll source 4U 1820-30 using IBIS data. Up to now, 4U 1820-30 has not been included in the sample of the high-energy emitting bursters [61] and indeed neither *BeppoSAX*, *CGRO*/BATSE nor *RXTE* detected this source above 50 keV ([63] and references therein). The previous lack of detection might have been due to either the source spending most of the time in the Soft state, the weakness of the emission above 50 keV in the island state, or the strong emission at $\geq$ 50 keV appearing in that state only occasionally.

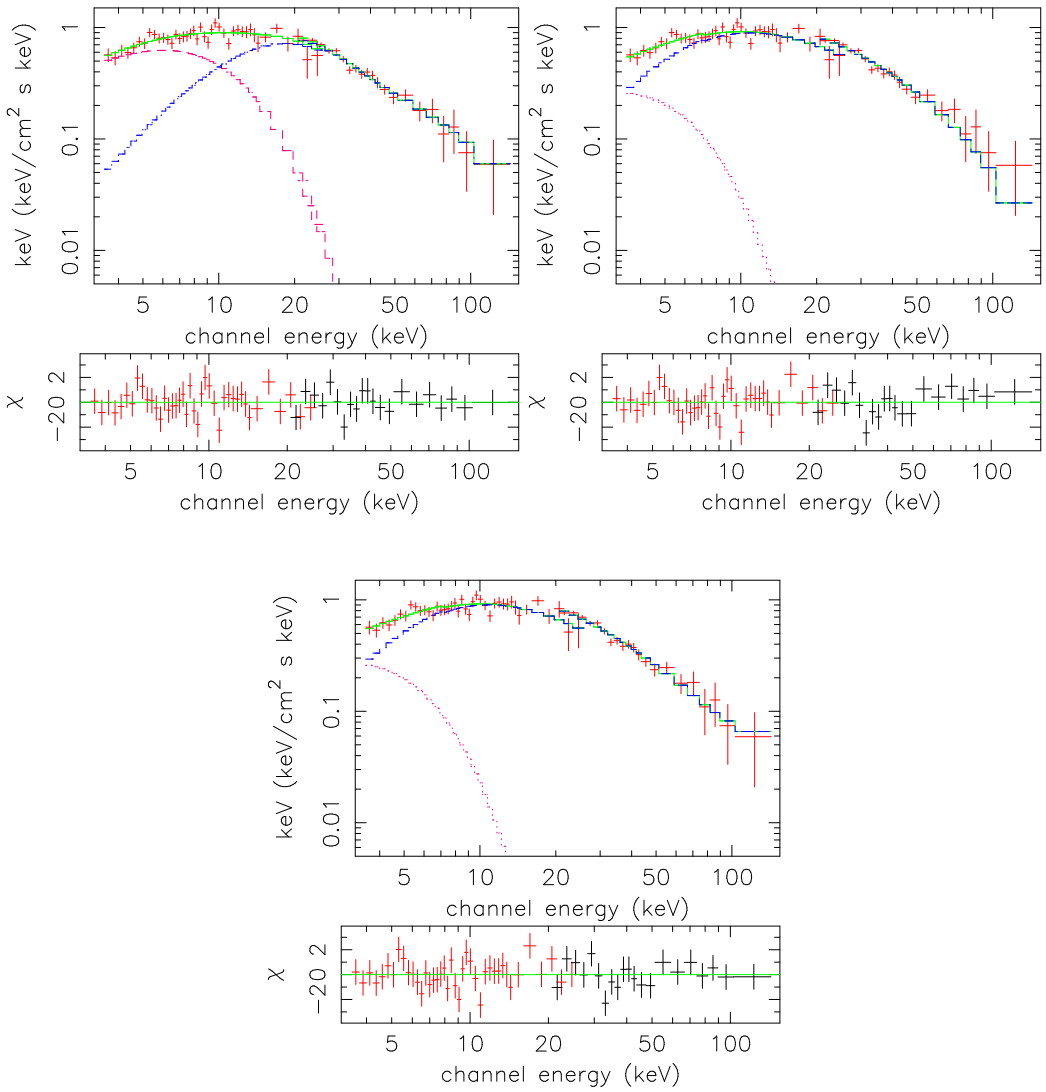

Figure 5.5: `CompPS` plus `diskbb` model for the Hard spectrum. See text for differences.

In our island-state observation, the relative flux contribution for energies > 60 keV is $\sim$10%. The ratio of the 4–20 keV flux to the 20–120 keV ones is $\sim$2, whereas it is in the range 20–27 for the Soft (banana) state. It is worthwhile to stress that our detection of emission above 50 keV is at the 1–20 keV luminosity of $\simeq 1.4 \times 10^{37} (d/5.8\,\mathrm{kpc})^2$ erg s^{-1}, i.e. close or somewhat below the critical value for which the X-ray binaries become hard emitters as proposed by Barret et al. (1996, 2000) [27], [28].

While the origin of the thermal Comptonization component in the Soft state ap-

pears well explained as emission from hot electrons that upscatter soft photons coming from the accretion disk and the neutron star surface, the origin of the high-energy tail is far to be clear.

The radio emission in the X-ray binaries is suggested to originate from jet-like outflows which may also produce X-rays [14]. In particular, there are indication that both black-hole candidate and neutron stars systems, when in Hard state, produce steady jet [37]. Also, in the Hard state, positive correlation between radio and X-ray fluxes has been reported [37]. 4U 1820-30 is one of the few radio detected atoll source. The only radio emission reported so far was during the Soft state [41], but it is probable that radio emission exist also in the Hard state, as e.g. for 4U 1728-34 [42].

Furthermore, the power-law tail detected by us is relatively soft, with $\Gamma \simeq 2.4$, and dominates over the Comptonization emission already for $E \leq 4$ keV, as shown in Figure 5.4.

If this component is due to nonthermal synchrotron emission, the minimum energy corresponds to the self-absorption turnover, typically in the IR or optical range, as it is the case in another ultracompact binary, 4U 0614+091 [37]. Then the hard tail luminosity would be $\sim$10 times that of X-rays (see also discussion in [87]), making the island state more luminous than the banana state, with the maximum of the overall EF_E at $\sim$1 eV, so far never reported in X-ray binaries.

The presence of the jets or outflow could be due also to magnetic reconnection events above the accretion disk [75].

A more likely origin of the power law tail appears to be emission of nonthermal electrons in a hybrid (i.e., containing also thermal electrons) plasma, as discussed in Section 5.1.3. Non thermal hard tails have been commonly detected in Soft states of black-hole binaries (e.g., Cyg X-1, [68]) and neutron-star Z-sources, e.g., GX 17+2 ([32]; [66]), Sco X-1 [33], GX 349+2 [35], GX 5–1 [60], while for atoll sources there are only few cases, e.g., 4U 0614+091 [34]. On the other hand, nonthermal tails have been detected in the Hard state of some black-hole binaries, e.g. Cyg X-1 [71] and GX 339–4 [79].

The 4U 1820-30 high-energy part of the spectrum (E $\geq$ 10 keV) can be well fitted with purely thermal Comptonization with $kT_{\rm e} \simeq 50$ keV, as discussed in Section 5.1.3.

This electron temperature is higher than the one seen in 4U 1608–522 [67], but the Comptonization temperature of atolls in the island state has not yet been established for a large sample of sources; also, $kT_e \simeq 50$ keV is a value very similar to that detected in the Hard state of black-hole binaries [84]. Finally, the problem with best fitting the spectrum at E $<$ 10 keV with this model may be due to the complexity of the X-ray spectra in the Hard state, including contributions from the disk, the corona above the disk, optically-thin and optically-thick parts of the boundary layer and the uncovered part of the neutron star surface.

A different thermal Comptonization model has been published by Markoff et al. (2005) [70]. They proposed thermal synchrotron self-Compton emission in a jet as a model for the Hard state of black hole binaries. However, their model requires an extremely high electron temperature, $kT_e \sim$ 3–4 MeV. This would result in the thermal spectral cutoff in black hole binaries at energies $\geq 3kT_e \sim 10$ MeV, which has not been seen in *any* object yet. Although we cannot formally rule out a contribution from this process, postulating the presence of $\sim$3 MeV plasma in 4U 1820–30 appears rather speculative at present stage.

In summary, we have discovered strong high-energy emission from 4U 1820–30 in Hard state. The high energy emission is harder than that from some other atolls in the island state. The most likely interpretation is either emission of some nonthermal electrons or thermal emission from plasma with a relatively high temperature, $kT_e \geq 50$ keV.

5.2 4U 1608–522

4U 1608–522 is an atoll type and transient source, with periodic outbursts [122], [126] during which the source changes spectral properties moving on the color-color diagram.

A reflection feature has been detected from this source [67]. 4U 1608–522 is one of the few atoll detected also in the radio bands [41], so that it is a good candidate for the presence of non thermal-emission. The scientific analysis of the monitoring with *INTEGRAL* aims to search for the spectral variations and characterise the high energy emission.

We study the source in the 4–200 keV energy range JEM-X [51] and IBIS [47]. We also analyse two non contemporaneous observations with *BeppoSAX* Satellite (LECS, MECS and PDS instruments) covering the 0.1-200 keV energy range [120].

5.2.1 *INTEGRAL* and *BeppoSAX* observations

The *INTEGRAL* observations part of this work, cover a non continuous period starting from 2004 February 18 to 2005 September 8, during the satellite revolution 164–354. We analysed all the public data of JEM-X (within $7^\circ \times 7^\circ$ of the FOV) and IBIS (within $9^\circ \times 9^\circ$ FOV) for a total of 192 and 420 pointings respectively.

The two public observations of *BeppoSAX* (available at http://asdc.asi.it) were performed on 1998 February 28 and 2000 August 1. The LECS (0.1-10 keV), MECS (1-10 keV) and PDS (15-200 keV) spectra have been generated within a radius of $4'$ and the public distribuited files for matrices, background subtraction and spectral binning have been applied; a 1 % systematic errors has been added to the model.

5.2.2 Light curves and hardness–intensity diagrams

In Figure 5.6 we report the public 1.5-12 keV *RXTE*/ASM light curves of 4U 1608-522 in the period 2004 February–2005 September with overplotted the light curves for JEM-X (4–10, 10–20 keV bands, light and dark green diamonds) and for IBIS (20–30, 30–60, 60–120 keV bands, red, purple and blue crosses). Each *INTEGRAL* point

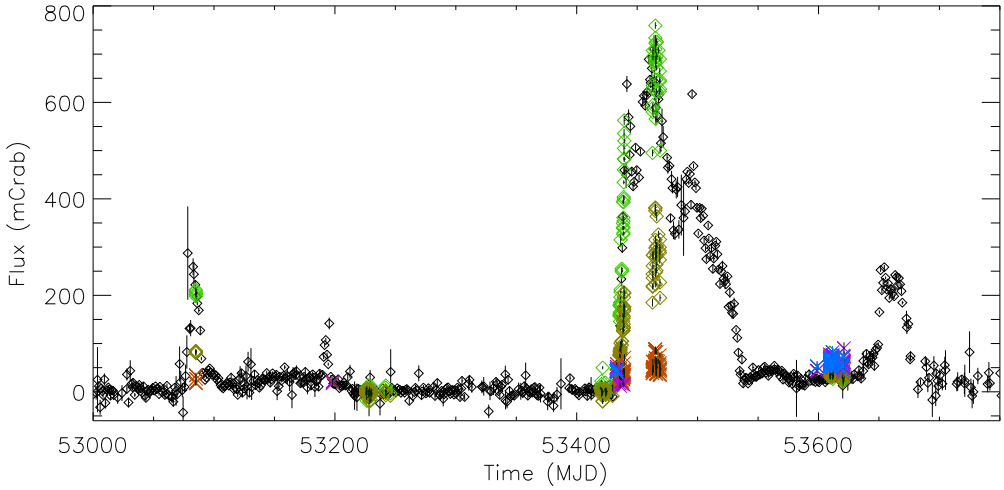

Figure 5.6: The 2004–2005 light curves of 4U 1608-522 with *RXTE*/ASM (black diamonds), *INTEGRAL*/JEM-X (light green diamonds in the 4-10 keV and in the dark green diamonds in the 10-20 keV band) and IBIS (red crosses in the 20-30 keV, purple in the 30-60 keV and blue in the 60-120 keV). Each point correspond to the count rate in mCrab unit, for a time bin of 1 ScWs for *INTEGRAL* and 1-day everage for ASM.

corresponds to a single ScW.

Figure 5.7 is the zoom of the light curve during the outburst of the source started on February 2005 (MJD 53400). Different colors in Figure 5.7 correspond to different spectral properties. The colors in the the hardness–intensity diagrams of Figure 5.8 have been used accordingly. The left panel in Figure 5.8 shows the hard color–intensity diagram from JEM-X/IBIS data. The hard color is defined as the ratio of the mCrab count rate of the 10–20 to 20–30 keV energy bands, while the Intensity are the sum of the mCrab count rate of the single energy bands. The right panel shows the same diagram supplemented with JEM-X data in the energy band 4–10 and 10–20 keV, represented by the grey points. The dark and light blue data correspond to a Hard spectral state (island state) while the purple red and green data correspond to Soft states (banana states). The Hard spectrum appear at the beginning and the end of the outburst (cfr Figure 5.7) as typical for transient sources.

In Figure 5.9 we show the ASM light curve where the two *BeppoSAX* observations are marked with vertical lines. In the 1998 observation the source was in a Soft state, while in 2000 one was in quiescent phase, as discussed below.

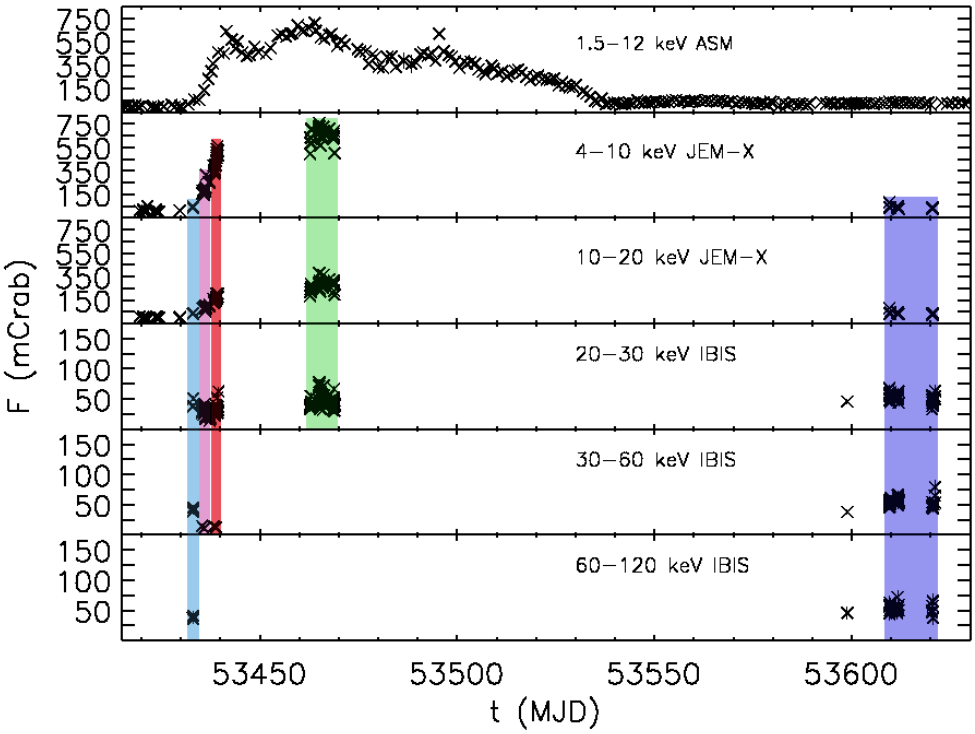

Figure 5.7: The zoom during the outburst of February–April 2005. The colored lines correspond to different spectral states. Note that the hardening appear just at the begin of the outburst and follow at the end of the outburst (check the blue crosses). These data are reported with the same colors in the Hardness-Intensity diagrams of Figure 5.8.

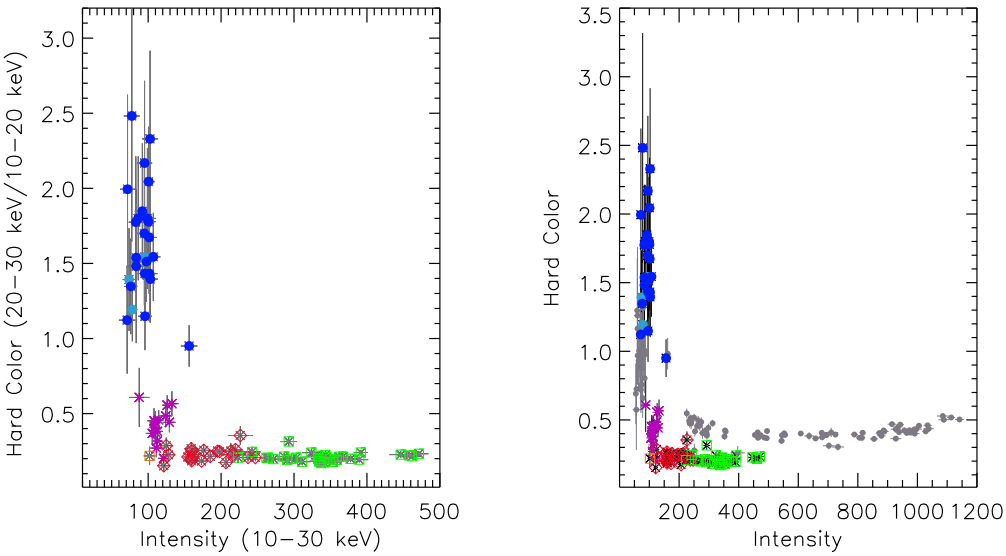

Figure 5.8: Hard color–Intensity diagram with IBIS/JEM-X data (left), and JEM-X/JEM-X data (right); each point corresponds to a 1 ScW.

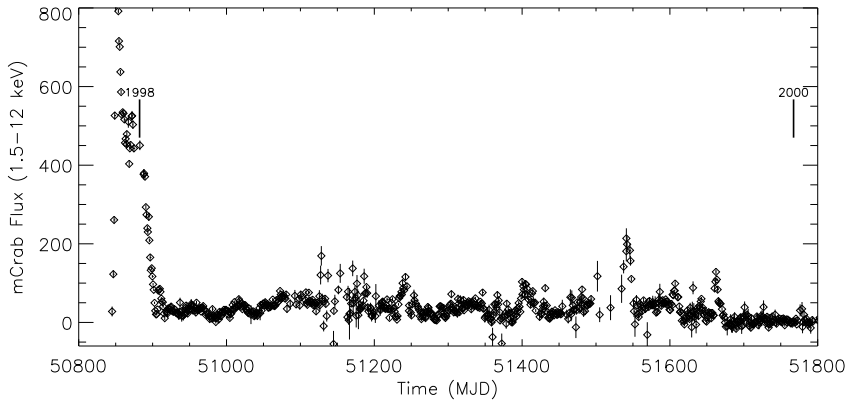

Figure 5.9: ASM 1.5-12 keV light curve, in which are indicated with vertical lines, the moment of *BeppoSAX* observations.

5.2.3 Spectral analysis

Spectra for *INTEGRAL* have been derived using data point collected accordingly to the same areas in the hardness–intensity diagram (see Figure 5.8). In Table 5.3 the log of the *INTEGRAL* and *BeppoSAX* data sets and spectral states are reported. Data S1 and S5 correspond to Hard state and S3 S4 correspond to Soft state and S2 to the Soft/Intermediate state.

Table 5.3: The log of the data used for spectral fitting of 4U 1608–522. The colors are used in the light curves, Figure 5.2, and hardness–intensity plots, Figure 5.8.

Data set	Time start (MJD)	Instruments Exposure (ks)	Spectral state
INTEGRAL		IBIS ; JEM-X	
S1 (light blue)	53433.0	10.2 ; 10.7	hard
S2 (purple)	53435.2	56.5 ; 32.0	soft/intermediate
S3 (red)	53438.0	64.5 ; 36.7	soft
S4 (green)	53462.7	74.6 ; 63.5	soft
S5 (blue)	53598.8	45.6 ; 53.7	hard
BeppoSAX		LECS ; MECS; PDS	
Spe1998	50872	30.4 ; 13.2 ; 14.1	soft
Spe2000	51757	47.8 ; 23.3 ; 22.7	quiescence

Soft states

For the S2, S3 and S4 data sets we first try to model the spectra with a Comptonised component, `CompTT` [57]. For the spectra corresponding to S2 and S3 and to minor extent for S4, it was necessary to add a soft component because of a soft excess below 6 keV and the worst value of the χ^2_r (1.4 and 1.2 respectively). A multicolor disk black body component, `diskbb` [16] is used, though a black body component (`bb`) gives similar results. In Table 5.4 we reported the parameters of the `CompTT+diskbb` model for these spectral states.

The fits results show that the inner disk black body temperature ($kT_{\rm in}$) rise from the left banana to the right banana (S2 to S4), while there is a corresponding decreasing of the temperature of the Comptonised region ($kT_{\rm e}$) which becomes more optically thick (τ increases).

Table 5.4: Spectral fitting results for the spectra of the banana states with *INTEGRAL* and *BeppoSAX*.

	INTEGRAL			*BeppoSAX*
	S2	S3	S4	spe 1998
parameters	CompTT+diskbb			
kT_0 (keV)	1.08	1.07	1.01	$0.78^{+0.02}_{-0.02}$
$kT_{\rm e}$ (keV)	$5.77^{+0.96}_{-0.32}$	$3.36^{+0.21}_{-0.17}$	$2.98^{+0.10}_{-0.10}$	$2.41^{+0.02}_{-0.03}$
τ	$2.29^{+0.32}_{-0.35}$	$3.59^{+0.31}_{-0.29}$	$4.27^{+0.21}_{-0.16}$	$6.46^{+0.13}_{-0.05}$
$\mathrm{norm}_{\rm CompTT}$	$0.11^{+0.02}_{-0.02}$	$0.56^{+0.07}_{-0.07}$	$1.22^{+0.02}_{-0.16}$	$1.09^{+0.02}_{-0.03}$
kT_{in} (keV)	$0.51^{+0.18}_{-0.13}$	$0.56^{+0.29}_{-0.09}$	$0.60^{+0.98}_{-0.26}$	$0.64^{+0.01}_{-0.02}$
$\chi^2_r(\nu)$	0.99(36)	0.97(33)	0.99(33)	1.35(403)
	reflect*gauss+CompTT+diskbb			
kT_0 (keV)	1.24	1.12	1.06	$0.65^{+0.02}_{-0.03}$
$kT_{\rm e}$ (keV)	$6.96^{+1.87}_{-1.19}$	$3.44^{+0.13}_{-0.28}$	$3.00^{+0.09}_{-0.08}$	$2.57^{+0.01}_{-0.10}$
τ	$1.69^{+0.46}_{-0.47}$	$3.42^{+0.36}_{-0.31}$	$4.10^{+0.20}_{-0.17}$	$5.74^{+0.08}_{-0.13}$
$\mathrm{norm}_{\rm CompTT}$	$0.08^{+0.02}_{-0.02}$	$0.51^{+0.06}_{-0.07}$	$1.14^{+0.10}_{-0.09}$	$1.22^{+0.03}_{-0.09}$
kT_{in} (keV)	$0.69^{+0.14}_{-0.11}$	$0.61^{+0.20}_{-0.14}$	$0.55^{+0.76}_{-0.05}$	$0.46^{+0.08}_{-0.23}$
$\Omega/2\pi$	$0.37^{+1.26}_{-0.64}$	$0.18^{+0.61}_{-0.40}$	$0.34^{+0.40}_{-0.23}$	$0.46^{+0.08}_{-0.23}$
σ_{Fe} (keV)	–	–	–	$1.22^{+0.18}_{-0.49}$
EW (eV)	–	–	–	208
$\chi^2_r(\nu)$	0.94(35)	1.01(32)	0.99(32)	1.15(401)

Moreover, for the spectrum S2 and S3 it is evident that the temperature of the input photons required for the Comptonization, kT_0, has a different value from the inner disk temperature of the photons, $kT_{\rm in}$. This fact indicates that the seed input photons should come from a region that doesn't have the same temperature of the inner disk region, such as boundary layer or from the neutron star surface. On the contrary, for S4 the temperature of the inner disk is compatible with the kT_0 value. If we try, during the fitting procedure, to fix, for all the spectral data, the parameters kT_0 and $kT_{\rm in}$ at the same value, only the spectrum S4 gives an acceptable χ^2_r value. On the other hand, we are aware that this parameter are well out of the instrument energy coverage.

We analysed also the Soft state as observed in 1998 by *BeppoSAX*, which also covered energies below 4 keV (below JEM-X operative range) and permits a better evaluation of the soft parameters. The results of the fit with the addition of an absorption model with a column density $N_{\rm H}$ of 1.2×10^{22} cm^{-2} is reported in Table 5.4. In this occasion also the source has a temperature of the input photons higher than the temperature of the inner disks photons temperature.

A reflection component [79] was also added, but a better fit resulted only for S2 spectrum, while the F-test didn't show any improvement for S3 and S4. This could be due to the soft-intermediate state nature of the S2 spectrum, as we expected from the light curve. In fact this spectrum appears after a Hard state and during the rise of the outbursts of the source. This reflection component contributes to the fit with a sort of bump in the 10-20 keV band and as results there is also a better fit of the high energy data ($>$ 30 keV). The best fit parameters value doesn't really change from the previous fit; results are shown in Table 5.4 and the energy spectra as well as models are showed in Figure 5.10. For the BeppoSAX data we need to add also a gaussian model to fit an excess below 10 keV, and it is showed in Figure 5.11 compared to the quiescent spectrum. A Fe emission line at energy of 6.4 keV with a large FWHM is required to best model the emission.

Assuming the source distance at 3.6 kpc [123] the value of the unabsorbed bolometric luminosity of these spectra ranges from 6×10^{37} erg s^{-1} to 1.5×10^{37} erg s^{-1} from the Soft to the Intermediate state respectively.

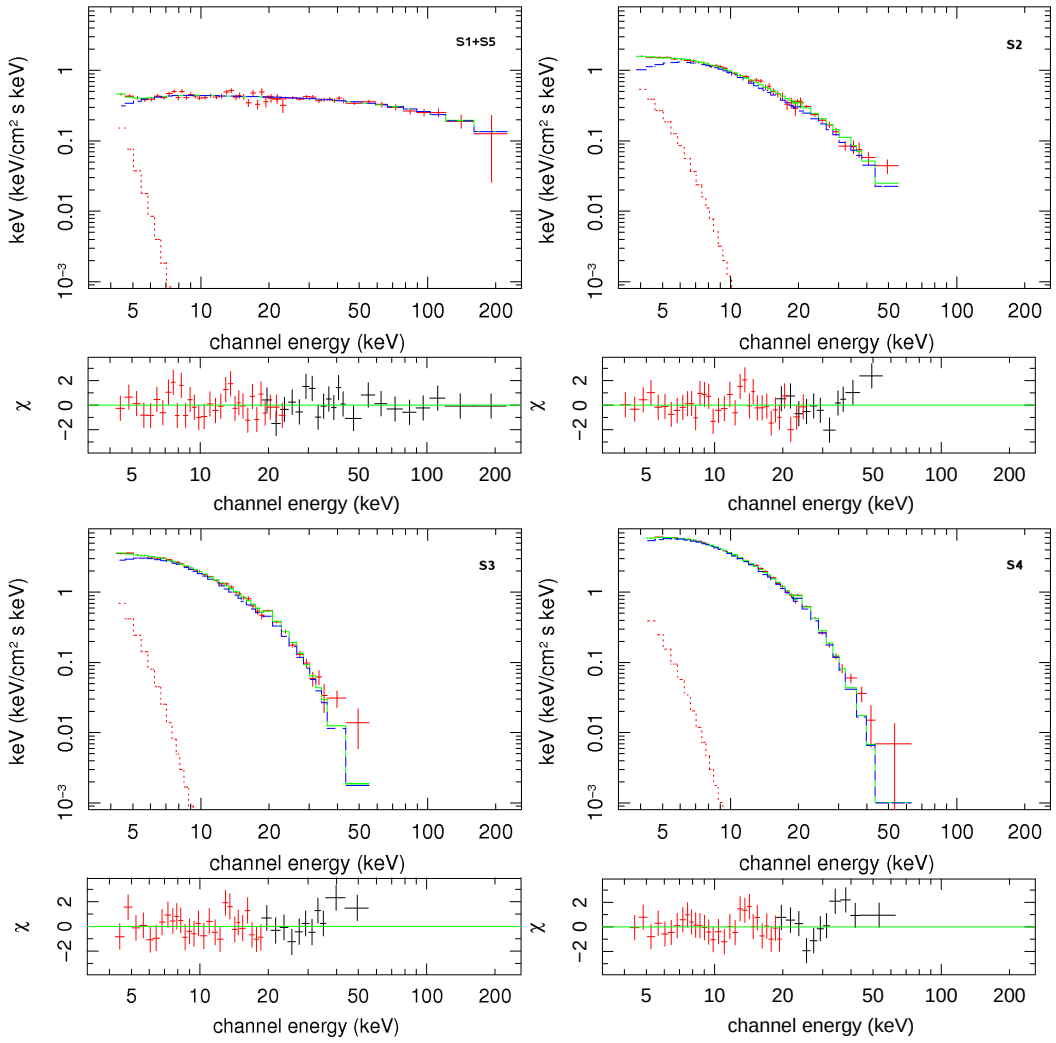

Figure 5.10: *INTEGRAL* spectra of 4U 1608-522 during the 2005 outburst. From the top left to the bottom right: Hard (S1+S5 data sets) and Soft spectra (S2, S3, S4 data sets) with IBIS and JEM-X, with the CompTT+diskbb+reflect models.

Hard states

Hard state have been detected at the beginning and at the end of the 2005 outburst (see Figure 5.7). The light curve shows same behaviour and values, so the S1 and S5 data sets have been used to get a single spectrum to increase the signal to noise ratio.

Firstly, a Comptonization model, `CompTT` has been used to fit the data resulting

in a kT_e=57.4$^{+54.3}_{-21.3}$, an optical depth, τ=0.49$^{+0.41}_{-0.31}$, and an input photons temperature, T_0, of 0.5 keV, with a $\chi^2_r(\nu)$= 0.91(50). A `diskbb` component has been add to take into account the higher residual below 6 keV. Table 5.5 reports the obtained values of this fit, and Figure 5.10 shows the spectrum extending up to 200 keV. Moreover, we obtain an acceptable fit also freezing the temperature of the seed photons to the black body temperature. In this case we obtain a soft temperature of 0.5 keV, and the corona temperature and optical depth are similar to the previous model.

It is evident in all cases that the value of the temperature of the electrons of the corona is not well costrained, as indication that we don't detect a real cut–off in this spectrum. We also checked the SPI data along the same period which show agreement with our ones [E. Jouradain, private comunication].

Finally we try to fit this spectrum with the `CompPS` model [58], which include the reflection parameter. The results are compatible with the `CompTT` spectrum model and are showed in Table 5.5.

The bolometric luminosity of the Hard spectrum correspond to 5×10^{37} erg s^{-1}.

Table 5.5: Spectral fitting results for the spectrum of the island state (S1+S5 data sets) with JEM-X and IBIS.

Parameters	CompTT+diskbb	CompPS+diskbb
kT_0 (keV)[a]	1.19	1.05±0.46
kT_e (keV)	62.63$^{+46.01}_{-28.81}$	38.48±9.7
τ	0.44$^{+0.57}_{-0.33}$	2.59±0.79
$\Omega/2\pi$	–	0.05±0.24
norm	0.003$^{+0.002}_{-0.002}$	74.52±138.28
kT_{in} (keV)	0.42$^{+0.31}_{-0.04}$	0.50±0.60
$\chi^2_r(\nu)$	0.79(49)	1.17(47)

[a]Fixed parameter

Quiescent state

During *BeppoSAX* observation in 2000, we detected the source in a quiescence state as derived with LECS and MECS only (0.1-10 keV), at a bolometric luminosity of about 1.4 $\times10^{33}$ erg s^{-1}.

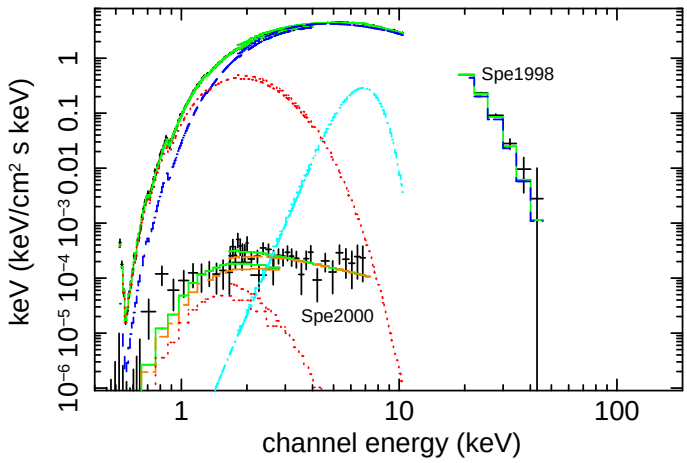

Figure 5.11: *BeppoSAX* soft and quiescent spectra of 4U 1608–522. Spe1998: Soft spectrum with CompTT+diskbb+reflect+gaussian model. Spe2000: quiescent spectrum modelled by NSA plus power law models.

This quiescent state was fitted with different models: a simple power law, a black body, a black body plus a power law, a Neutron Star Atmosphere model (NSA of XSPEC) [128], and finally a NSA plus power law. For all the fits we assumed an absorbtion, $N_{\rm H}$, fixed to 1.2×10^{22} cm^{-2}.

The single power law component gives a photon index of 3.3 with a good $\chi^2_r(\nu)$ value of 0.82(65).

The black body model gives a temperatures 0.5 keV, with $\chi^2_r(\nu)$equal to 1.18(65). From the value of the blackbody normalization (assuming a distance of 3.6 kpc) we derive the black body emission region as $\sim$0.4 km which is incompatible with the typical neutron star radius of 10 km. This could be explained assuming that the X-ray emission originates from a small emission region such as the polar caps of the neutron star. Adding a power law component the fit improves [$\chi^2_r(\nu)$=0.74(63)] and the black body temperature is 0.07 keV, but the black body region emission is too large respect to the neutron star radius ($\sim$ 100 km).

We also try to fit the quiescence spectra with a pure H-atmosphere spectrum instead of a black body emission. The Neutron Star Atmosphere model uses as parameters the mass and radius of the neutron star, the unreshifted effective temperature of the surface of the neutron star, $kT_{\rm eff}$, and the normalization that is equal to $1/D^2$ where D

is the distance of the source [128]. Note that the black body model temperature (i.e. the temperature at infinite distance) is different from the $kT_{\rm eff}$ by the redshift factor corresponding to 0.76, for the standard values of mass and radius of a NS ($1.4M_{\odot}$ and 10 km). We freeze the mass and the radius of the star at this standard values and the normalization to the value of 7.716×10^{-8} (for D equal to 3.6 kpc), and we left as free parameter the effective temperature. By freezing the NS radius at 10 km, we overcome the problem of the underestime of the emission region derived from the black body model. The effective temperature of the neutron star obtained is 0.17 keV, but the value of the $\chi^2_r(\nu)$ is still too high [1.7(66)].

The best fit model has been obtained adding a power law to the NSA component: in this case the effective temperature corresponds to 0.12 keV, and the photon index of the power law to 3 [$\chi^2_r(\nu)$ is equal to 0.83(64)].

In the past decade the quiescent spectrum of this source was modelled with the same models (black body, single power law or NSA models) though a power law component was never required to the fits [119], [124].

5.2.4 Discussion and conclusions

We reported the study of the spectral characteristics of the atoll source 4U 1608–522 in different spectral states [106]. It shows the bolometric luminosity ranging from 1.4 $\times10^{33}$ erg s^{-1} to 6 $\times10^{37}$ erg s^{-1} in the quiescent up to the Soft state. We fit the Soft and Hard spectra with a soft component plus a Comptonization component. In all the spectra (except for the quiescent spectrum) there is also the hint of a reflection emission from the disk.

The soft component is well described by a disk black body model emission with a inner temperature ranging from 0.4 to 0.7 keV;the Comptonised corona temperature increases from the Soft to the Hard state (i.e. from the banana to the island branch), and the optical depth decrease, becoming an optically thin and very hot corona in the Hard state; the energy spectrum doesn't show any energy cut–off. The seed input photons have a higher temperature than the inner disk temperature (T_0 ranging from 0.6 to 1.2 keV), indicating that could come from a different region such as a boundary layer or

the neutron star surface.

From the diskbb normalization model we estimate the radius of the black body emission region, i.e. the inner disk radius (see section 4.0.8). For the Soft spectra we obtain a radius ranging from 20 to 60 km while for the Hard spectrum it extends up to 120 km, as expected to allow the formation of hot plasma corona.

We investigate also the spectrum of the quiescent state of 4U 1608–522. For the first time the addition of a power law component to the NSA model is required as reported from other sources (e.g. Aql X-1, Cen X-4 [119], [121], [125]). The nature of the quiescent tail is still unclear, but it could be due to a sort of comptonization due to the low-level accretion rate also in the quiescence state.

5.3 4U 1728–34 alias GX 354–0

The source 4U 1728–34 is a well known LMXB classified as atoll type based on its track described in a color-color diagram and its timing and spectral properties on the different branches of this track [93]. This system contains a Neutron Star as indicated by the presence of type-I X-ray bursts. The Eddington-limited bursts allowed for the distance estimate of 4.4-5.1 kpc [32]. The time averaged persistent Soft (0.1 keV) to Hard (300 keV) X-ray spectrum of 4U 1728–34 was studied using different satellites (from Einstein to *BeppoSAX*, *RXTE* and finally *INTEGRAL*). The spectrum was well described by a Comptonized spectrum plus a black body emission, with different parameters depending on the posistion in the CCD.

4U 1728–34 is one of the few atoll source also detected in the radio band, such us 4U 1820–30 (discussed in section 5.1) [41].

5.3.1 The *INTEGRAL* and *RXTE* observation campaign of 4U 1728–34

To study the spectral properties of 4U 1728–34, we planned a campaign consisting of approved AO11 *RXTE* and AO4 *INTEGRAL* observations. The *RXTE* monitoring is based on 2ks pointings every two days, from 2006 March to 2007 June. The *INTE-*

GRAL monitoring consisted on two parts: the first part (March-April 2006) with public GCDE observations and the second with observations guaranteed by the AO4 program (2006 September-October and 2007 February-April), for a total of 594 pointings.

5.3.2 Light curves

We monitored the source with *INTEGRAL* and *RXTE* during the period March 2006-March 2007. We extracted the IBIS light curves in the 20-40, 40-100, 100-300 keV energy bands and the PCA light curves have been extracted in the band 3-20 keV. Figure 5.12 (top) shows the light curve of the total observing period, in the 20-40 and 3-20 keV energy bands; in the bottom panel we show the hardness corresponding to the flux ratio 20-40/3-20 keV. In the total light curve one can see three main periods of *INTEGRAL RXTE* contemporaneous observations during which the source showed high energy emission, as well a changes in the hardness value. We show zoomed-in figure of the second period in bottom of Figure 5.12.

Figure 5.13 shows the IBIS light curves for the three different energy bands, and in the top panel, it is shown the 2-12 keV ASM rate. Note that, for each period, the source shows at high energy the same slow-rise then fall shape; moreover the flux increases first at high energies ($>$20 keV), with the increase at low energies coming afterwards. This behaviour indicates a spectral change of the source, as confirmed by the track of the source through the PCA hardness-intensity diagram of Figure 5.14, for each period.

5.3.3 Hardness-intensity diagram

Figure 5.14 shows the hardness-intensity diagram for PCA data. The hardness is defined as the flux ratio of the (6-10 keV)/(3-6 keV) energy bands and the Intensity is the rate in the 3-20 keV band. We show with different color the data of the three periods: red points for the 1st period, blue points for the 2nd period, green for the 3rd period. The black points are PCA data, without *INTEGRAL* coverage. In each period the source moved from the banana to the island state, showing the same behaviour. The points labeled A to E indicate the intervals in which we have simultaneous data

from *RXTE* and *INTEGRAL* and that have been used for spectral analysis.

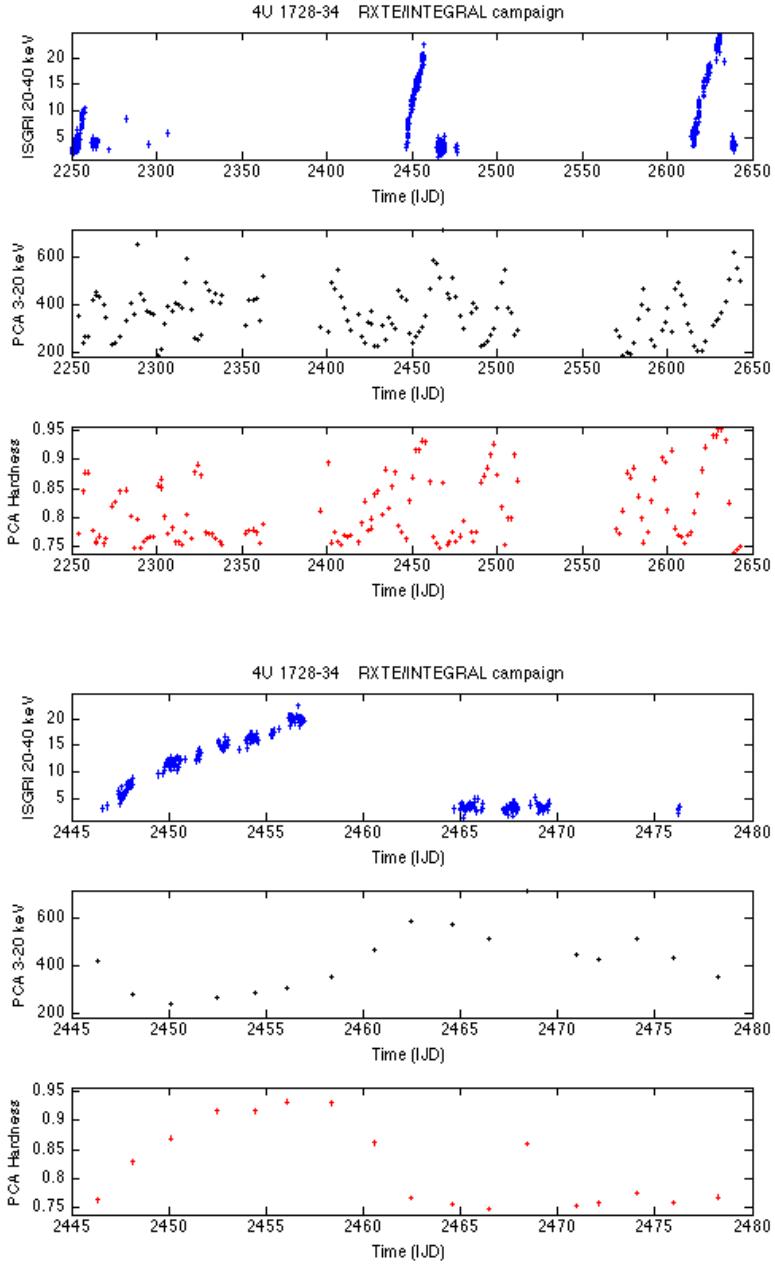

Figure 5.12: *Top: INTEGRAL* /IBIS and *RXTE*/PCA 2006-2007 light curves of 4U 1728–34. Three main period of observation are visible. Hardness is shown in the bottom panel. *Bottom:* Zoomed-in light curve during the second period. The spectral evolution of the source is clearly evidences

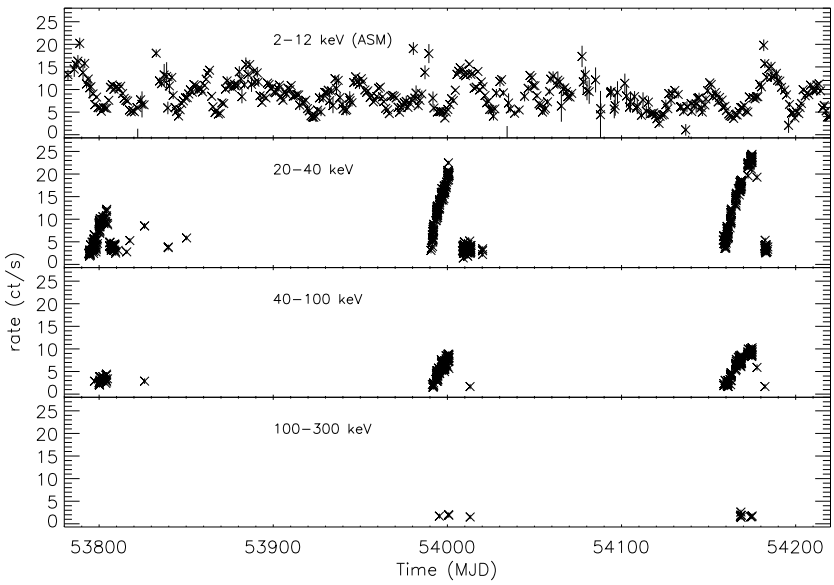

Figure 5.13: *INTEGRAL* /IBIS and *RXTE*/ASM 2006-2007 light curves of 4U 1728-34. The energy bands are indicated for each panel.

In Figure 5.15, we show the ASM and IBIS light curve, for the second period, with indicated A-E data sets. The A, B, C, D data sets correspond to the rise of the high energy emission, before the increase of the flux at low energies, whereas the E data correspond to high level of the flux at low energies.

5.3.4 Spectral analysis

We analysed the spectra of the A-E data sets of the *INTEGRAL*/IBIS and *RXTE*/PCA and HEXTE contemporaneous observations as shown in the hardness-intensity diagrams and light curves of Figure 5.14 and 5.15. In Table 5.6 we perort the IBIS observation log.

We tried to fit the spectra with different spectral models: Comptonization, Comptonization plus a disk black body and also reflection. For all spectra we need to add a Gaussian model to fit a broad line (σ_{Fe} $\sim$0.3-0.7) at about 6.4 keV, as previously observed. We fixed the interstellar column density at the value of $N_H = 2.3 \times 10^{22} cm^{-2}$.

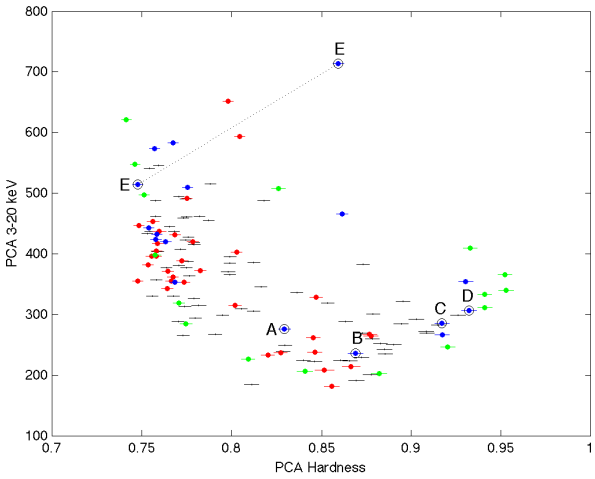

Figure 5.14: Hardness-Intensity diagram of 4U 1728–34 with PCA data. The hardness is the ratio (6-10 keV)/(3-6 keV). Different colors are used for the different observing periods as shown in Figure 5.12. The source covers the atoll track moving from the banana to the island state.

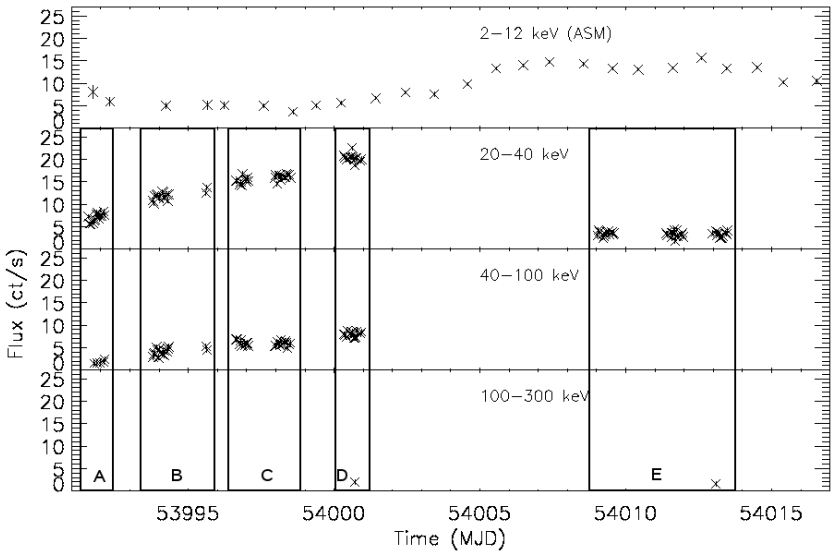

Figure 5.15: IBIS/*INTEGRAL* and ASM/*RXTE* light curves of 4U 1728–34, of the second period. Each box shows the IBIS pointings summed into the same average spectrum.

Table 5.6: The log of the *INTEGRAL*/IBIS data used for spectral fitting of 4U 1728–34.

Data set	Time start (MJD)	Exposure (ks)	Spectral state
A	53991.6	24.2	hard/intermediate
B	53993.8	27.1	hard
C	53996.6	39.2	hard
D	54000.3	24.3	hard
E	54009.0	67.6	soft

Soft state

The spectrum E has been well fitted by a Comptonization model, `CompTT` [57], plus a disk black body model, `diskbb` [16], as reported in Table 5.7. Spectrum with data, models and residuals are showed in Figure 5.16. The unabsorbed bolometric flux of the Soft state is 1.3×10^{-8} erg cm^{-2} s^{-1} that corresponds to a luminosity of 3.3×10^{37} erg s^{-1}, assuming a distance source 4.6 kpc.

Hard states

For the Hard states two degenerate fits with different models has been found:

1) DISKBB+COMPTT+PL models:

First, we fitted the spectra A-D by a `CompTT` plus a `diskbb` model. Because of the high value of χ^2_r and the high energy residuals (from IBIS and HEXTE) at E>50 keV (see Figure 5.17 and Table 5.7), we need to add a power law component. The need for the additional power law increases with the hardening of the spectrum, from A to D. Only for the A spectral data set, the addition of a soft black body component improves the fit; while for the B, C, and D spectra the fit doesn't improve (nevertheless the blackbody temperature values about 0.4-0.5 keV). The energy spectra of the lowest and strongest ones (A and D) are reported in the Figure 5.16. The fitting parameters are showed in Table 5.7.

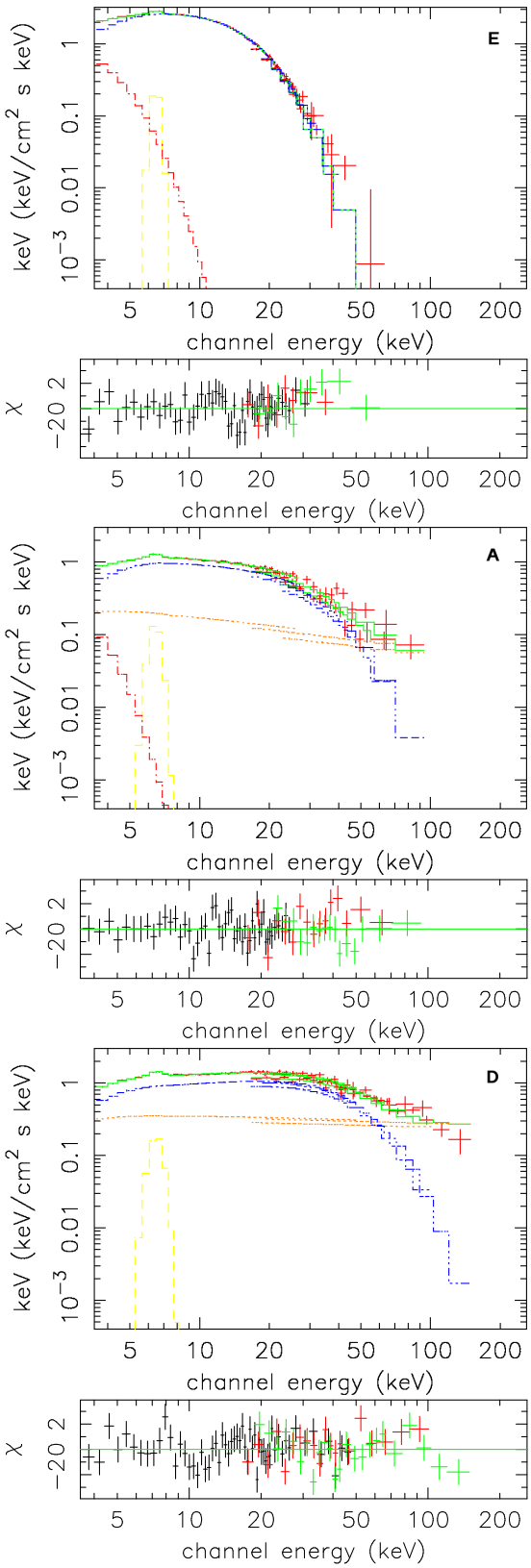

Figure 5.16: *INTEGRAL* /IBIS and *RXTE*/PCA and HEXTE spectra of 4U 1728–34 (E, A, D data set from top to bottom) with models described in Table 5.7.

Table 5.7: Spectral fitting results for the spectra of 4U 1728-34 with contemporaneous *INTEGRAL* and *RXTE* observations

	A	B	C	D	E
parameters	CompTT+diskbb				
kT_0 (keV)	$1.04^{+0.25}_{-0.07}$	$0.95^{+0.18}_{-0.05}$	1.02 ± 0.30	0.88 ± 0.27	$0.94^{+0.97}_{-0.06}$
kT_e (keV)	$7.87^{+0.28}_{-0.46}$	$10.84^{+0.62}_{-0.53}$	11.80 ± 0.26	11.70 ± 0.19	$2.89^{+0.03}_{-0.03}$
τ	$2.72^{+0.14}_{-0.16}$	$2.46^{+0.11}_{-0.12}$	2.61 ± 0.06	2.61 ± 0.04	$6.26^{+0.08}_{-0.15}$
$\text{norm}_{\text{CompTT}}$	$7.08^{+0.53}_{-0.23}\times10^{-2}$	$4.28^{+0.36}_{-0.37}\times10^{-2}$	$4.13\pm1.0\times10^{-2}$	$5.69\pm0.18\times10^{-2}$	$0.44^{+0.05}_{-0.22}$
kT_{in} (keV)	$0.45^{+0.25}_{-0.07}$	$0.46^{+0.40}_{-0.06}$	0.77 ± 0.40	0.41 ± 0.04	$0.59^{+0.51}_{-0.16}$
$\text{norm}_{\text{diskbb}}$	$8593.0^{+246103.0}_{-8147.2}$	$1000.5^{+167382}_{-5142.4}$	160.6 ± 338.1	3764.44 ± 2169.73	$2398.1^{+30604.9}_{-2172.0}$
$\chi^2_r(\nu)$	1.23(73)	1.21(92)	2.25(96)	2.46(93)	1.09(62)
parameters	CompTT+diskbb+PL				
kT_0 (keV)	$1.07^{+0.07}_{-0.06}$	$1.01^{+0.14}_{-0.12}$	$0.98^{+0.10}_{-0.11}$	$0.90^{+0.12}_{-0.09}$	–
kT_e (keV)	$6.66^{+0.63}_{-0.53}$	$7.77^{+0.61}_{-0.56}$	$9.01^{+0.45}_{-0.40}$	$8.75^{+0.40}_{-0.49}$	–
τ	$3.14^{+0.22}_{-0.22}$	$3.38^{+0.32}_{-0.32}$	$3.45^{+0.21}_{-0.24}$	$3.42^{+0.30}_{-0.27}$	–
$\text{norm}_{\text{CompTT}}$	$6.48^{+1.29}_{-0.78}\times10^{-2}$	$3.55^{+1.43}_{-0.85}\times10^{-2}$	$3.44^{+0.75}_{-0.46}\times10^{-2}$	$5.01^{+1.31}_{-1.04}\times10^{-2}$	–
kT_{in} (keV)	$0.46^{+0.20}_{-0.10}$	–	–	–	–
$\text{norm}_{\text{diskbb}}$	$5660^{+687452..0}_{-4600.47}$	–	–	–	–
Γ	$2.34^{+0.23}_{-0.35}$	$2.30^{+0.11}_{-0.26}$	$2.23^{+0.60}_{-0.95}$	$2.05^{+0.12}_{-0.30}$	–
norm_{PL}	$0.35^{+1.60}_{-0.27}$	$0.65^{+0.30}_{-0.37}$	$0.67^{+0.24}_{-0.17}$	$0.40^{+0.30}_{-0.30}$	–
$\chi^2_r(\nu)$	1.15(71)	0.69(93)	1.44(96)	1.24(93)	–

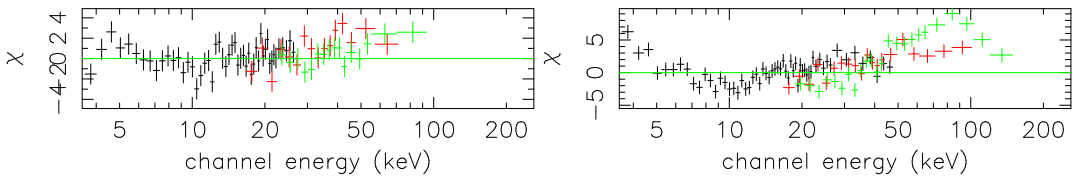

Figure 5.17: Residual to the models of the A and D data set, without the power law component.

We obtain also a good fit for the B, C, D set with the comptonization model `CompPS` assuming an hybrid thermal and non-thermal composition of the electrons plasma, as for the source 4U 1820-30 (see section 5.1.3). The results is a Comptonizing plasma with $kT_e \simeq 25$ keV, $\tau \simeq 3$ and input seed photons with $kT_0 \simeq 1.4$ keV; a reflection factor of 1; a inner disk temperature of 1 keV; and the high energy tail with index $p \simeq 4$ above the electron Lorentz factor of 1.7. We show the energy spectra with these models for the most Hard spectrum (D) in Figure 5.18.

2) DISKBB+COMPTT+REFLECTION models:

Only for the B, C, and D hard spectra (i.e. the state which present more high energy

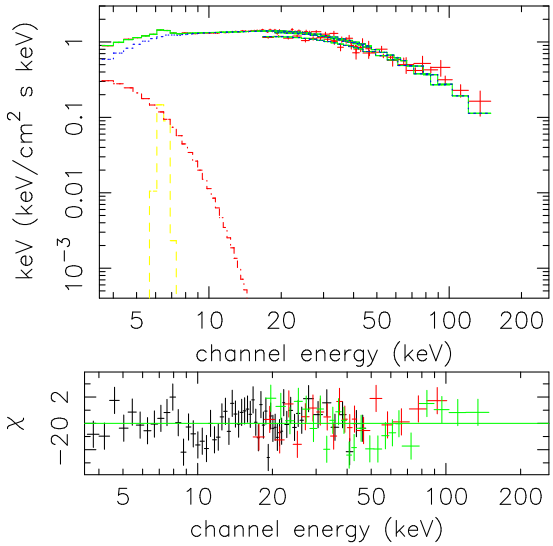

Figure 5.18: Spectrum of the D data set and residual to the model, with CompPS model assuming a hybrid thermal and non-thermal electron distribution. See text for the fit parameters.

residual without the power law component) it is possible to fit the data with a reflection component added to the Comptonization and diskbb components. In this case the Comptonization component reveals input seed photons with temperature of 1.1 keV; a corona with a higher electron temperature, ranging from 24 to 32 keV, a lower optical depth of 0.5-1, with respect to the models 1). The black body temperature is 0.5-0.6 keV and the reflection parameter has a high value of 1.1-1.7, that fit the bump near 20-30 keV. We show the energy spectra with these alternative models, of the most Hard spectrum (D) in Figure 5.19. Also this model gives acctetable values of $\chi^2_r(\nu)$ [0.68(93) for B; 1.50(95) for C; 1.22(92) for D].

The unabsorbed bolometric flux of the A and D spectrum is 2.9 $\times 10^{-8}$ erg cm^{-2} s^{-1} and 1.1 $\times 10^{-8}$ erg cm^{-2} s^{-1} corresponding to a bolometric luminosity of 7.3×10^{37} erg s^{-1} and 2.8×10^{37} erg s^{-1}.

5.3.5 Discussion and conclusions

The contemporaneous *RXTE* and *INTEGRAL* observations allow us to study over a broad energy band (3-200 keV) the different spectral states shown by the atoll source

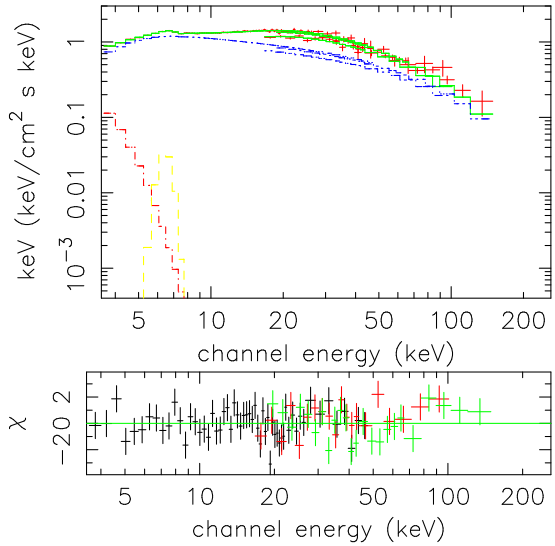

Figure 5.19: Spectrum of the D data set and residual to the models with Comptonization, gaussian, diskbb and reflection component. See text for the fit parameters.

4U 1728-34 [130]. The presence of different states are indicated by the position of the data points in the Hardness-Intensity diagram, as well by the *INTEGRAL* high energy behaviour of the source.

The Soft spectrum is well fitted by a soft component described by a disk black body emission with inner temperature of 0.6 keV, and by a hard component described by a Comptonizing corona with a low electrons temparature of 3 keV and high optical depth of 6.

The Hard spectra are described by two different models, with different physical characteristics. The first one is rapresented by a Comptonization with a low temperature of the electrons (6-10 keV) and optical depth of 3, plus a power law with photon index of about 2. The second one is a Comptonization model with a higher temperature of the electron plasma (20-30 keV), with the addition of high reflection component, due to repeated inverse Compton scattering of the seed photons by the hot electron of the corona.

Although, the two models well represent the data, we discard the ”reflection” model, 2), because of the high reflection amplitude that imply a decreasing of the inner disc radius, not in agreement with the geometry of the system when in Hard

state. Moreover, a so high reflection bump has never been detected in the atoll source. Therefore, the ”power law” model, 1), it is more physically applicable to these data.

The power law component could originates from a non-thermal emission or by the presence of a hybrid thermal-non thermal composition of the electron plasma as already revealed from the source 4U 1820–30 during the island state (see section 5.1.3 and discussion 5.1.4) [127]. In the Hard spectrum (D) the relative flux contribution for E>60 keV is about 7%, similar to the value found in the Hard state of 4U 1820-30.

5.4 4U 1812–12

4U 1812–12 was discovered as a weak galactic source by the Uhuru satellite in 1970 [93]. Type 1 X-ray bursts were detected for the first time with Hakucho and the burst detection allowed to determine the nature of the compact object as a neutron star in a Low Mass X-ray Binary system [98]. During the Galactic Bulge monitoring campaign performed in the period 1996-2001 with the Wide Field Cameras (WFCs) on board BeppoSAX, several X-ray bursts were detected and in most of them a clear photospheric radius expansion due to Eddington-limited burst luminosity was observed. This allowed to estimate the source distance at 4.1 ± 0.5 kpc. At energies above 5 keV, the bursts showed a double peaked profile that became more evident at higher energy [92].

A broad band spectrum of the persistent emission and rapid X-ray variability has been revealed during simultaneous observations with *BeppoSAX* and *RXTE* on April 20, 2000. Emission above 20 keV has been reported while the source was in a Hard spectral state with a 1-200 keV flux of 1.1×10^{-9} ergs s^{-1} cm^{-2} [90].

The persistent emission at low energy, revealed by Chandra on June 14, 2000, is characterized by a 2-10 keV flux of about 4×10^{-10} ergs s^{-1} cm^{-2} [100]. The source was still in the Hard state during the RXTE observation in June and July 2001 with a 2-10 keV flux of 3.8×10^{-10} ergs s^{-1} cm^{-2} [97]. Like most of the bursters, 4U 1812–12 is classified as an atoll source [99].

5.4.1 *INTEGRAL* and *BeppoSAX* observations

Since March 2003, this source has been observed and is still being monitored, by the *INTEGRAL* observatory in the framework of the GCDE programme. We report here on the analysis performed with *INTEGRAL*/IBIS on both the persistent and bursting behaviour [113]. We analysed all the data in which 4U 1812–12 was within the IBIS field of view. The observations covered a non-continuous period from 2003 March 11^{th} to 2004 October 20^{th} (from orbit 49 to 246) for a total of 1322 ScWs.

A well detail hard X-ray continuum emission up to 200 keV has been detected. Moreover during the observing campaign, 4 bursts triggered the INTEGRAL Burst Alert System (IBAS) [96] from a direction consistent with the 4U 1812–12 error box.

We do not report on JEM-X [51] results, because when 4U 1812–12 was in the JEM-X field of view, it was not detected in the mosaic image, due to the low flux.

For the continuum emission study, it is essential to have as broad as possible spectral coverage. For this reason we have combined the IBIS (20-200 keV) data with the *BeppoSAX* LECS (0.5-4 keV) and MECS (1.5-10 keV) data obtained in 2000. Even if these data are not simultaneous, combining spectra is meaningful in view of the very-low observed variability of this source (see section 5.4.2 for more details). We have used the public data obtained with *BeppoSAX* between 20 April at 18:51 UT to 21 April 2000 at 13:23 UT. The publicly available data from the MECS and LECS instruments have been downloaded from the on line archive of *BeppoSAX*[1].

5.4.2 Continuum emission Results

Figure 5.20 shows the IBIS light curves in the 20-40, 40-60, 60-80 and 80-200 keV energy bands for the whole monitoring period. Each point corresponds to the source count rate (at a signal to noise ratio $>3\sigma$) for a single pointing. The source is significantly detected up to 200 keV and shows the same behaviour in all energy bands, revealing a persistent and moderately ($\sim$ 20%) variable continuum emission. In the 20-40 keV band, the average source flux corresponds to $\sim$ 26 mCrab.

To search for a possible correlation between flux and spectral variation, we derived

[1] http://www.asdc.asi.it/

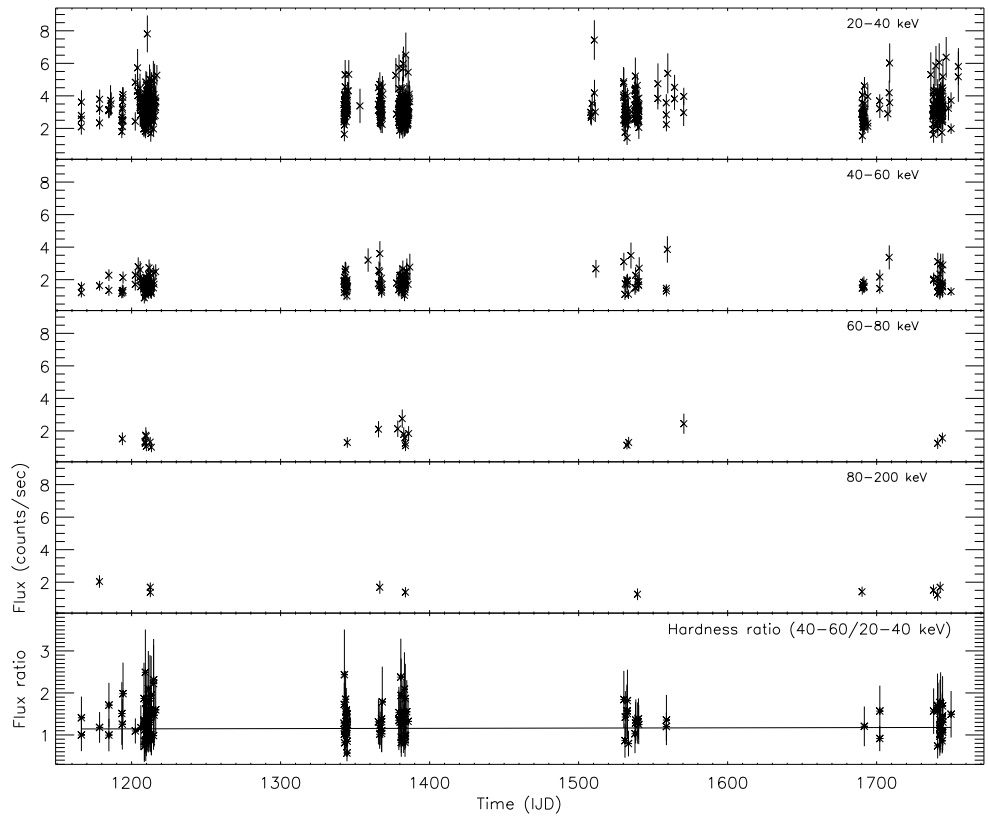

Figure 5.20: 4U 1812–12 IBIS/ISGRI light curves, in the 20-40, 40-60, 60-80, 80-200 keV energy bands; and the hardness ratio of the 40-60 to 20-40 keV flux. The observation period is between 2003 March 11^{th} to 2004 October 20^{th}, and each data point rapresents a single pointing.

the hardness ratio in the 40-60/20-40 keV flux. The null slope (with a $\chi^2_r \sim 1$) in the bottom panel of Figure 5.20 indicates that, as expected, there is no spectral variability. Spectra have been extracted for each pointing and, in view of the lack of flux variation, it has been possible to add all the spectra to increase the signal to noise ratio. The final spectrum has been obtained for a total time of 165 ks, and does not include any of the burst events. This spectrum is well represented by a thermal comptonization model that indicates that the source was in the Hard spectral state, the same state in which the source was found during the contemporaneous *BeppoSAX* and *RXTE* observation in 2000 [90]. Because of this and of the weak variability of the source, we combined the 2000 BeppoSAX low energy data with the IBIS data, even though

Table 5.8: Spectral fitting parameters of the 4U 1812–12 persistent emission. The best fit is a sum of comptonization (CompTT) and blackbody (bb) models.

Parameters	wabs×(bb+CompTT) value
N_H	$1.5^{+0.1}_{-0.1} \times 10^{22}$ cm^{-2}
T_0 (keV)	$0.3^{+0.1}_{-0.1}$
kT_e (keV)	$17.5^{+1.7}_{-1.4}$
τ	$2.3^{+0.2}_{-0.2}$
$norm_{CompTT}$	$7.6^{+1.0}_{-0.9} \times 10^{-3}$
kT_{bb}(keV)	$0.6^{+0.1}_{-0.1}$
$norm_{bb}$	$7.5^{+1.4}_{-1.4} \times 10^{-4}$
χ^2_r(d.o.f)	1.03 (514)
$Flux_{20-200\,keV}$	4.2×10^{-10}erg cm^{-2}s^{-1}
$Flux_{1-10\,keV}$	3.2×10^{-10}erg cm^{-2}s^{-1}

they are not simultaneous. The intercalibration between the three instruments shows agreement: the relative normalization factor of ISGRI with respect to LECS and MECS is 1.03±0.05, while the relative normalization factor of LECS with respect to MECS is 0.67±0.07. The spectrum thus obtained has been fitted with different models. We always assume a systematic error of 0.01 for the MECS and LECS and of 0.02 for ISGRI. The best fit model, a comptonization model `CompTT` [57] plus a low energy blackbody component, `bb`, is reported in Table 5.8, while the spectrum is shown in Figure 5.21. The low energy data can also be fitted by the multicolor disk black body (`diskbb`) model [16], with similar parameters and χ^2_r results.

The IBIS high energy sensitivity provides a better evaluation and error constraint of the comptonization parameters (kT_e=$17.5^{+1.7}_{-1.4}$ and τ=$2.3^{+0.2}_{-0.2}$ with χ^2_r=1.03) compared to the ones obtained by *BeppoSAX* in 2000 (kT_e=$36.0^{+78.0}_{-9.0}$ keV, τ=$3.0^{+0.7}_{-1.8}$ with χ^2_r=1.03 [90]).

The 20-200 keV flux value derived from IBIS is 4.2×10^{-10} ergs cm^{-2} s^{-1}, and the 1-200 keV flux value, combining LECS MECS and IBIS, is 9.1×10^{-10} ergs cm^{-2} s^{-1}. Assuming a source distance of 4.1 kpc [92], the bolometric luminosity is 2×10^{36} ergs s^{-1} that corresponds to $L/L_{Edd} \sim 0.01$ (for a neutron star mass M=1.4$M_\odot$).

Parameters	**Burst A** 2003-04-25 UT 10:54:28		**Burst B** 2003-09-06 UT 00:23:49		**Burst C** 2003-09-27 UT 16:08:52		**Burst D** 2004-10-04 UT 03:15:53	
	1^{st} peak	2^{nd} peak	1^{st} peak	2^{nd} peak	1^{st} peak	2^{nd} peak	1^{st} peak	2^{nd} peak
$kT_{\rm bb}$ (keV)	$2.7^{+0.6}_{-0.5}$	$3.1^{+0.5}_{-0.4}$	$2.7^{+0.6}_{-0.5}$	$2.2^{+0.4}_{-0.3}$	$2.3^{+0.5}_{-0.4}$	$2.7^{+0.4}_{-0.3}$	$1.9^{+0.4}_{-0.3}$	$2.3^{+0.3}_{-0.3}$
$R_{\rm km}/d_{10}$ kpc	10.5±5.1	7.0±2.5	10.9±5.8	33.1±10.7	22.1±10.4	10.3±3.7	76.3±26.8	28.3±9.8
χ^2_r	1.6	1.2	1.0	1.3	1.4	1.3	1.9	1.8
duration (s)	4	9	5	8	5	9	4	6
Counts s^{-1}	116 ±18	104±12	64±17	153±14	143±19	129±15	177±21	176±17
$\text{Flux}^{a}_{15-30\,\rm keV}$	1.18	1.03	1.12	2.05	1.86	1.35	3.08	2.28

[a] In unit of 10^{-8} ergs cm^{-2} s^{-1}.

Table 5.9: Parameters of the burst peaks. The spectral model applied is the blackbody model (bbodyrad).

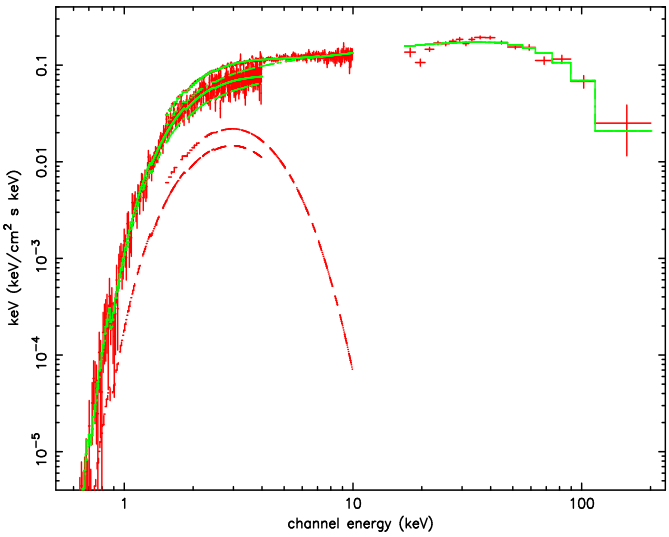

Figure 5.21: *INTEGRAL*/IBIS/ISGRI and *BeppoSAX*/LECS and MECS spectrum of the persistent emission of 4U 1812–12, with the CompTT plus blackbody models.

We have also analysed the recent publicly available *RXTE*/PCA spectrum data[2] of a 4U 1812-12 observation in July 15, 2004 to check for a possible source spectral state change. The analysis of this data shows the flux in agreement with the SAX/IBIS one and the spectrum has similar parameters and χ^2_r value.

5.4.3 Burst emission results

Four bursts were detected during the *INTEGRAL* GCDE campaign; the light curves for two energy bands (15-20 and 20-30 keV) and the whole band 15-30 keV, with a temporal bin of 1 second, are shown in Figure 5.22. Above 30 keV there is no detection of the burst emission. The upper limit of the persistent emission up to 30 keV during the bursts is about 20 counts s^{-1} (corresponding to 0.2 Crab). The burst profiles are clearly double peaked and in each case the first pulse shows a fast rise ($\sim$1 s) shape. The burst fluxes reach up to 2 Crab in the 15-30 keV band. In Table 5.9 we report the characteristic parameters of the 4 bursts (burst A, B, C, D taken in chronological order).

The burst avarage spectra are affected (in the ISGRI band) by “switch off” during

[2]downloaded from the on line archive of HEASARC http://heasarc.gsfc.nasa.gov/docs/archive.html

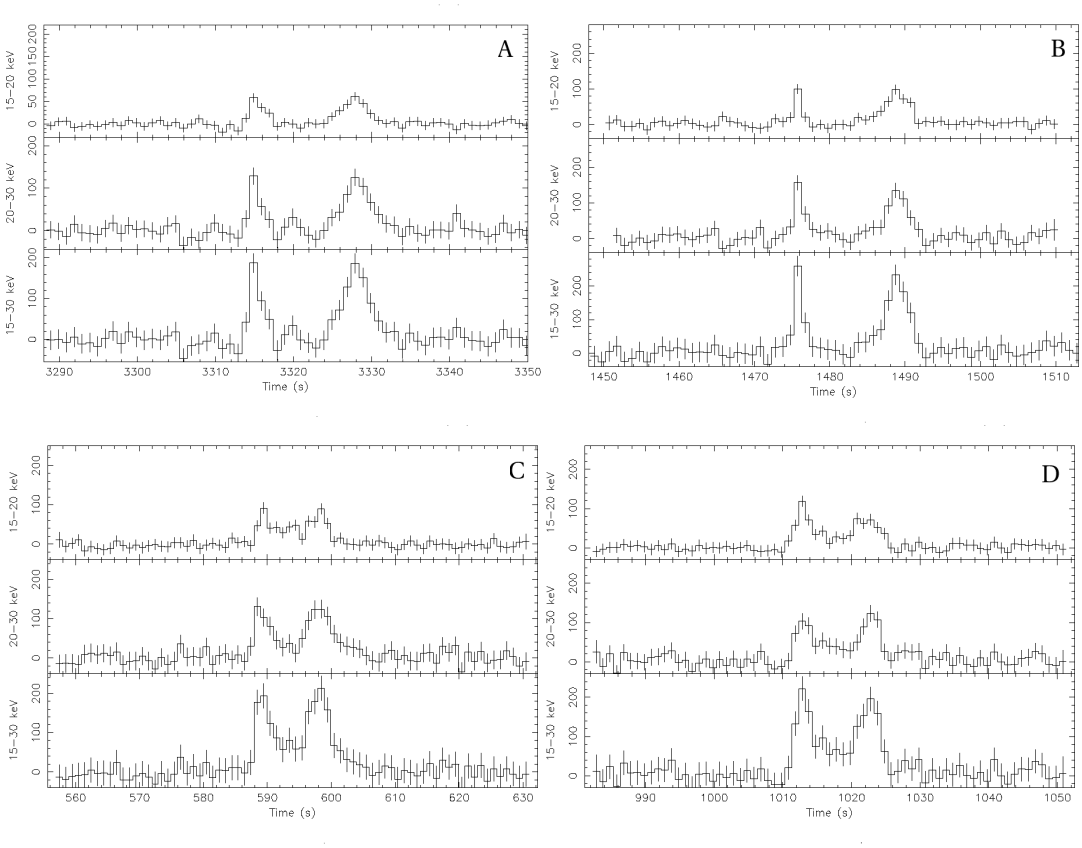

Figure 5.22: IBIS/ISGRI light curves (counts s^{-1} vs time) of the 4 bursts of 4U 1812–12 in the 15-20, 20-30, 15-30 keV energy bands, with temporal bin of 1 second.

the expansion so that we have extracted a separate spectrum from each burst peak. We have fitted them with a black body model and the best fit parameters are reported in Table 5.9. A comparison between the burst and persistent emission spectra is shown in Figure 5.23.

5.4.4 Discussion and conclusions

The IBIS observation has allowed us to follow the high energy behaviour of 4U 1812–12. During the long monitoring period, the light curves show that the persistent source flux is almost constant and with the same behaviour in all the light curves energy bands.

Combining the IBIS/ISGRI spectrum with the non-contemporaneous LECS and MECS spectra, when the source was in the same spectral state, we obtain a broad band

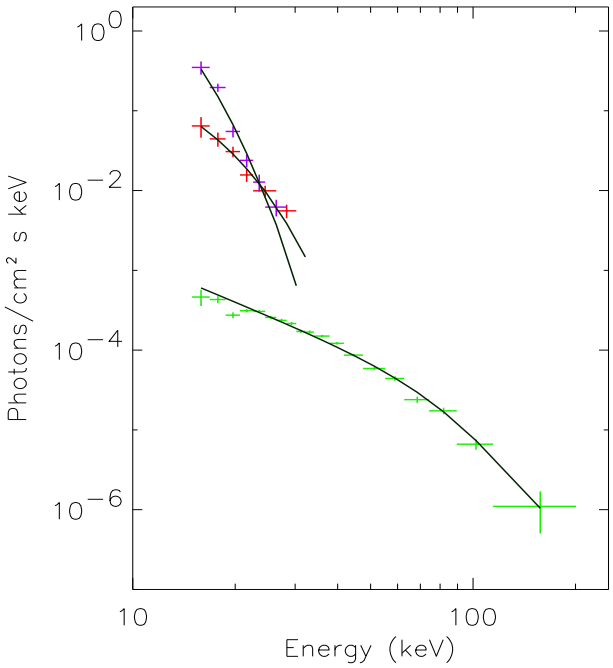

Figure 5.23: IBIS/ISGRI spectrum of the 4U 1812–12 persistent emission compared with spectrum of the most and the least intense bursts detected. The solid lines describe the spectral models: blackbody for the bursts and comptonization for continuum emission.

energy spectrum well represented by a soft thermal component (with a temperature of 0.6 keV) plus a Compton emission with an electron temperature, kT_e, of $\sim$ 18 keV and an optical depth of the plasma, τ, of $\sim$ 2.3. The 1-200 keV luminosity is 2×10^{36} ergs s^{-1}. These results are in agreement with the high energy behaviour of an atoll source in the Hard state [32]. Then, we confirm that 4U 1812–12 spends most of its time in this Hard state (as is also shown by results from the 2004 *RXTE*/PCA data) as well as the presence of a hard emission extending up to 200 keV.

The hard component is due to the comptonization of soft photons in a hot region between the neutron star and the accretion disk. The soft component can be represented by a single-temperature black body model or alternatively by a multicolor disk black body, and hence we cannot determine if the origin of this emission is from the neutron star surface or from the accretion disk.

The 4U 1812–12 IBIS data also allowed us to study the bursting activity, even if

most of the burst emission is well below the ISGRI low energy theshold (15 keV). In fact, because of the relatively high bursts fluxes and the well-defined instrument response, we can still derive the spectral parameters of the bursts.

Type I bursts are due to thermonuclear flashes on to neutron star surface. The spectral softening, typical of this type of burst, is not evident because of the high energy band (15-30 keV) in which we have observed the burst events, but the type I nature of the bursts is very well established by previous measurements at lower energy [92]. The energy spectra of the detected bursts are satisfactorily described by a blackbody model whose temperature changes in the range kT=1.9-3.1 keV, according to the thermal nature of these events. This range of temperature is compatible with the temperature of other bursts previously detected from 4U 1812–12. The observed high energy emission of the 4 bursts has a double peaked profile, typical of Eddington-limited events [8]. The burst profiles are similar in the 15-20 and 20-30 keV ranges, and the duration of the second peak is always longer than the first one as expected for double peaked bursts [8]. Decay times and energy release are typical of the helium burning regime [10].

5.5 4U 1722–30

4U 1722–30, also known as GRS 1724-30, is a bright LMXB located in the Globular Cluster Terzan 2 [102]. The observed Type 1 X-ray bursts indicate that the compact object is a weakly magnetized neutron star [104] [102]. *RXTE* observations suggest that its timing properties are typical of an atoll source [105]. 4U 1722–30 is a persistent though variable source, and it is one of the first neutron star systems from which hard X-ray emission (E $>$35 keV) was detected by SIGMA with a power law spectrum extending above 100 keV, with photon index $\Gamma \sim$1.65 [101]. While previous EXOSAT observation didn't reveal flux above 10 keV [103]. *BeppoSAX* and *RXTE* allowed a broad band observations, detecting the source with a Comptonized spectrum extending up to 200 keV, plus an additional soft componenet (below 3 keV), described by a blackbody emission.

5.5.1 *INTEGRAL* observation

We have studied the sources with *INTEGRAL* during the period October 2003 - April 2005, collecting a total of 883 pointing for IBIS and 256 pointings for JEM-X. Because of this long term monitoring, *INTEGRAL* detected the source in different spectral states and for the first time a detailed spectral analysis of different spectral states has been performed.

5.5.2 Light curves and hardness-intensity diagrams

In Figure 5.24 the light curves with JEM-X and IBIS in different energy bands are showed. In the top panel are reported the ASM monitoring during the same period. The source reveals a flux variation (similar to outbursts) in the soft band ($<$20 keV), while in the hard ones ($>$20 keV), when it is detected the flux changes to a small extent.

We construct two hardness-intensity diagrams, the first one with the IBIS and JEM-X contemporaneous pointings and the second one with JEM-X only. Both are shown in Figure 5.25, with indicated the Intensity and Color bands used. Each point correspond to a single ScW.

The source moves through the diagram showing spectral changes. We indicated with different color the different spectral data sets, which observations log is reported in Table 5.10. The purple data set are present only in the JEM-X/JEM-X hardness intensity diagram because of the lack of high energy detection by IBIS. This data set correspond, in fact, to a Soft (banana) spectral state. The green and red pointings corresponds to an hardening of the sources that enters the Hard (island) spectral state. These pointings are reported in both the hardness-intensity diagrams.

5.5.3 Spectral analysis

We collected the data corresponding to the same spectral state and performed the spectral analysis. We modeled the data with different spectral models, as for the other sources.

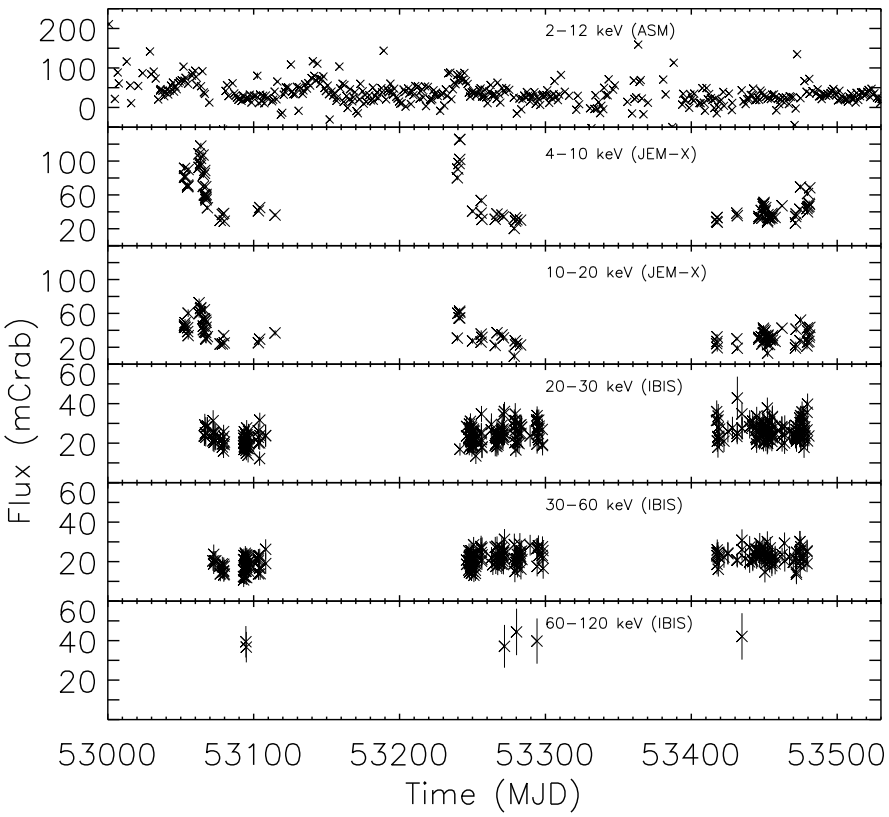

Figure 5.24: *INTEGRAL* and ASM/*RXTE* light curves of 4U 1722–30.

Soft state

For the spe1 data (see Table 5.10) the bets fit model is rapresented by a black body model (or also simple black body model) plus a comptonization model with parameters showed in Table 5.11. Changing the diskbb model with the simple black body model the fit doesn't change.

The source shows this spectral state during the soft "outbursts" clearly evident in the JEM-X light curve, when it isn't detected above 30 keV.

The spectrum, model and residuals are showed in Figure 5.26. The unabsorbed bolometric luminosity during this spectral state corresponds to 1.8×10^{38} ergs s^{-1}, i.e. L/L_{Edd}=0.9 (assuming a distance source of 9.5 kpc [11]).

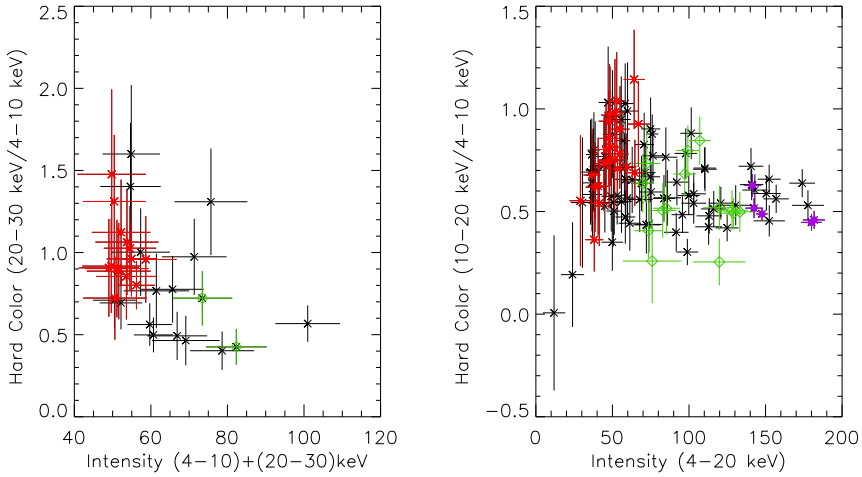

Figure 5.25: *Left:* IBIS-JEM-X Very hard color–intensity diagram. *Right:* JEM-X hard color–intensity diagram. The colors identify the spe1 (purple), spe2 (green) and spe3 (red) data sets (see Table 5.10).

Table 5.10: The log of the *INTEGRAL*/IBIS and JEM-X data used for spectral fitting of 4U 1722–30.

Data set	Time start (MJD)	Exposure (ks) IBIS ; JEM-X	Spectral state
spe1 (purple data)	53239.0	9.6 ; 24.4	Soft
spe2 (green data)	53241.2	66.1 ; 25.9	Hard/Intermediate
spe3 (red data)	53431.2	116.1 ; 65.5	Hard

Hard and Hard/Intermediate states

The green and red spectral data sets corresponds to the hardening of the source. The Intermediate state is detected just after the soft ”outburst” showed in the light curve, and the Hard state soon after this.

The Hard/Intermediate state is well rapresented by the diskbb model plus a comptonization model. For the Hard state, the best fit is the simple comptonization and by adding the diskbb component the fit doesn’t improve. The plasma temperature rises with the hardening, while the optical depth decreases, as indicated in Table 5.11.

In the Hard state the plasma temperature is not contrained very well and there is

the indication of a lack of cut-off, similarly to the Hard state of the atoll 4U 1608-522 [106].

Reflection component doesn't improve the fits.

The bolometric luminosity of the Intermediate state corresponds to 1.2×10^{38} ergs s^{-1}, that yields a 0.6 $L_{\rm Edd}$. The bolometric luminosity of the Hard state corresponds to 1.4×10^{37} ergs s^{-1}, i.e. a $L_{\rm Edd}$ ratio of 0.07.

Table 5.11: Spectral fitting results for the JEM-X and IBIS broad-band spectra of 4U 1722-30. The model is CompTT for spe3 and CompTT + diskbb for spe1 and spe2.

parameters	spe1	spe2	spe3
kT_0 (keV)[a]	0.40	1.33	0.81
$kT_{\rm e}$ (keV)	$2.21^{+0.20}_{-0.09}$	$11.37^{+1.31}_{-0.56}$	$40.36^{+47.03}_{-15.06}$
τ	$9.06^{+9.65}_{-3.40}$	$1.33^{+0.19}_{-0.09}$	$0.48^{+0.42}_{-0.35}$
$\rm norm_{CompTT}$	$0.46^{+0.09}_{-0.18}$	$1.19^{+0.27}_{-0.42}\times10^{-2}$	$3.79^{+2.78}_{-3.79}\times10^{-3}$
$kT_{\rm in}$	$0.46^{+0.10}_{-0.15}$	$0.54^{+0.02}_{-0.02}$	–
$\rm norm_{\textit{diskbb}}$	$2.13^{+4.93}_{-0.42}\times10^{4}$	$1.42^{+0.40}_{-0.32}\times10^{3}$	–
χ^2_r(d.o.f)	1.27(30)	1.03(41)	0.70(55)
$F_{4-20\rm keV}$[b]	2.8×10^{-9}	8.1×10^{-10}	6.4×10^{-10}
$F_{20-200\rm keV}$	3.7×10^{-11}	1.5×10^{-10}	3.3×10^{-10}

[a] Fixed parameters

[b] The Fluxes are in units of erg s^{-1} cm^{-2}

5.5.4 Discussion and conclusions

The *INTEGRAL* observations of 4U 1722-30 permit to understand that the X-ray behaviour of this source is very similar to a X-ray transient even if a real "quiescent" state is never reached. In the X-ray light curves the outbursts, with spectral changes typical of transient sources, are evident, as also confirmed by the color-intensity diagrams, such as the ones for the transient source 4U 1608-522 (see section 5.2) [106].

At high soft flux level the source was in Soft state, followed by hardening. During the Soft state the source doesn't show emission above 30 keV, and the spectrum is well described by a cold and optically thick Comptonized corona plus a soft black body emission coming from either the accretion disk or the neutron star.

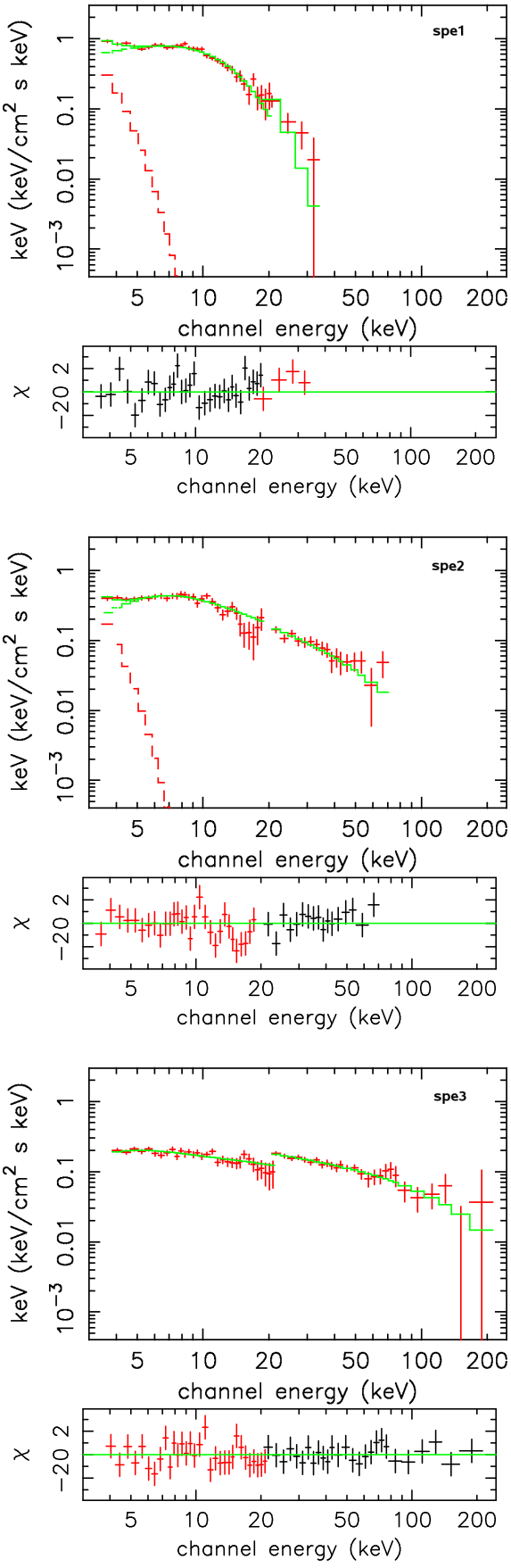

Figure 5.26: IBIS and JEM-X energy spectra of 4U 1722–30, with the residuals of the data to the model. Spe1 corresponds to the Soft spectral state; spe2 to the Hard-Intermediate; spe3 to the Hard. The models applied are the blackbody plus a Comptonization for spe1 and spe2 data sets and only a Comptonization for spe3. The best fit parameters are reported in Table 5.11.

During the hardening the contribute of the soft component decreases, with a corresponding increase of the hard X-ray emission (up to 200 keV) described by a hot and optically thin Comptonizing corona, without evidence of an energy cut-off.

As for the transient source 4U 1608-522 (section 5.2.4) , we estimated the inner radius of the accretion disk in the soft and hard/intermediate state and derived a increasing in its value (from 5 to 20 km), suggesting an extension of the inner radius during the hardening [106].

5.6 XB 1832–330

Firstly reported as H 1825–33 from observation with the Einstein observatory (HEAO-1) [108], and later confirmed by ROSAT as a X-ray source member of the Galactic globular cluster NGC 6652 [112], this source was then catalogated as atoll type LMXB with name XB 1832–330 [115].

The long exposure on the galactic bulge region performed with the WFCs on board *BeppoSAX*, allowed to discover the presence of Type I X-ray bursts emission [110], evidencing the neutron star nature of the compact object.

A broad band (0.1-200 keV) spectral study of the persistent emission was made by Parmar et al. (2001) with the Narrow Field Instruments (NFIs) of the BeppoSAX satellite. The spectrum was well described by a disk-blackbody and a comptonization (`CompTT`) component plus the addition of a partial covering of the disk. A 0.1-200 keV luminosity of 4.4 $\times 10^{36}$ erg s^{-1} has been reported for a distance of 9.2 kpc (derived from optical method [107]).

This source belong to the short period binary systems (P$<$ 1 hr) and its optical counterpart is identified with a blue variable object with $M_V = 3.7$ [109].

5.6.1 *INTEGRAL* observations

INTEGRAL data analysis includes all the public pointings in which XB 1832-330 was within the ISGRI/IBIS fully coded field of view ($9^\circ \times 9^\circ$) [47]. The observations cover the period from 2003 March 22 to 2005 September 25 for a total of 132 ScWs. We do

not report on JEM-X results because the source was not detected in the mosaic images, because of the low flux level.

5.6.2 Time behaviour

Light curves of all the monitoring period with IBIS in three energy bands, 20-40, 40-60 and 60-120 keV have been extracted, and are showed in Figure 5.27. Each cross corresponds to the source counts rate for a time bin of 1 ScW at a signal to noise ratio grater than 3σ.

In the top panel it is also reported the *RXTE*/ASM one day averaged light curve in the 1.5-12 keV for the same observation period. The source shows a weak variability and no hint of spectral transition was detected. The corresponding flux in the 20-40 keV is of about 19 mCrab.

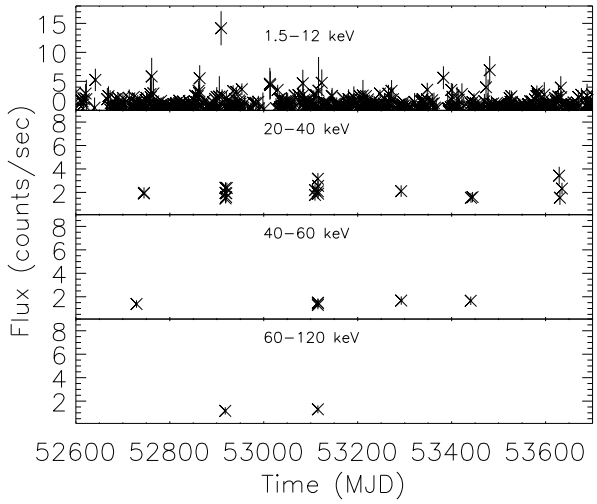

Figure 5.27: 2003-2005 light curve of XB 1832–330 with IBIS (with time bin of 1 ScW) and ASM (with time bin of 1 day). Each point rapresent the count rate to time bin.

5.6.3 Spectral analysis

We have extracted spectra for each pointing and because of the lack of flux variation, as revealed by the IBIS (and ASM) light curves, we added all the available spectra to

increase the signal to noise ratio. The final spectrum correspond to a total exposure time of 178 ks. This spectrum extends up to 150 keV and it is well described by a

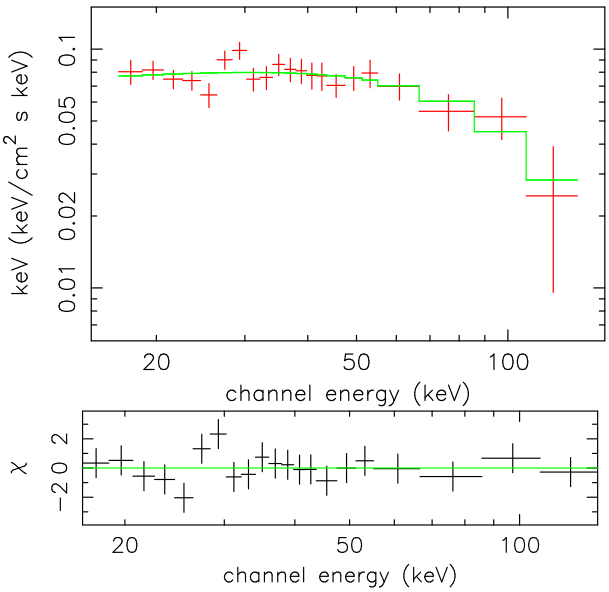

Figure 5.28: IBIS everage spectrum of XB 1832–330. The model (dotted line) is the CompTT comptonization model. See Table 5.12 for the best fit parameters. The residuals to the model are shown in the bottom panel.

Comptonization model (`CompTT`) [114] with a thermal plasma temperature, kT_e, of about 22 keV and optical depth of the electrons plasma, τ, of about 2, with a χ^2_r=0.9. The temperature of the seed photons, kT_0, has been frozen at the best fit value of 0.15 keV, and a better evaluation is not possible because of the IBIS energy band.

Data, model and residuals of the spectrum are reported in Figure 5.28, while Table 5.12 lets the best fit parameters, as well the flux in different energy bands and the bolometric luminosity estimated for a source distance of 9.2 kpc.

The bolometric luminosity corresponds to $L/L_{\rm Edd} \sim 0.03$ (for a neutron star mass of 1.4 $M_\odot$).

The electron plasma temperature and the plasma optical depth are in the typical range values of the LMXBs when in Hard spectral state.

Table 5.12: Best fit parameters of CompTT model for the IBIS data of XB 1832–330.

Parameter	CompTT values
kT_0 (keV)	0.15 (frozen)
kT_e (keV)	$21.3^{+12.8}_{-4.7}$
τ	$1.8^{+0.7}_{-0.9}$
$\mathrm{norm}_{\mathrm{CompTT}}$	$0.006^{+0.001}_{-0.002}$
χ^2_r(d.o.f)	0.9(17)
$F_{20-40\mathrm{keV}}$	8.8×10^{-11}erg s^{-1} cm^{-2}
$F_{40-100\mathrm{keV}}$	9.7×10^{-11}erg s^{-1} cm^{-2}
L_{bol}	5.5×10^{36}erg s^{-1}

5.6.4 Discussion and conclusion

The *INTEGRAL*/IBIS long monitoring of the source XB 1832–330 shows that the spectrum of this compact source extend up to 150 keV and it is well described by a thermal Comptonization with the temperature of the electrons, kT_e, of 22 keV and optical depth, τ, of 1.8. These parameter values are compatible with those found in previous *BeppoSAX* analysis ($kT_e = 25.3 \pm 1.8$ keV $\tau = 1.77 \pm 0.07$ [111]). Moreover, assuming a distance of 9.2 kpc, the 0.1-200 keV luminosity as derived from the model, is 5.4×10^{36} erg s^{-1} that is consistent with the previous *BeppoSAX* measurement.

The IBIS result indicate that in the hard X-ray band the source is a persistent, "stable" one and spend most of the time in the typical Hard state of LMXBs. This behaviour is similar to the one showed by 4U 1812–12 in the same domain of hard X-ray (section 5.4), in spite of both sources are atoll and therefore changes in flux and spectral shape are expected [113].

The hard component of XB 1832–330 is explained as due to the Comptonization of soft photons coming from the accretion disk and the neutron star surface. Unluckily no data are available for the *INTEGRAL* X-ray detector, JEM-X, and we can not investigate the presence of a disk blackbody component that would indicate emission from the disk or/and the neutron star surface.

5.7 4U 1254–690

The source 4U 1254–690 is one the LMXB system that exhibit periodic dips and thermonuclear X-ray bursts. The dips are due to decreases of the soft X-ray flux resulting from obscuration of the X-ray source by the edge of the accretion disk with high inclination of the light of sight. Like most of the LMXBs characterized by bursts emission, 4U 1254–690 is classified as atoll source because of the track observed in the color-color diagram. It is then expected that this source could show flux variation corresponding to spectral state change. So far, only one spectral state has been reported, that is a relatively Soft.

5.7.1 *INTEGRAL* observations

For the data analysis we used all the public pointing in which 4U 1254–690 was within the IBIS/ISGRI [47] and JEM-X fully coded field of view ($9^\circ \times 9^\circ$, and $4.8^\circ \times 4.8^\circ$). The observations cover the period from 2003 January 29 to 2006 March 8 for a total of 49 ScWs for IBIS and 9 for JEM-X. These pointings have been obtained during the Galactic Plane observation.

5.7.2 Light curves

During the observation period the source was significantly detected from JEM-X. Figure 5.29 shows the light curve of the *RXTE*/ASM in the 1.5–12 keV band with a time bin of 1 day. In the same light curve the JEM-X single pointing detections, in the 4–10 keV band as light green diamonds, and in the 10–20 keV as the dark green diamonds, are overplotted.

We also extracted the light curve with a time bin of 1 second but unfortunately no dips or bursts have been detected during the observation of JEM-X.

With the IBIS instrument, the source was detected in the mosaic image of all pointings, up to 100 keV. On the contrary, in the single energy band (we choose 20–40, 40–60, 60–120 keV) of the single pointings the source was not revealed unless for some pointings.

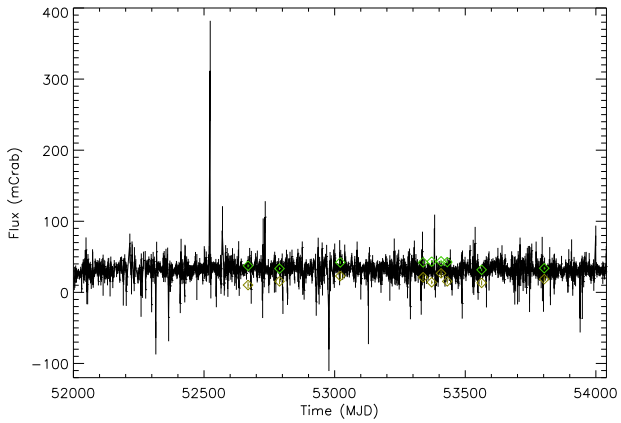

Figure 5.29: 4U 1254–690 light curve with ASM, in the 1.5-12 keV band (black) with 1 day of time bin, and JEM-X, in the 4-10, 10-20 keV band (light green and dark green diamond respectively) with time bin of 1 pointing.

5.7.3 Spectral analysis

We build up the spectrum from all pointings and sum them into a single average spectrum for a total exposure time of 11 ks for JEM-X and 90 ks for IBIS. We tried to fit the spectrum with different spectral model. First, we used the `CompTT` model [114] but the residual shown a soft excess (below 6 keV) so that we added a black body component, `bb` [15]. An F-test indicates that the addition of this component improved the fit with good statistical significance (probability of chance improvement 0.163). The parameter of the best fit model are reported in the Table 5.13.

Changing the black body model with a disk black body model, `diskbb` [16] the fit didn't improve and the parameters of the fit are similar: the inner temperature of the disk, $kT_{\rm in}$, was 0.55±0.25 keV, the temperature of the seed photons, kT_0, was 1.21±0.28 keV, the electron temperature, $kT_{\rm e}$, was 4.48±1.84 keV, and the optical depth, τ, was 2.34±1.54.

Figure 5.30 shows the energy spectrum with the best fit model.

Table 5.13: Spectral fitting parameters of the IBIS and JEM-X data of 4U 1254–690. The best fit is a sum of comptonization (CompTT) and blackbody (bb) models. In the bottom there are the flux values in two energy range.

Parameters	(CompTT+bb) values
T_0(keV)	$1.19^{+0.58}_{-0.17}$
kT_e(keV)	$5.39^{+3.35}_{-2.30}$
τ	$1.85^{+1.20}_{-1.78}$
norm_{CompTT}	$3.30^{+2.18}_{-3.15} \times 10^{-2}$
kT_{bb}(keV)	$0.36^{+0.60}_{-0.25}$
norm_{bb}	$5.88^{+1.53}_{-5.58} \times 10^{-2}$
χ^2_r(d.o.f)	1.09 (26)
$\mathrm{Flux}_{4-20\,\mathrm{keV}}$	7.3×10^{-10}erg cm^{-2}s^{-1}
$\mathrm{Flux}_{20-100\,\mathrm{keV}}$	2.6×10^{-11}erg cm^{-2}s^{-1}

5.7.4 Discussion and conclusion

The *INTEGRAL* long monitoring of the source 4U 1254–690 shows that the spectrum of this dipper extend up the 60 keV and is well described by a thermal comptonization with the temperature of the electrons, kT_e, of 5 keV and optical depth, τ, of 1.8, plus a blackbody component of temperature 0.4 keV. The soft black body component approximates the spectrum of an optically thick, geometrically thin accretion disk and/or the neutron star surface. At higher energy the comptonization component is due to repeated inverse Compton scattering of the soft photons by hot electrons plasma with a thermal distribution of velocities which could originate in a spherical corona or boundary layer of optical depth τ surrounding the neutron star. The observed everage unabsorbed flux in the 4–100 keV energy range is 7.55×10^{-10} ergs cm^{-2} s^{-1} which corresponds to an unabsorbed luminosity of 8.93×10^{36} ergs s^{-1} (for a distance of the source of 10 kpc [116]) that correspond to a L/L_{Edd} ratio of 0.3.

During the observations the source didn't show hard excess (>30 keV) as reported during the *BeppoSAX* observations on 1998 December 22 and 23 [117]. This hard excess was fitted with the addition of a bremsstrahlung components to the Comptonization and blackbody components, suggesting the presence of an extended optically thin

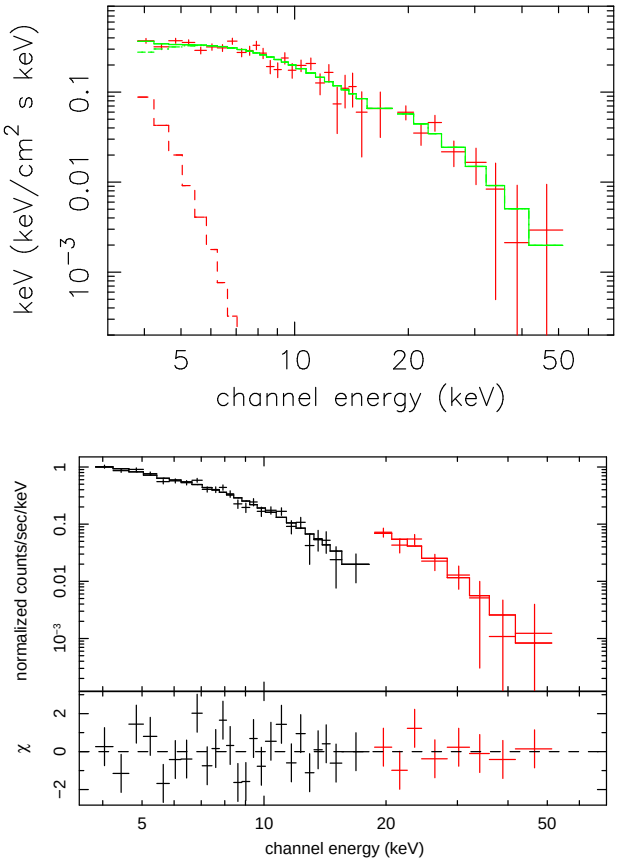

Figure 5.30: IBIS and JEM-X everage spectrum of 4U 1254–690 in energy (top) and in counts with the residuals of the data to the model (bottom). The model is a comptonization model (CompTT) plus a blackbody model (bb). See Table 5.13 for the best fit parameters.

accretion disk corona, ADC [118], probably due to evaporation of the outer layers of the disk illuminated by emission of the compact object. The lack of this component in the *INTEGRAL* monitoring indicates that this feature occurs only occasionally. This could be probably due to a different system geometry (line of sight).

Monitoring of this source is very important and we will make use in the future of all available information from in-orbit high energy satellites.

Chapter 6

Overall discussion and conclusions

6.1 Behaviour of the source analysed

The scientific results reported in Chapter 5 allow us to identify two kind of behaviour from the source sample:

- Sources with spectral changes:

From my analysis we detected spectral changes from the sources 4U 1820–30, 4U 1608–522, 4U 1728–34 and 4U 1722–30. Spectral changes are associated to transient phenomena for two of them, with spectral hardening and softening occurring in a short time; the other ones showed continuum emission with high flux variations coupled to spectral transitions.

- Sources with persistent behaviour:

4U 1812–12, XB 1832–330 and 4U 1254–690 showed a persistent flux with a low level of variability ($< 25\%$) and without spectral changes.

In particular, 4U 1812–12 has been detected only in the Hard state up to now.

6.2 Spectral states observed

The spectral analysis performed and outlined in the previous Chapter, can be summarized with the existence of three type of spectral states for the Atoll sources:

- **Soft state**

  This state (also called ”banana” state) is characterised by a strong black body component with temperature of 0.4-0.6 keV plus a Comptonized component with a low electron temperature ranging from 2 to 5 keV and high optical depth of 2-9. The input photons of the Comptonization have a temperature of 0.2.-1.2 keV.

  The Soft state of transient sources is characterized by a stronger soft component compared to that of the other sources (as example 4U 1608–522 compared to 4U 1254–690). This could be explained by the high flux level reached during the outburst (high luminosity) that imply higher accretion rate and, in turn, high luminosity.

- **Hard state**

  The soft black body component during the Hard state (also known as ”island” state) is of lower intensity and in some cases is not even detected. The Comptonizing corona shows a higher electron temperature (6-60 keV) and a lower value of the optical depth (0.4-3).

  The *main results of this thesis work* is that the **Hard states** show **two different type of behaviour**:

  In the first one, the corona temperature is high and the spectra extends up to 200 keV, and in some cases without a clear high energy cut-off (as for 4U 1608–522 and 4U 1722–30).

  In the second one, the corona has a lower temperature and the Comptonization component contributes to the spectrum up to 50-60 keV, while at higher energy a hard power law with photon index of 2-2.3 dominates (as for 4U 1820–30 and 4U 1728–34). In this last case, the Hard state could be also interpreted as a Comptonization with a hybrid thermal-nonthermal plasma with high temperature (20-30 keV), and a power law at higher energy ($>$50 keV).

- **Intermediate state**

  These is the state in which sources spend a short time just in coincidence with a

spectral state transition. Only a detailed spectral analysis correlated with a photmetric and temporal study allows to detect these kind of short time behaviour and spectra.

The spectral parameters have intermediate values between the Soft and Hard ones. Nevertheless, it is possible to understand when it is Soft-like or Hard-like by the comparison with the values of the parameters for the two main states.

6.2.1 Physical interpretation

From our analysis it is clear that there is a strong variation in the spectral shape between the island and banana state of the Atoll sources, probably due to changes in the accretion flow geometry and coupled with variations in the mass accretion rate.

In spite of the difficulty to precisely determine the soft parameters because of the used limited instrumentation band-width (often at E$>$ 4 keV), still we can draw some remarks and explanations.

The observed ”soft component” is modelled either by the `diskbb` or by `bb` emission, and we don’t manage to discern the origin of this component that could be originate either in the optically thick and geometrically thin accretion disk or NS surface or optically thick boundary layer between the disk and the NS (i.e. western or eastern model). In general we privilege the accretion disk emission origin.

The input seed photons necessary for the Comptonization process could in general have the same origin of the soft photons. This hypothesis is not confirmed by us since we never observed the same temperature value, suggesting a different origin for the seed photons.

During the **Hard state** the observed disk black body emission is either not detected or has a low temperature values compared to that of the Soft state. This implies a larger extension of the inner radius of the accretion disk ($R_{\rm in} \propto T^{-3/4}$, section 2.1.1). The input seed photons have higher temperature compared to the inner disk temperature implying a smaller emission region. As a consequence they could originate from the NS surface or from the inner part of the disk such us the optically thick boundary layer. The seed photons interact in a hot and optically thin plasma supposed to be

around or inside the extended accretion disk, and causing the high energy Comptonized component observed in our analysed spectra.

During the **Soft state** the disk extends close to the NS surface as showed by the high values of the inner disk temperature observed. In this case, Comptonization takes place in an optically thick and cold plasma and the seed photons have a low temperature and could originate from the outer part of the disk. Because of the extension of the disk close to the NS, the boundary layer is optically thick and could be the region that give rise to the Comptonization.

The Hard and Soft states observed in our sample correspond to various ratios of Luminosity to the Eddington Luminosity. In fact, L/L_{Edd} ranges from 0.01 (for 4U 1812–12) to 0.9 (for 4U 1722-30 in Soft state), as expected for the Atoll source. Moreover this ratio decreases from the Hard to the Soft states, implying changes in the mass accretion rates.

All these informations are clues that the spectra from the NS systems and BH system are very similar, especially in the Hard state during which high temperatures of the corona are detected and the spectra extends up to 200 keV. This confirms that the ”corona temperature” method is not a valid tool to discern from BH and NS systems (as pointed out in Chapter 2).

6.3 Luminosity diagram of our sample of LMXBs

The final and important remark is about the Luminosity diagram of the sources spectral state that have been reported in Chapter 5 for each single source.

We derived the flux values from the best fit models of each sources state detected in two energy bands: the *soft*, 4-10 keV, and the *hard*, 20-200 keV. We estimated the luminosity in these two energy bands using the distances reported in the literature, giving priority to the values derived from burst with photospheric radius expansion whenever possible.

Figure 6.1 shows the luminosity diagram in the two energy bands of all the sources states.

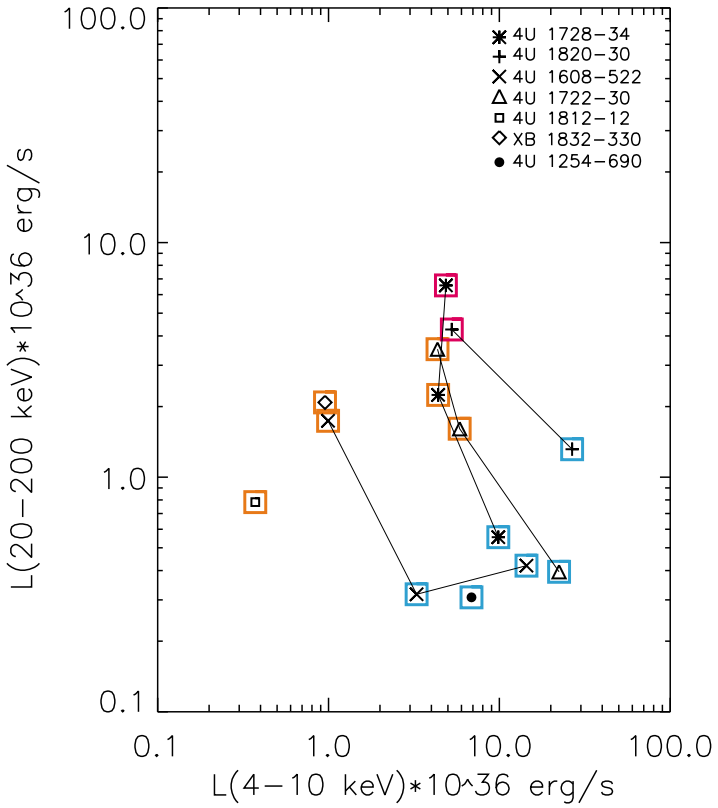

Figure 6.1: Luminosity diagram of the source sample analysed. For each source it is shown the spectral states detected, joined with a line for the same source. The blue boxes show the Soft states, the orange one the Hard states and with red boxes the Hard state with hard power law tail. The Intermediate states belong to the nearing spectral state-group.

Comparing the luminosity between different spectral states it is clear that they are positioned in different zones. The Soft states are all localized at $L_{soft} > 6 \times 10^{36}$ erg s^{-1} and $L_{hard} < 1.4 \times 10^{36}$ erg s^{-1} (blue boxes). On the contrary the Hard states are located all at $L_{soft} < 6 \times 10^{36}$ erg s^{-1} and $L_{hard} > 0.7 \times 10^{36}$ erg s^{-1} (orange and red boxes). The Intermediate states observed are located between the Soft and Hard states. By the closeness to the Soft state group or the Hard group we could say that the Intermediate state is associated more to a group than to the other one. In fact the Intermediate state of 4U 1722–30 and 4U 1728–34 is more similar to the Hard state, while the Intermediate state of 4U 1608–522 to the Soft state group.

The Luminosity diagram seem to be a good clue to characterize the Soft or Hard nature of the source spectral states.

We indicate with red boxes the Hard states with the power law tail i.e. with a electron population with hybrid thermal and not thermal velocity distribution. These correspond to high value of L_{soft}, $\simeq 5 \times 10^{36}$ erg s^{-1} and to the highest value of L_{hard}, $> 4 \times 10^{36}$ erg s^{-1}.

We investigated the existence of a different luminosity correlation between Soft and Hard states using the Luminosity ratio $R = L_{soft}/L_{hard}$. R values ranges from 7.2 to 56.5 for the Soft states, while for the Hard states R values are in the range to 0.45 to 3.64.

Respect to the Burtser Box reported by Barret et al. 2000 [28], our diagram has in addition the information of the spectral changes, being the luminosities not an averaged value but computed for the different spectral states detected from the same source. The sources in our sample also indicate the existence of a critical value for L_{hard} below which the NS systems are positioned in the Bursters Box as reported by Barret et al. 2000 (L_{crit} 1.5×10^{37} erg s^{-1}).

6.4 Future work

We aim to better investigate the hard tail detected during Hard states of Atoll sources, in correlation with state transition, timing properties and Radio emission.

A larger sample will be studied to inquire the critical value for L_{hard}, and further investigate to establish hints to observationally distinguish between NS and BH systems.

Appendix A

Other X-ray missions relevant for the thesis

A.0.1 *BeppoSAX*

BeppoSAX [120] was a space mission dedicated to X-ray astronomy founded by the Italian Space Agency (ASI) with partecipation of the Netherlands Agency for Aerospace Programs (NIVR). The original mission name was *SAX* (Satellite per l'Astronomia X) and it was renamed *BeppoSAX* after the launch on 30 April 1996, in honor of the Italian physics Giuseppe Occhialini. The spacecraft carries a set of instrument allowing simultaneous high sensitivity ($\sim$ 10 mCrab) observations of sources on the wide energy band 0.1–300 keV, the monitoring (at $\sim$ 10 mCrab sensitivity) of large regions of the sky in 1.5-26 keV band with 3 arcmin angular resolution [131].

The scientific instruments of *BeppoSAX* can be classified in Narrow Field Instruments (NFIs), and Wide Field Instruments (WFIs). The NFI constists of the Low Energy Concentrator Spectrometer (LECS, 0.1-10 keV) [132], three Medium Energy Concentrator Spectrometers (MECS, 2-10 keV) [133], a High Gas Pressure Scintillator Proportional Counter (HPGSPC, 20-120 keV) [134], a Phoswich Detection System (PDS, 15-300 keV) [136]. The WFI consists of two Wide Field Cameras (WFCs, 1.5-26 keV) [135] doveted to transient sources study.

The LECS and MECS consist of grazing incidence X-ray concentartor and of gas

scintillation proportional counter using Xenon.

The HPGSPC is an high pressure scintillator proportional counetr filled with a Xenon and Helium gas mixture, to cover low and medium energies.

Thw WFCs consist of two coded mask aperture cameras, with detector (multi wire proportional counetr filled with gas mixture) and mask of same size, about 25.5×2.5 cm^2.

The PDS detector is composed of 4 actively shielded NaI(Tl)/CsI(Na) phoswich scintillators with a total geometric area of 795 cm^2 and a field of view of 1.3° (FWHM).

The *BeppoSAX* instruments main characteristics are reported in Table A.1 [120].

Table A.1: *BeppoSAX* instruments main characteristics.

Instrument	Band (keV)	FOV ($^\circ$ FWHM)	Ang. res. (arcmin)	Eff. Area (cm^2)	Energy Res. (% FWHM)
LECS	0.1-10	0.5	3.5@0.25 keV	22@0.25 keV	$8x(E/6)^{-0.5}$
MECS	1.3-10	0.5	1.2@6 keV	150@6 keV	$8x(E/6)^{-0.5}$
HPGSPC	4-120	1.1	collimated	240@30 keV	$4x(E/60)^{-0.5}$
PDS	15-300	1.3	collimated	600@80 keV	$15x(E/60)^{-0.5}$
WFC	1.5-26	20x20	3	140@10 keV	18x(E/6)

A.0.2 *RossiXTE*

The Rossi X-ray Timing Explorer was launched on December 30, 1995 from NASA's Kennedy Space Center. It was named as "Rossi"-XTE after the launch in honor of the italian astronomer Bruno Rossi. The satellite was designed to facilitate the study of time variability in the emission of X-ray sources with moderate spectral resolution. Time scales from microseconds to months are covered in a broad spectral range from 2 to 250 keV. RXTE is moneuverable (6 deg/minute) so that it can point to a selected source rapidly. This flexibility allows the instrument to respond to short-lived or new pheomena as they are discovered.

The mission carries two pointed instruments, the Proportional Counter Array (PCA)[139], the High Energy X-ray Timing Experiment (HEXTE) [140] covering the upper energy range. RXTE carries also All-Sky Monitor (ASM) [137] that scans about 80% of the sky every orbit.

The PCA is an array of five Xenon gas proportional counters with a total collecting area of 6500 cm^2, that are sensitive to X-rays with energies from 2 to 60 keV. The instrument properties are:

- Energy range: 2-60 keV
- Energy resolution: $<$ 18% at 6 keV
- Time resolution: 1 ms
- Spatial resolution: collimator with 1 degree FWHM
- Sensitivity: 0.1 mCrab

HEXTE consists of two clusters each containing four phoswich scintillation detectors (of NaI7/CsI). The HEXTE extends the X-ray sensitivity of RXTE up to 250 keV. The basic properties are:

- Energy range: 15-250 keV
- Energy resolution: 15% at 60 keV
- Time sampling: 8 ms
- FOV: 1 degree FWHM
- Sensitivity: 1 Crab $=$ 360 count/s per cluster

The ASM consists of three wide-angle shadow cameras equipped with proportional counters with a total collecting area of 90 cm^2. The instrument properties are:

- Energy range: 2-10 keV
- Time resolution: 80% of the sky every 90 minutes
- Spatial resolution: $3' \times 15'$
- Number of shadow cameras: 3, each with 6×90 degrees FOV
- Collecting area: 90 cm^2
- Sensitivity: 30 mCrab

Appendix B

Publications

1) INTEGRAL *high energy behaviour of 4U 1812–12* (A&A 448, 335-339, 2006)
Tarana, A.; Bazzano, A.; Ubertini, P.; Cocchi, M.; Gtz, D.; Capitanio, F.; Bird, A. J.; Fiocchi, M.
2) INTEGRAL *spectral variability study of the atoll 4U 1820–30: first detection of hard X-ray emission* (ApJ 654, 494, 2007)
Tarana, A.; Bazzano, A.; Ubertini, P.; Andrzej Zdziarski A. A.
3) INTEGRAL *and* BeppoSAX *observation of the transient atoll source 4U 1608–522:from quiescent to hard spectral state*
Tarana, A., Bazzano, A., Ubertini, P. submitted to ApJ
4) INTEGRAL *and* RXTE *observation campaign of the Atoll source 4U 1728–34*
Tarana, A., Bazzano, A., Belloni, T., Homan, ; Mendez et al. in preparation
5) INTEGRAL *spectrum of the low mass X-ray binary 4U 1254–69* (proceeding of The Extreme Universe in the Suzaku Era, Kyoto, Japan, 2006)
Tarana, A.; Bazzano, A.; Ubertini, P.
6) *Following the Colour of the Low Mass X-ray Binary 4U 1820-30 with* INTEGRAL (Proceeding, ESA-SP 622, 2006.)
Tarana, A.; Bazzano, A.; Ubertini, P.; Andrzej Zdziarski A. A.; Federici M.
7) *Observing the high energy behaviour of the low mass X-ray binary XB 1832-330 with* INTEGRAL (Proceeding , ESA-SP 622, 2006)
Tarana, A.; Bazzano, A.; Ubertini, P.; Federici M.

8) *XMMU J174716.1-281048: a quasi-persistent very faint X-ray transient?* (2007 A&A 468L 17)
Del Santo, M.; Sidoli, L.; Mereghetti, S.; Bazzano, A.; **Tarana**, A.; Ubertini, P.
9) INTEGRAL *high-energy monitoring of the X-ray burster KS 1741-293* (2007 MNRAS 380, 615)
De Cesare, G.; Bazzano, A.; Martnez Nez, S.; Stratta, G.; **Tarana**, A.; Del Santo, M.; Ubertini, P.
10) *Simultaneous Multiwavelength Observations of the Low/Hard State of the X-Ray Transient Source SWIFT J1753.5-0127* (2007 ApJ 659, 549)
M. Cadolle Bel, M. Ribo, J. Rodriguez, S. Corbel, S. Chaty, A. Goldwurm, F. Frontera, R. Farinelli, A. **Tarana**, P. Ubertini, P. Laurent, P. Goldoni, and I. F. Mirabel.
11) *Spectral States of the X-Ray Binary IGR J17091-3624 Observed by* INTEGRAL *and RXTE* (ApJ 643, 376-380, 2006)
F. Capitanio, A. Bazzano, P. Ubertini, A. A. Zdziarski, A. J. Bird, G. De Cesare, A. J. Dean, J. B. Stephen, A. **Tarana**
12) *GRB 040403: a faint X-ray rich Gamma-ray Burst discovered by* INTEGRAL (A&A 433, 113,2005)
Mereghetti S., Gotz D., Andersen M.I., Castro-Tirado A., Frontera F., Hartmann D.H., Hjorth J., Hudec R., Pizzichini G., Produit N., **Tarana** A., Topinka M., Ubertini P.
13) INTEGRAL *observation of the X-ray burster KS 1741-293* (Proceeding ESA SP-604, Vol. 1, Noordwijk: ESA Publications Division, ISBN 92-9092-915-4, p. 259 260, 2006)
De Cesare, G.; Bazzano, A.; Stratta, G.; Del Santo, M.; **Tarana**, A.; Ubertini, P.
14) INTEGRAL , *XMM-Newton and Rossi-XTE Observations of the State Transition of the X-ray Transient and Black Hole Candidate XTE J1720-318* (Proceedings of the 5 *INTEGRAL* Workshop 'The *INTEGRAL* Universe', inun.conf. 215C, 2004)
Cadolle Bel M., Goldwurm A., Rodriguez J., Goldoni P., Corbel S., Sizun P., Parmar A., Kuulkers E., Capitanio F., Del Santo M.,**Tarana** A., Ubertini P., Roques J.P., Bouchet L., Farinelli R., Frontera F., Westergaard N.
15) *Two years of* INTEGRAL *observation of the BHC IGR J17464-3213* (Advances in Space Research Vol. 38, Issue 12 , 2006, Pages 2816-2819)

Capitanio, F.; Bazzano, A.; Ubertini, P.; Cesare, G. De; Santo, M. Del; **Tarana**, A.; Joinet,A.

16) *High energy behaviour of the IGR J17464-3213* (Proceedings of the 5 *INTEGRAL* Workshop 'The *INTEGRAL* Universe', inun.conf. 313C, 2004)

Capitanio F., Kretschmar P., Ubertini P., Barlow E.J., Bazzano A., Brandt S., Bouchet L., Budtz-Jorgensen C., Cadolle Bel M., Castro-Tirado A., Dean A.J, De Cesare G., Del Santo M., Farinelli R., Frontera F., Gehrels N., Goldoni P., Goldwurm A., Houvelin J., Lund N., Mirabel F., Natalucci L., Piraino S., Reglero V., Roques J.P., **Tarana** A., Vilhu O., Westergaad N.J., Zdziarski A.A.

17) *Spectral behaviour of an integral sample of Black Hole candidates: initial results* (Proceedings COSPAR 2004, Paris, 18-25 July 2004, Advances in Space Research Vol. 38, Issue 7 , 2006, Pages 1369-1373, 2006)

Ubertini P., Bazzano A., Capitanio F., De Cesare G., Del Santo M., Natalucci L., **Tarana** A., Roques J.P., Jourdain E., Kretschmar P., Zdziarski A. A., Dean A.J, Barlow E.J., Cadolle Bel M., Goldwurm A.

18) INTEGRAL *view on X-ray Bursters* (Proceeding of A Life with stars, 22-26 August 2005 Dublin.

Bazzano, A., **Tarana**, A. et al.

19) INTEGRAL *observation of X-ray Binaries* (Proceeding of The Multicoloured Landscape of Compact Objects and their Explosive Origins 19-23 June 2006, Cefalú, Sicily)

Pietro Ubertini, Antonella **Tarana**, Angela Bazzano, Fiamma Capitanio, Giovanni De Cesare, Melania Del Santo, Mariateresa Fiocchi, Nicola Masetti, Vito Sguera

20) ATEL #456, 11 April 2005: *Discovery of a new X-ray transient IGR J16283-4838 with* INTEGRAL

21) ATEL #885, 18 September 2006: *IGR J17497–2821: a new hard X-ray transient detected by* INTEGRAL

22) ATEL #962, 13 December 2006: INTEGRAL *observation of SWIFT J1626.6-5156*

23) ATEL #953, 29 November 2006: INTEGRAL *hard X-ray observations of the outburst of the AXP CXOU J164710.2–455216*

24) ATEL #1019, 3 March 2007: INTEGRAL *observation of a bright X-ray outburst*

of XTE J1739-302 / IGR J17391–3021
25) ATEL #1021, 5 March 2007: *IGR J17191–2821: a new hard X-ray transient detected by* INTEGRAL
26) ATEL #1228, 4 Ottobre 2007: A new outburst of the recurrent neutron star transient SAX J 1747.0-2853 27) ATEL #1322, 8 December 2007: *Swift/XRT follow-up observations of unidentified INTEGRAL sources (1)*
28) ATEL #1323, 8 December 2007: *Swift/XRT follow-up observations of unidentified INTEGRAL sources (2).*
29) ATEL #1338, 19 Dicembre 2007: INTEGRAL detection of an intermediate long X-ray burst from SLX 1737-282

Bibliography

[1] Tauris T. M. & van den Heuvel E. P. J., ”Formation and evoultion of compact stellar X-ray sources” in *Compact Stellar X-ray Sources*, eds. W.H.G. Lewin and M. van der Klis, Cambridge Astrophys. Ser. 39

[2] Kopal Z., *Colse binary systems*, The international astrophisics series, vol.5.

[3] Castellani V., Giannone P., *Evoluzione stellare*, Ed. Sistema Roma.

[4] *X-ray binaries* Cambridge Astrophys. Ser. 26, ed. W. H. G. Lewin, J. van Paradjijs & E. P. J. van den Heuvel

[5] Frank J., King A.R., Raine D.J., *Accretion power in astrophisics,* Cambridge University Press.

[6] Israel G., PhD thesis ”A Systematic Search of New X-ray Pulsators in ROSAT Fields”, 1996.

[7] Peterson B., *An introduction to AGN*, Cambridge University Press

[8] Lewin, W. et al., 2004, ”X-ray bursts” in *X-ray binaries* Cambridge Astrophys. Ser. 26, ed. W. H. G. Lewin, J. van Paradjijs & E. P. J. van den Heuvel

[9] Lewin W. H. G., van den Heuvel E. P. J., *Accretion driven stellar X-ray sources*, Cambridge University Press.

[10] Strohmayer, T. & Bildsten, L., 2004, ”New view of thermonuclear bursts”, in *Compact Stellar X-Ray Sources*, Cambridge Astrophys. Ser. 26, eds. W.H.G. Lewin and M. van der Klis

[11] Kuulkers, E., den Hartog, P. R., in't Zand, J. J. M., Verbunt, F. W. M., Harris, W. E., & Cocchi, M., 2003, A&A, 399, 663

[12] Hasinger, G. & van der Klis, M., 1989, A&A, 225, 79

[13] van der Klis M., "Rapid X-ray variability" in *Compact Stellar X-ray Sources*, eds. W.H.G. Lewin and M. van der Klis, Cambridge Astrophys. Ser. 39

[14] Fender, R.P., 2004, "Jets from X-ray Binaries" in *Compact Stellar X-ray Sources*, eds. W.H.G. Lewin and M. van der Klis, Cambridge Astrophys. Ser. 39

[15] Sakura N. I., Sunyaev R. A., A&A 24, 337, 1973.

[16] Mitsuda et al., PASJ 36, 741, 1984.

[17] Narayan R. & Yi I. ApJ 428L, 13, 1994

[18] Quataert E. & Gruzinov A. ApJ 539, 809, 2000.

[19] Giorge, I. M.; Fabian, A. C. MNRAS 249, 352, 1991

[20] Longair M. S., *High energy astrophysics*, Cambridge.

[21] Gierliński, M., & Done, C., 2003, MNRAS, 342, 1083

[22] Barret D. AIPC 703 238B

[23] Di Salvo, T. & Stella, L., 2002, in proceeding of *"The Gamma Universe"*, The Gioi Publishers, astro-ph/0207219

[24] White N. E., et al. MNRAS 218, 129, 1986.

[25] McClintock J.E., Remillard R. A., "Black hole binaries", in *Compact Stellar X-ray Source*, W.H.G. Lewin e M. van der Klis, Cambridge Astrophys. Ser. 39

[26] Barret, D. & Vedrenne, G. ApJSS 92, 505, 1994.

[27] Barret, D., McClintock, J. E., & Grindlay, J. E. 1996, ApJ, 473, 963

[28] Barret, D., Olive, J. F., Boirin, L., Done, C., Skinner, G. K., & Grindlay, J. E. 2000, ApJ, 533, 329

[29] Tavani M. & Barret D. AIP 410, 75, 1997

[30] Zdzdiarski A. A., et al. MNRAS 301, 435, 1998

[31] Churazov E., et al. Adv Space Res. 19, 55, 1997

[32] Di Salvo, T., Stella, L., Robba, N. R., et al. 2000, ApJ, 544, L119

[33] D'Amico, F., Heindl, W. A., Rothschild, R. E., & Gruber, D. E. 2001, ApJ, 547, L147

[34] Piraino, S., Santangelo, A., Ford, E. C., & Kaaret, P. 1999, A&A, 349, L77

[35] Di Salvo, T., Robba, N. R., Iaria, R., Stella, L., Burderi, L., & Israel G. L. 2001, ApJ, 554, 49

[36] Fender, R. P., Belloni, T., Gallo, E. MNRAS 355, 1105, 2004.

[37] Migliari, S., & Fender, R. P. MNRAS, 366, 79, 2006

[38] Gallo, E., Fender, R. P., Pooley, G. G. MNRAS 344, 60, 2003

[39] Hjellming, R. M., and Wade, C. M., Astrophys. J. Lett., 168, L21, 1971

[40] Fender, R. P. & Hendry, M. A. MNRAS 317, 1, 2000

[41] Migliari, S., Fender, R. P., Rupen, M., Wachter, S., Jonker, P. G., Homan, J., & van der Klis, M. 2004, MNRAS, 351, 186

[42] Migliari, S., Fender, R. P., Rupen, M., Jonker, P. G., Klein-Wolt, M., Hjellming, R. M. & van der Klis, M. 2003, MNRAS, 342, L67

[43] Capitanio F., PhD thesis "Transient BHC observed with *INTEGRAL* ", 2007

[44] Winkler C., ESA-SP 459, 471, 2001

[45] Caroli E. et al., SSR 45, 349, 1987

[46] Goldwurm, A, Ex. A. ,6 , 9 1995

[47] Ubertini P. et al., A&A 411L, 131, 2003

[48] Lebrun, et al., 2003, A&A, 411, L141

[49] Di Cocco, G., Caroli, E., Celesti, E., et al. A&A, 411, L189, 2003

[50] Vedrenne, G., Roques, J.-P., Schnfelder, V., et al. A&A, 411, L63, 2003

[51] Lund N. et al., A&A 411, L238, 2003

[52] Mas-Hesse, J. M.; Gimnez, A.; Culhane, J. L. et al. A&A, 411 L261, 2003

[53] Goldwurm, A., David, P., Foschini, L., et al. 2003, A&A, 411, L223

[54] Courvoisier, T. J.-L.; Walter, R.; Beckmann, V.; Dean, A. J. et al. A&A 411L, 53, 2003

[55] ISDC, IBIS analysis user manual, versione OSA 5.1, 2006

[56] Zdziarski A. A., Gierlinski M., *Radiative processes, spectral states and variability of black-hole binaries*, in Progress of theoretical physics, Proceeding supplement, 2004,

[57] Titarchuk, L. ApJ, 434, 570, 1994

[58] Poutanen, J., & Svensson, R. 1996, ApJ, 470, 249

[59] Magdziarz, P., & Zdziarski, A. A. 1995, MNRAS, 273, 837

[60] Asai, K., Dotani, T., Mitsuda, K., Nagase, F., Kamado, Y., Kuulkers, E., & Breedon, L. M. 1994, PASJ, 46, 479

[61] Bazzano, A., et al. 2006, ApJL, 649, 912

[62] Bevington, P. R., & Robinson, K. D. 1992, Data Reduction and Error Analysis for the Physical Sciences, 2nd Ed., New York, McGraw-Hill

[63] Bloser, P. F., Grindlay, J. E., Kaaret, P., Zhang, W., Smale, A. P., & Barret, D. 2000, ApJ, 542, 1000

[64] Chou, Y., & Grindlay, J. E. 2001, ApJ, 563, 934

[65] Cornelisse, R., et al. 2003, A&A, 405, 1033

[66] Farinelli, R., Frontera, F., Zdziarski, A. A., Stella, L., Zhang, S. N., van der Klis, M., Masetti, N., & Amati L. 2005, A&A, 434, 25

[67] Gierliński, M., & Done, C., 2002, MNRAS, 337, 1373

[68] Gierliński, M., Zdziarski, A. A., Poutanen, J., Coppi, P. S., Ebisawa, K., & Johnson, W. N. 1999, MNRAS, 309, 496

[69] Grindlay, J., Gursky, H., Schnopper, H., Parsignault, D. R., Heise, J., Brinkman, A. C., & Schrijver, J. 1976, ApJ, 205, L127

[70] Markoff, S., Nowak, M. A., & Wilms, J. 2005, ApJ, 635, 1203

[71] McConnell, M. L., et al. 2002, ApJ, 572, 984

[72] Priedhorsky, W. & Terrell, J., 1984, ApJ, 284, L17

[73] Rappaport, S., Nelson, L. A., Ma, C. P., & Joss, P. C. 1987, ApJ, 322, 842

[74] Shaposhnikov, N., & Titarchuk, L. 2004, ApJ, 606, L57

[75] Shibata, K., 2005 , in Proc. of Magnetic Fields in Universe, E. Dalpino et al., eds. APS

[76] Sidoli, L., Parmar, A. N., Oosterbroek, T., Stella, L., Verbunt, F., Masetti, N., & Dal Fiume, D. 2001, A&A, 368, 451

[77] Šimon, V. 2003 , A&A, 405, 199

[78] Stella, L., Priedhorsky, W., & White N. E. 1987, ApJ, 312, L17

[79] Wardziński, G., Zdziarski, A. A., Gierliński, M., Grove, J. E., Jahoda, K., & Johnson, W. N. 2002, MNRAS, 337, 829

[80] Wen, L., Levine, A. M., Corbet, R. H. D., & Bradt, H. V. 2006, ApJS, 163, 372

[81] Winkler, C., Gehrels, N., Lund, N., Schönfelder, V., & Ubertini, P. 1999, ApL&C 39, 361

[82] Winkler, C., Courvoisier, T. J.-L., Di Cocco, G., et al. 2003a, A&A, 411, L1

[83] Winkler, C., Gehrels, N., Schönfelder, V., et al. 2003b, A&A, 411, L349

[84] Zdziarski, A. A., & Gierliński, M. 2004, PThPS, 155, 99

[85] Zdziarski, A. A., Lubiński, P., & Smith, D. A. 1999, MNRAS, 303, L11

[86] Zdziarski, A. A., Poutanen, J., & Johnson, W. N. 2000, ApJ, 542, 703

[87] Zdziarski, A. A., Lubiński, P., Gilfanov, M., & Revnivtsev, M. 2003, MNRAS, 342, 355

[88] Zdziarski, A. A., Wen, L., & Gierliński, M. 2006, MNRAS, in preparation

[89] Zhang, W., Smale, A. P., Strohmayer, T. E., & Swank, J. H. 1998, ApJ, 500, L171

[90] Barret, D. et al., 2003, A&A, 400, 643

[91] Brandt, H.V., Rothschild, R.E. & Swank, J. H., 1993, A&A, 97, 355

[92] Cocchi, M. et al., 2000, A&A, 357 527

[93] Forman, W. et al, 1976, ApJ, 206, L29

[94] Kuulkers, E.,,2004, Nuclear Physics, B 132, 466

[95] Labanti, C. et al., 2003, A&A, 411, L149

[96] Mereghetti, S. et al., 2003, A&A 411, L291

[97] Muno, P. et al., 2005, ApJ 626, 1020

[98] Murakami, T. et al., 1983, PASJ 35, 531

[99] Wijnands, R. & van der Klis, M., 1999, ApJ 514, 939

[100] Wilson, C. A. et al., 2003,astro-ph/0307045

[101] Barret, D., Olive, J.F., Boirin, L. et al. A&A 357, L41, 1991

[102] Grindlay, J. E., Marshall, H. L., Hertz, P., et al. ApJ 240, L21,1980

[103] Parmar A.N., Stella, L. & Giommi, P., A&A 222, 96, 1989

[104] Swank, J.H., Becker, R. H., Boldt, E. A., et al. 1977, ApJL 212 L73.

[105] Olive, J.F., Barret, D., Boirin, L. et al. 1998 A&A 333, 942

[106] Tarana A., Bazzano A., Ubertini P. submitted to ApJ.

[107] Chaboyer, B., et al. 2000, Astron. J. 120, 3102

[108] Hertz P., & Wood K. S. 1985, ApJ 290, 171

[109] Heike, C. O., Edmonds, P. D. & Grindlay, J. E. 2001, ApJ 562, 363

[110] In't Zand, J. J., et al. 1998, A&A 329,L37

[111] Parmar, A. N., Oosterbroek, T., Sidoli, L., et al. 2001, A&A 380, 490

[112] Predehl, P., Hasinger, G., & Verbunt, F. 1991, A&A 286, 444

[113] Tarana, A., Bazzano, A., Ubertini, P. et al. 2006, A&A 448, 335

[114] Titarchuk, L. 1994, ApJ 434, 570

[115] van Paradjijs, J. 1995, in *X-ray Binaries*, Cambridge Astrophys. Ser. 26, ed. W. H. G. Lewin, J. van Paradjijs & E. P. J. van den Heuvel

[116] Courvoisier, T., J., -L. et al. 1986, ApJ 309, 265

[117] Iaria, R., Di Salvo, T., Burderi, L., et al 2001, ApJ 548, 883

[118] White, N.E., & Holt, S. S., 1982 ApJ, 257, 318

[119] Asai, K., Dotani, T., Mitsuda, K. et al 1996 PASJ 48, 257

[120] Boella, G., Butler, R.C. , Perola, G.C. et al 1997, A$ASupll 122, 299

[121] Campana, S., Stella, L., Mereghetti, S. et al., 2000 A&A, 358, 583

[122] Lochner, J. and Roussel-Duprè D., 1994, ApJ 435, 840

[123] Nakamura, N., Dotani, T., Inoue H., et al. 1989 PASJ 41, 617

[124] Rutledge, R.R., Bildsten, L., Brown, E. F., et al. , 1999, ApJ, 514, 945

[125] Rutledge, R.R., Bildsten, L., Brown, E. F., et al., 2000, ApJ, 529, 985

[126] Simon, V. 2004, A&A, 418, 617

[127] Tarana A., Bazzano B., Ubertini P. & Zdziarski A.A., ApJ 654, 494, 2007

[128] Zavlin, V.E., Pavlov, G.G. and Shibanov, Yu.A. 1996, A&A, 351, 141

[129] Remillard, R. and Morgan, E. 2005, ATel 482.

[130] Tarana A., Belloni T., Homan J., Mendez M., Bazzano A., Ubertini P. in preparation

[131] Amati, L., PhD thesis in Astronomy 2004.

[132] Parmar, A.,N. et al. Astron. Astrophys. Suppl. Ser., 122, 307-326, 1997

[133] Boella, G., Chiappetti, L., Conti, G., et al. Astron. Astrophys. Suppl. Ser., 122, 327-340 1997

[134] Manzo, G., Giarrusso, S., Santangelo, A., et al. Astron. Astrophys. Suppl. Ser., 122, 341-356, 1997

[135] Jager, R., Mels, W.A., Brinkman, A.C., et al. Astron. Astrophys. Suppl. Ser., 125, 557, 1997

[136] Frontera, F., Costa, E., Dal Fiume, D., et al. Astron. Astrophys. Suppl. Ser., 122, 357, 1997

[137] Levine, A. M. et al. ApJ, 469, L33-L36, 1996

[138] Bradt, H. V., et al. A&AS, 97, 355-360, 1993.

[139] Jahoda, K. AAS Meet., 26, 894, 1994

[140] R. E. Rothschild, P. R. Blanco, D. E. Gruber, et al. ApJ 496, 538, 1998

Finito di stampare il February 22, 2008 utilizzando LaTeX 2ε

Finito di stampare il February 22, 2008 utilizzando LaTeX 2ε

Acknowledgments

I first want to thanks my tutors Pietro Ubertini and Angela Bazzano of IASF of Rome, to give me the possibility to do this work thesis at the better way, thanks for all their precious theachings and advices and thanks to learn me how much it is difficult but also real nice and excitant the research work. I hope to will carry with me the enthusiasm in this work as they do every day.

I would like to thanks also to the PhD coordinator Roberto Buonanno and all the theachers for their addiction to the the PhD project of Tor Vergata University. Thanks in particular to Luigi Stella to have been showed how it can be nice also the theaching.

Thanks to all my collaborators who contribuited to give some of the important results of this thesis work: Andrzej Zdziarski, Diego Götz, Antony Bird, Tomaso Belloni, Jeroen Homan, Mariano Méndez and Lara Sidoli.

Thanks to all my colleagues and collaborators of IASF of Rome, for their abetment and collaborations every time, so thanks to Fiamma Capitanio, Giovanni De Cesare, Melania del Santo, Mariateresa Fiocchi, Lorenzo Natalucci, Memmo Federici, Ugo Zannoni, Massimo Cocchi, Catia Spalletta, Alessandra De Rosa, Giuliano Sabatino e Sergio Di Cosimo.

Thanks to my PhD colleagues and friends of Tor Vergata and La Sapienza, Silvia Giordano, Francesco Massaro, Marialaura Conciatore, Massimo De Luca, Fiore De Luise, Giuliano Giuffrida, Alessandro Papitto, Silvia Gianní and Fabio Muleri. Thanks also to the other PhD students that I have known in Schools and Workshops during these years for their useful discussions and to give me the way to compare with my work.

But the actual thanks I need to give to my family. Thanks to my parents Ranieri Rossana and Narciso Tarana, without you I will never done nothing. Thanks to my brother for all his support in every moment I need it, and thanks also to my upcoming sister in law as well as friend Laura and her family.

I great and really special thanks to my ”new family” Salvatore D’Antonio, Ninno, for his lovely comfort and to have been give me the belief in me every time, and to my dog Maggie the only one that has quietly suffered all my days of study and works. Thanks also to Carla Cozzolino and Giacinto D’Antonio for thier support and interest that my work will go in good way.

Thanks to all my friends that give me support with their friendship and for the care-free evening during these three years of PhD: Airella, Alessandro O., Cristiana, Pier, Emanuaela, Prisco, Marinella, Rino, Sara, Massi...e his partyes with all his friends such as... ’Nimalo. Thanks also to my friends that I rarely see but not for this are less important: my friends of Bologna Marica, Laura, Valentina, Marghe and also Alessandro and Luisa, Mimmetta and Cinzia.

Thanks also to my relatives of Cineto Romano and thanks to all my relatives of Fiumicino and Napoli. Thanks, thanks to everybody.

Finito di stampare il February 22, 2008 utilizzando LaTeX 2ε